INFORMATION TO USERS

The most advanced technology has been used to photograph and reproduce this manuscript from the microfilm master. UMI films the text directly from the original or copy submitted. Thus, some thesis and dissertation copies are in typewriter face, while others may be from any type of computer printer.

The quality of this reproduction is dependent upon the quality of the copy submitted. Broken or indistinct print, colored or poor quality illustrations and photographs, print bleedthrough, substandard margins, and improper alignment can adversely affect reproduction.

In the unlikely event that the author did not send UMI a complete manuscript and there are missing pages, these will be noted. Also, if unauthorized copyright material had to be removed, a note will indicate the deletion.

Oversize materials (e.g., maps, drawings, charts) are reproduced by sectioning the original, beginning at the upper left-hand corner and continuing from left to right in equal sections with small overlaps. Each original is also photographed in one exposure and is included in reduced form at the back of the book. These are also available as one exposure on a standard 35mm slide or as a 17" x 23" black and white photographic print for an additional charge.

Photographs included in the original manuscript have been reproduced xerographically in this copy. Higher quality 6" x 9" black and white photographic prints are available for any photographs or illustrations appearing in this copy for an additional charge. Contact UMI directly to order.

U·M·I

University Microfilms International
A Bell & Howell Information Company
300 North Zeeb Road, Ann Arbor, MI 48106-1346 USA
313/761-4700 800/521-0600

Order Number 9009730

Remote monitoring of gaseous pollutants by image topography techniques

El-Massry, Mohamed H., Ph.D.

City University of New York, 1989

U·M·I
300 N. Zeeb Rd.
Ann Arbor, MI 48106

A

REMOTE MONITORING OF GASEOUS POLLUTANTS
BY
IMAGE TOPOGRAPHY TECHNIQUES

By

MOHAMED H. EL-MASSRY

A dissertation submitted to the Graduate Faculty in Engineering in partial fulfillment of the requirements for the degree of Doctor of Philosophy, The City University of New York.

1989

This manuscript has been read and accepted for the Graduate Faculty in Engineering in satisfaction of the dissertation requirement for the degree of Doctor of Philosophy.

6/2/89

Date

Chair of Examining Committee

6/5/89

Date

Jacques E. Benveniste

Executive Officer

Professor S. Ahmed
Professor J. Barba
Doctor D. Kokkinos
Professor L. Roytman

Supervisory Committee

The City University of New York

Abstract

REMOTE MONITORING OF GASEOUS POLLUTANTS BY IMAGE TOPOGRAPHY TECHNIQUES

By

MOHAMED H. EL-MASSRY

Adviser: Professor Samir Ahmed

The objective of this thesis was to experimentally demonstrate the viability of utilizing CCD video cameras to measure, detect and monitor molecular air pollution and trace contaminants in the atmosphere. Differential spectral absorption wavelengths were used to identify and delineate specific pollutants. Standard video output carried data to appropriate image processors, producing a color-coded display on an RGB monitor. A frame of video information captured by a frame grabber was processed according to the pollution ratio present in the frame and presented as a digitized image. This digitized image was then displayed on a topographical layout, showing varying levels of concentration and a distribution profile of the pollutant superimposed on the image of the scene being viewed.

This video monitoring technique increases the capability of performing real-time frame analysis and structural analysis of pollutant concentrations.
The differential absorption technique was used to detect images within a specific wavelength or absorption band, were synthesized, saved, and later retrieved as references in comparing similar absorption patterns in real-time. A pattern of absorption images could provide qualitative detection information on pollutants or the tracking of a contaminating gas spill over a densely populated area. Another important aspect of this technique is its potential to provide detection information via a standard video format signal which could be transmitted live to remote locations for additional interpretation.

The Remote Sensing Laboratory of the City College of New York pioneered the use of the differential absorption of scattered laser energy (DASE), which successfully demonstrated that measurements of atmospheric molecular pollution could be used to provide real-time monitoring. The results of these active laser radar techniques served as the impetus for video monitoring techniques.

In contrast to laser techniques, the video monitoring technique can be passive or active, and views a entire scene rather than merely monitoring the path of the laser beam. The system also provides great potential for indoor use, e.g. in detecting low level concentrations of hazardous gases inside chemical plants, industrial facilities or research laboratories.

ACKNOWLEDGEMENTS

I would like to express my gratitude to all the member of my doctoral committee. In particular, I would like to thank my mentor, Professor Samir Ahmed, for his support and guidance in the development of this work. I would like to dedicate this thesis to my wife, Deirdre, whose patience, great support and understanding during the course of this undertaking encouraged me to attain my goals. Without her continues encouragement, I doubt that I could have completed this task. Finally I am grateful to my parents, my family and my wife's family for their continuous encouragement.

To my wife

Deirdre

Table of Contents

Table of Figures

Table of Tables

1 Introduction and Background

Many spectral regions have been used for the remote detection and measurements of air pollutants including UV Visible and IR regions. The UV and Visible regions tend to be the regions of choice for fairly simple molecules. The Mid-IR is frequently the best region for detection of more complex molecules. There are essentially two ways in which optical interaction can be used to detect the presence of trace constituent molecule[1]:

(i) Selective absorption by the molecules of preferential spectral regions, or wavelength.

(ii) Emission by the trace molecules of specific wavelengths that are characteristic of them, when they are irradiated with light of appropriate wavelengths.

Both the emission and the absorption can be detected by remote techniques to determine the nature and concentration of pollutants present, and both approaches have been used in conjunction with lasers to measure atmospheric molecular pollution.

Research and development since the early sixties has concentrated on developing LIDAR into an effective method for air pollution monitoring. The first recorded backscattered echoes from the atmosphere were reported by Ficco and Smullin[2] and by Ligada[3] in 1963 measured the backscattered signal from haze. Raman Scattering was first used in 1967 to detect molecular constituents of the atmosphere by Leonard, Cooney and Malfi. In 1969 Inaba and Kobayashi discussed the possibility of pollution detection by Raman scattering and they were able at 1970 to detect SO_2 and CO_2 in the atmosphere, though sensitivity was not adequate for trace contaminant measurements typically found in polluted urban areas.

Kabayashi and Anaba[4] in 1971 using a Nitrogen laser operating at 3371 $\mathring{A}$ with 20 Kw peak power had detected Raman signals from clear air and from an oil smoke plume. Progress in laser sources lead to improvement in Raman detection systems. Hirschfield[5] described a system at 1973 using a frequency doubled Ruby laser transmitter with 3m aperture telescope as the receiver this was used in field tests to detect CO_2 , H_2O and SO_2 over 200m range, concentration of approximately 10000 ppm of water vapor and 310 ppm of CO_2 and 300 ppm of SO_2 were detected. The development of tunable dye lasers opened possibilities for other LIDAR pollution detection methods with inherent advantages over the Raman technique. The four LIDAR schemes for which tunable dye lasers are particularly important for the detection of molecular pollutants with resonant absorption in the visible and near ultraviolet are Resonance Raman, Long Path absorption, Resonance Fluorescence and Differential Absorption of Scattered Energy "DASE"

Resonance Raman : observation of resonance Raman scattering in gases have been very few. Bernstein[6] (1973) measured resonance in gases Ci_2, Br_2, and I_2, where he obtained intensities of 10 to 1000 times stronger than the normal Raman effect. Rosen (1975) estimated the feasibility of using resonance Raman scattering for the remote detection of pollutants, estimating that for 10,000 pulses of 0.05 mj each, 100 ppm of NO could be detected during the daytime (with S/N ratio of 10). These concentrations are 3 to 4 orders of magnitude higher than ambient pollution concentrations encountered normally.

Long Path Absorption : Hanst[7] (1968) described the measurement of average pollutant concentration along a laser beam path by laser resonance absorption. Hodgeson, Mc Clemmy and Hanst (1973) suggested long path absorption schemes for determining average pollutant densities. Kidal and Byer[8] gave a detected analysis of the doubled-ended long path absorption method, which later extended to the single-ended absorption method using a topographical targets by Byer and

Garbuny[9] determine the average pollutant density along a laser beam path absorption measurements have been carried out using a lsw power diode lasers by Hinkley, concentration ranging from 74 to 1000 ppm of C_4H_4 and N_2 were detected in a laboratory in a sample chamber 30 Cm long, O'Shea and Dodge (1974) measured NO_2 absorption coefficients for the most prominent Argon-ion laser lines a corner cube reflector was positioned 3.54 Km from laser site to reflect the laser signal back to the receiver, integrated pollutant concentrations ranging from 0.05 ppm to 0.15 ppm of NO_2 were detected.

Resonance Fluorescence : Bowman, Gibson and Sandford[10] (1969) used a flashlamp - pumped dye laser to obtain nighttime measurements of sodium in the upper atmosphere. The output of the dye laser was used to induce fluorescence from Sodium at altitudes up to 150 Km. Concentrations ranging from $1.8x10^{14}$ m^{-2} to $9x10^{12}$ m^{-2} were detected at altitudes of 80 to 100 Km. Gibson and Sandford (1970) extended their use of the resonance fluorescence scheme into a daytime operation by using a narrow band optical receiver Gelbwachs (1972) utilized resonance fluorescence of No_2 excited by an Argonne-Ion laser to detect No_2 locally with a sensitivity of one part per billion the laser excitation was at 4480 $\mathring{A}$ and the fluorescence was monitored at 7000$\mathring{A}$ to 8000$\mathring{A}$. The increased sensitivity of resonance fluorescence backscattering makes it appear useful as a remote monitoring method compared to the Raman method also the sensitivity of the resonance fluorescence scheme is greatly surpassed by the differential absorption of scattered energy method (DASE).

Differential Absorption of Scattered Energy (DASE): this method was first suggested by Schotland[11],[12] in 1964 using a search light as a source for water vapor measurement, the method was extended to laser (LIDAR) pollution monitoring by Ahmed[13] (1973). Measurements using the differential absorption method were carried out at the Remote Sensing Laboratory in the City College using a flashlamp-pumped dye laser operating in the 4450$\mathring{A}$ spectral region[14]. NO_2 was measured of known concentration in a sample chamber using this technique of remote measurements of ambient NO_2, SO_2 and O_3 were carried out in the areas surrounding the College. The results, when correlated with wet chemical measurements showed that typical ambient concentrations of 1.005 ppm could be remotely measured in real time.

2 Basic Principles of Atmospheric Sensing and Radiative Transfer

The interaction of the electromagnetic waves with the atmospheres are governed by the characteristics of propagating wave (mainly its wavelength), the physical characteristics of the atmosphere (Pressure, Temperature and Suspended particules) and the atmospheric constituents. These interaction mechanisms are complex, because of their three dimensional nature of propagation in a medium. The multiplicity of the interactions take different form such as: Scattering, Absorption, Emission and Refraction, in this section I will give a brief overview of the physical and chemical properties of the atmosphere that are relevant to remote sensing[15].

2.1 Physical Properties of the Atmosphere

The atmospheric density falls with altitude, in case of the hydrostatic equilibrium the pressure $p(z)$ and the density $\rho(z)$ are related by the following relationship:

$$dP(z) = -g\rho(z)\,dz \qquad (3.1.1)$$

Where: g = the gravity which is assumed to be constant through thin atmospheric layer

$p(z)$ = the pressure measured upward from the surface (vertically)

The expression in equation (3.1.1) basically states that the difference of pressure between level (z) and (z + dz) is equal to the weight of the atmosphere between these two levels. The equation of state for a perfect gas relates the $p(z)$, $\rho(z)$ as follow:

$$\rho(z) = MM_0 \frac{P(z)}{KT(z)} \tag{3.1.2}$$

Where: M = the average molecular weight of the atmosphere
= 28.97 for the atmosphere.
M_0 = the atomic mass unit (1.66×10^{-27} Kg)
K = Boltzman constant (1.36×10^{-23} JK^{-1})
T = temperature

The number density $N(z)$ (molecules /m^3) are related to the pressure $p(z)$ by the following relationship:

$$N(z) = \frac{P(z)}{KT(z)} \tag{3.1.3}$$

from equation (3.1.3) one can express the pressure as:

$$P(z)=N(z)KT(z) \tag{3.1.4}$$

combining (3.1.2,3) and (3.1.4)

$$\frac{dP(z)}{P(z)} = -g\frac{\rho(z)dz}{N(z)KT(z)} \tag{3.1.5}$$

$$\frac{dP(z)}{P(z)} = -g\frac{MM_0P(z)d(z)}{N(z)\{KT(z)\}^2} \tag{3.1.6}$$

$$\frac{dP(z)}{P(z)}=-g\frac{MM_0}{KT(z)}dz \tag{3.1.7}$$

$$\frac{dP(z)}{P(z)} = -\frac{dz}{H(z)} \tag{3.1.8}$$

Where

$$H(z)=\frac{KT(z)}{gMM_0} \tag{3.1.9}$$

H(z): known as the scale height

We also can express the pressure P(z) from (3.1.8) as:

$$P(z) = -\frac{H(z)}{d(z)}dP \tag{3.1.10}$$

solving for P(z):

$$P(z) = P(0)\exp\left(-\int_0^z \frac{d\xi}{H(\xi)}\right) \tag{3.1.11}$$

Where: P(0) is the surface pressure, for example if we have an isothermal atmosphere the temperature T will be constant then:

$$P(z) = P(0)\exp\left(\frac{-Z}{H}\right) \tag{3.1.12}$$

This equation shows that the pressure decreases exponentially with altitude and the same also proven to be true for the density

$$\rho(z) = \rho(0)\exp\left(\frac{-Z}{H}\right) \tag{3.1.13}$$

Where:

$$\rho(0) = \frac{MM_0P(0)}{KT} = \frac{P(0)}{gH} \tag{3.1.14}$$

In a similar fashion the number density N (molecules/m^3) is given as:

$$N(z) = N(0)\exp\left(\frac{-Z}{H}\right) \qquad (3.1.15)$$

By integrating equation (3.1.13) and using equation (3.1.14) to substitute for the density number for the pressure one can get the total atmospheric mass M_T in a column of unit area

$$M_T = \int_0^\infty \rho(z)dz = \rho(0)H \qquad (3.1.16)$$

$$\rho(0)H = \frac{P(0)H}{gH} \qquad (3.1.17)$$

$$M_T = \frac{P(0)}{g} \qquad (3.1.18)$$

The previous equation shows that the scale height corresponds to the thickness of a homogeneous atmospheric layer of density $\rho(0)$ and mass equal to the atmospheric mass.

Just for the sake of illustration if we consider a case of earth atmosphere we have:

$M = 28.97$ and $\rho(0) = 1$ atmosphere= 10^5 Newton / m^3

$g = 9.81$ m/sec^2 and $T = 288^{\circ}K$

The scale height H(z):

$$H(z) = \frac{KT(z)}{gMM_0} = \frac{288^{\circ}K \times 1.38 \times 10^{-23} JK^{-1}}{9.81\, m/\sec^2 \times 28.97 .66 \times 10^{-27} Kg}$$

$$H(z) = 8.4 \text{ Km}$$

The surface density $\rho(0)$ can be given as:

$$\rho(0) = \frac{P(0)}{gH} = \frac{10^5 \text{N}ewton/m^2}{9.81\, m/\sec^2 \times 8.4 Km}$$

$$\rho(0) = 1.21 \; Kg/m^3$$

The total atmospheric mass M_T in a column of unit area:

$$M_T = \frac{P(0)}{g} = \frac{10^5 Newton/m^2}{9.81\, m/\sec^2}$$

$$M_T = 10200 \text{ Kg/m}^3$$

The previous illustrations assumed an isothermal atmosphere. Usually the temperature near the surface decreases as a function of altitude up to 11 Km then remain constant up to the 25 Km level[16]. The change of the atmospheric temperature can be derived for a simplified case where it is assumed that the atmosphere is transparent to all radiation and that it contains no liquid particles. Knowing that most of the atmospheric mass is in a very thin layer above the surface relative to the planets radius. In the case of earth, 99% of the atmospheric mass is below 32 Km. If we assume a unit mass moving upward in an atmosphere in hydrostatic equilibrium, first law of thermodynamics gives:

$$C_v dT + PdV = dq \tag{3.1.19}$$

Where: C_V = the specific heat at constant volume.

dV = the change in volume.

dT = the change in temperature.

dq = the heat input = zero.

Combining (3.1.4) and (3.1.14) one can express the number density as:

$$\rho(z) = MM_0 \frac{P(z)}{KT(z)} = MM_0 N(z) \tag{3.1.20}$$

$$\rho = \frac{1}{V} = MM_0 \frac{P(z)}{KT(z)} \tag{3.1.21}$$

Differentiating equation (3.1.2) gives

$$Pdv + Vdp = \frac{K}{MM_0}dT \tag{3.1.22}$$

For a perfect gas :

$$\frac{K}{MM_0} = C_p - C_v \tag{3.1.23}$$

Where C_p is the pacific heat at constant pressure combining (3.1.19) and (3.1.23)

$$C_v dT + PdV = (C_p - C_v)dT \tag{3.1.24}$$

$$Vdp = C_p dT \tag{3.1.25}$$

Combining equation (3.1.1) with (3.1.25) one can allows express the rate of change in temperature with respect to the distance z :

$$-g\rho(z)dz = \frac{C_p}{V}dT \tag{3.1.26}$$

$$\frac{dT}{dz} = -\frac{g}{C_p} = -\Gamma_a \tag{3.1.27}$$

Where: Γ_a is known as the Adiabatic Lapse Rate (ALR). for the atmosphere C_p = 1000 J/Kg K. Which gives:

$$\Gamma_a = -\frac{9.81 m/\sec^2}{1000 J/KgK}$$

$$\Gamma_a = 9.81 K/Km$$

One can also notes from observing equation (3.1.22) that the temperature at the bottom of the atmosphere is equal to T(0) and the solution for T(z) become as follows:

$$T(z) = T(0) - \Gamma_a Z \qquad (3.1.28)$$

In reality the temperature in the earth lower atmosphere does decreases linearly with altitude but at a rate of 6.5 K/Km some what lower than Γ_a at a higher altitudes the temperature profile is significantly more complex.

2.2 Atmospheric Composition

For the atmosphere carbon dioxide, water vapor, and ozone dominate the interaction with electromagnetic radiation. Main constituents which represent the atmospheric compositions are N_2 78% and O_2 21% and Ar 1% beside H_2, CO_2, O_3 as a small percentage. Carbon dioxide is substantially uniformly mixed up about 100 Km. The interaction of the CO_2 molecule with electromagnetic waves is strongest in the infrared band near (4.3 - 15)μm It plays a dominant role in the energy budget of the mesosphere (50 - 90)Km, which is cooled as a result of CO_2 radiative emission in the 15 μm band. Water vapor plays an important role in the energy budget of the troposphere (below 15 Km), because its rule in the cloud formation precipitation and energy transfer in the form of latent heat. Its also highly variable in space equal 0.25 % of the total atmospheric mass. Its partially important in remote sensing because of the strong water vapor absorption lines in the infrared and microwave region. Ozone strongly absorbs UV radiation and cause radiation and causes a short wave cutoff of the earth transmission at 0.3 μm and shorter its mostly concentrated between 20 - 50 Km altitude[17].

2.2.1 Nitrogen Oxides

Most health effects associated with nitrogen oxides (NO_x) have been attributed to nitrogen dioxide (NO_2). However, the major anthropogenic sources of NO_x are combustion processes which primarily produce nitric oxide (NO). This gas is subsequently oxidized to NO_2. Levels of NO_2. above 282 mg/m^3 (150 ppm) can be lethal while concentrations in the range of 94-282 mg/m^3 (150 ppm) can produce chronic lung disease (Ferris, 1978). The earliest response to NO_2 occurs in the sensory organs. Odor can be perceived at 0.23 mg/m3 (0.12 ppm) and reversible changes in adaptation at exposures of 0.14-0.50 mg/m^3 (0.075-0.26 ppm) (NAS. 1977b). In community exposure studies done by the EBA[18], shows a higher incidence of respiratory symptoms and diseases were seen in children living in homes with gas stoves (a NO_x source) as apposed to those in homes with electric stoves, where indoor concentrations were measured. The absorption Spectrum of NO_2 are given in Fig.3.2.1.

2.3 Particulates and Clouds

Particulate are the atmospheric dust particles of radii between 0.1 and 10 μm. Clouds of liquid and solid water have particles of size varying between 1 μm and 100 μm. Particulates are usually concentrated in the lowest few Kilometers and tend to scatter radiation in the Visible and Near Mid-IR. The distribution of the number of density of large particles can also be approximated by an exponential decay as follow[19]

$$N(z) = N(0)\exp\left(\frac{-Z}{Hp}\right) \tag{3.3.1}$$

Where: H_p = the particles scale height

2.4 Wave Interaction Mechanisms in the Atmosphere

The interaction of the electromagnetic waves with planetary atmosphere, involves resonant interactions corresponding to molecular and atomic energy levels, nonresonant interactions corresponding to molecular and atomic energy levels, nonresonant absorption and refraction, in addition suspended particles scatter the light waves and have their own radiative properties[20].

2.4.1 Resonant Interaction

When an electromagnetic wave interacts with gaseous molecule it may be exited the molecule to a higher energy level and in the process transfer all or part of its energy to the molecule.

A molecule in an exited state may droop to a state with a lower energy level and in the process emit energy in the form of an electromagnetic wave. The energy level of gaseous molecules are well defined and discreet. Thus, the related interaction occurs at a very specific frequency leading to specific spectral lines.

The environmental factors specifically temperature and pressure T(z), P(z) lead to the broadening of these lines to narrow bands. The basic mechanism behind the energy states molecules Electronic energy levels result from the transfer of electrons between different orbits, vibrational energy levels result from the different vibrational modes of the molecules. In addition, gaseous molecules have a rotational energy states which correspond to rotational of the molecule around different axes, on the other hand the interaction mechanisms which were related to the crystalline structure in solids, such as crystal field effects, semiconducting bands, and color centers do not exist in the case of gaseous. The lowest energy levels correspond to the rotational states. These levels depend on the three principal moments of inertia of molecule.

Four types of rotating molecules exist:

(1) All three principal moments of inertia are different the molecule is called **asymmetrical top** as in H_2O.

(2) Two of the moments are equal, the molecule is called **symmetrical top**

(3) All three moments are equal, the molecule is called **spherical top** as in CH_4

(4) Two of the moments are equal and the third is negligible, the molecule called **linear top** as in CO_2

No energy transitions are allowed in the pure rotation spectrum for a molecule which possesses no permanent dipole moment.

The symmetric linear CO_2 molecule is an example, to illustrate, let us consider the case of the water molecule and oxygen molecule.

The lowest spectral line for water vapor occurs at 22.2 GHz the next lowest one is at 183.3 GHz at two pressure level.

An interesting observation is that as the pressure decreases the absorption at the center of the line increases because the absorption from the same amount of the water vapor is now limited to a narrower band.

The Oxygen molecules has a permanent electrical dipole moment but a permanent magnetic dipole moment resulting from the fact that two of the orbital electrons are unpaired, so the two lowest spectral lines occur at 60 GHz (which is a band consisting of multiple lines) and 118.75 GHz The absorption due to atmospheric Oxygen and water vapor dominates the resonant interaction of waves in the earth's lower atmosphere across the microwave spectrum from 20 GHz to 180 GHz. In the upper atmosphere the trace molecules play a more tangible role, and their spectral signature is usually very rich in spectral lines. In the more simple model of atomic molecule and elementary calculation of the energy levels.

The molecule can be regarded as a dumbbell consisting of two masses at a fixed distance, let I be the moment of inertia relative to the axis perpendicular to the line connecting the two masses and intersecting it at the center of mass.

In quantum mechanics it can be shown that the corresponding rotational energy levels are given by:

$$E = \frac{h}{8\pi^2 I} j(j+1) \qquad (3.4.1.1)$$

Where: j = 0, 1, 2, 3,.... Known as the rotational quantum number The selection rule requires that transitions can occur only between adjacent energy levels $\Delta j = \pm 1$ the energy transfer for the transition from (j) to (j - 1) is

$$\Delta E_j = \frac{h}{8\pi^2 I}\{j(j+1)-(j-1)\}$$

$$\Delta E_j = \frac{h}{8\pi^2 I}j \qquad (3.4.1.2)$$

The above equation indicate that the spectrum consists of a series of equidistant lines.

The vibrational transitions correspond to significantly higher energy than the rotational transitions. Thus the corresponding spectral lines appear mainly in the Infrared region.

One of the most important transitions used in atmospheric remote sensing is the 15 μm line of Co_2 which corresponds to the bending of the linear molecule. As a molecule vibrate its effective moment of inertia varies. Thus we would expect the presence of a family of spectral lines around a vibrational line corresponds to rotation - vibration interactions. The rotational transitions appear as a fine structure near the vibrational lines.

The electronic transitions correspond to highest energies and the corresponding spectral lines are usually in the Visible and Ultraviolet part of the spectrum.

2.4.2 Spectral Line Shape

The spectral lines are not infinitely narrow, line broadening results mainly from the three following factors:

(1) Excited state life time.

(2) Pressure - induced collisions.

(3) Thermal motion.

If an excited state has a lifetime τ the spectral line will have a frequency width $\Delta\nu$ at least equal to:

$$\Delta\nu = \frac{1}{2\pi\tau} \qquad (3.4.2.1)$$

This can be derived by assuming the emission from an excited state to be a pulse with exponentially decaying amplitude as a function of time.

The Fourier Transform of such a pulse will have a spectral width given by equation (3.4.2.1). The thermal motion of a molecule during emission or absorption of radiation gives rise to a Doppler shift, considering that the thermal motion is random and the molecules velocity distribution is related to the temperature. It is normal to expect that the thermal motion induces a broadening of the spectral line. The resultant shape is given by the following relation:

$$K(\nu) = \frac{s}{\nu_D\sqrt{2\pi}}\exp\left[-\left(\frac{\nu-\nu_0}{\nu_D}\right)^2\right] \qquad (3.4.2.2)$$

Where **s** = constant representing the total strength of the line

$$S = \int_0^\infty K(\nu)d\nu \qquad (3.4.2.3)$$

ν_0 = the center frequency

ν_D = the doppler line width

Which related to gas temperature by:

$$\nu_D = \frac{\nu_0}{C}\sqrt{\frac{2\pi RT}{M}} \qquad (3.4.2.4)$$

Where: R = Universal gas constant = K/M_0 = 8314 JK^{-1} Kg^{-1}

M = Molecular weight of the gas

T = Temperature of the gas

The Doppler broadening dominates at high altitudes. Another mechanism of line broadening results from pressure-induced collisions described by Lorentz shape function as:

$$K(\nu) = \frac{S}{\pi}\frac{\nu_L}{(\nu-\nu_0)^2+\nu_L^2} \qquad (3.4.2.4)$$

Where: ν_L = Lorentz width

one can also relate the mean time between collisions t_C to Lorentz width by the following relationship:

$$\nu_L = \frac{1}{2\pi t_c} \qquad (3.4.2.5)$$

The collision time in turn is inversely proportional to the pressure, thus the Lorentz width is linearly proportional to the pressure

$$\frac{\nu_P}{P} = \frac{\nu_L(P_0)}{P_0} = constant \qquad (3.4.2.6)$$

Lorentz broadening dominates at high pressure and thus, it is particularly important at law altitudes. To illustrate the relative variation of the Doppler broadening and the pressure broadening, let us consider the lower 50 Km of the earth surface atmosphere, in this layer the pressure varies by three order of magnitude from (1 bar to 1 millibar) leading to a three order of magnitude variation in the line broadening due to pressure. In comparison the temperature varies by only 30% between 300 K° and 210 K° and this leads to a change in the line broadening due to temperature of only 14%. The drastic change in the pressure broadening of spectral lines allows the use of this effect for sounding of atmospheric properties as a function of the height. It should be noted that the doppler broadening is proportional to ν_0 thus the doppler effect will become particularly significant in the Visible and IR regions of the spectrum.

2.4.3 Nonresonant Absorption

The most common cause of absorption as a result of the slowly decaying wings of distant spectral lines. The wings of the absorption lines far away from the line center fall off even slower than the Lorenz profile, however, absorption does decrease significantly with pressure.

The two most used atmospheric windows in the Infrared are 3.5 μm to 4.1 μm and 10.5 μm to 12.5 μm the last is particularly important because it's centered near the peak emission of the blackbody radiation at a typical earth surfacer temperature.

The main source of absorption in the 11 μm window are the wings of CO_2 lines at 15, 10.4, 9.4 μm and the wings of the neighboring water vapor lines. The effect of CO_2 gas can be accurately modeled because it's uniformly mixed and have relatively constant distribution. The water vapor contribution is hard to model because of it's variability in space and time. For absorption coefficients:

$$\alpha_a = [gas\ volume\ mixing\ ratio]\frac{\nu^2 P^2}{T^2} \qquad (3.4.3.1)$$

Where: $\alpha^2 = Km^{-1}$

P = pressure in atmosphere

ν = frequency in Hz

$T = K^{\circ}$

Considering a layer of gas of thickness **dz** and density ρ the absorption coefficients through this layer is:

$$\alpha_{a} dz = \rho \alpha dz \qquad (3.4.3.2)$$

The amount of intensity reduction encountered by the electromagnetic wave of intensity I is:

$$dI = -\alpha dz I = -\rho \alpha \qquad (3.4.3.3)$$

Where: α_{a} = absorption extinction coefficient

α = absorption coefficient

2.4.4 Nonresonant Emission

If we consider an atmospheric layer of thickness dz and a temperature T, Thermal radiation will be generated following Plank's law

$$dI = \Psi_t dz = \alpha_a B(\nu,T)dz \tag{3.4.4.1}$$

Where: $B(\nu,T)$ is the Plank function

$$B(\nu,T) = \left[\frac{2h\nu^3}{C^2}\right]\left[\frac{1}{e^{\left(\frac{h\nu}{KT}\right)} - 1}\right] \tag{3.4.4.2}$$

Where: Ψ_t = the thermal source term

To point out the difference between the above equation and the Plank's constant equation as a function of the wave length

$$S(\lambda) = \frac{2\pi hC^2}{\lambda^5 \frac{1}{\exp\left(\frac{Ch}{\lambda KT}\right) - 1}} \tag{3.4.4.3}$$

The previous equation represent the spectral emittance, in order to do the comparison the following transformation carried on:

$$B(\nu)d\nu = B(\lambda)d\lambda$$

$$B(\nu) = \frac{\lambda^2}{C}B(\lambda)$$

One can come to the conclusion that the spectral radiance

B is related to the spectral emittance S by the following:

$$S = \pi B \tag{3.4.4.4}$$

In case of planetary atmosphere, the temperature and constituent density are function of the altitude Z, thus the thermal source term is expressed as:

$$\Psi_t(z) = \alpha_a(z) B(\nu, T(z)) \tag{3.4.4.5}$$

2.4.5 Wave Particle Interaction and Scattering

In the most simple case atmospheric particles can be considered as a small sphere. The rigorous solution for the scattering of a plane monochromatic wave by a spherical dielectric particle with a complex index of refraction n was derived by Mie. The expressions for the scattering cross section and the total extinction cross section are given by equations (3.4.5.1) and (3.4.5.2)

$$\sigma_s = \frac{\lambda^2}{2\pi} \sum_{m=1}^{\infty} (2m+1)\{|a_m(n,q)|^2 + |b_m(n,q)|^2\} \tag{3.4.5.1}$$

$$\sigma_E = \frac{\lambda^2}{2\pi}\sum_{m=1}^{\infty}(2m+1)e\{((a_m(n,q))+(b_m(n,q))\} \qquad (3.4.5.2)$$

Where the coefficients a_m, b_m are coefficients in the scattered field representing the contribution from the induced magnetic and electric dipoles, quadruples, and so on. These coefficients can be expressed in terms of spherical Bessel functions with arguments

$$q = \frac{\pi D}{\lambda}$$

Where: D is the diameter of the sphere. In the case of a small particle relative to the wave length (q<<1). The above scattering cross sections reduce to:

$$\sigma_s = \frac{2}{3}\frac{\pi^5 D^6}{\lambda^4}|K|^2 \qquad (3.4.5.3)$$

$$\sigma_E = \frac{\pi^2 D^3}{\lambda}m(-K) + \frac{2}{3}\frac{\pi^5 D^6}{\lambda^4}|K|^2 \qquad (3.4.5.4)$$

Where:

$$K = \frac{(n^2-1)}{(n^2+2)} \qquad (3.4.5.5)$$

The absorption cross section σ_a is given by:

$$\sigma_a = \sigma_E - \sigma_s \tag{3.4.5.6}$$

If the atmospheric unit volume contains **N** particles of equal size, the medium is then characterized by a particles extinction coefficient will be given by:

$$\alpha_E = \sigma_E N \tag{3.4.5.7}$$

If the scattering particles have a size distribution given by N(r) then

$$\alpha_E = \int \sigma_E(r) N(r) dr \tag{3.4.5.8}$$

Similar expressions can be written for scattering coefficient α_a and the absorption coefficient α_s, where multiple scattering can be neglected. When the wave scatters from a particle, the scattered intensity has an angular pattern called the phase function

$$P(\theta_i, \theta_s, \phi_i, \phi_s)$$

Where: the subscript **i, s** stands for incident and scattered respectively. In a simple terms. The phase function can be thought of as:

(1) The percentage of energy scattered per unit solid angle in a certain direction.
(2) An angular weighting function for the scattered radiation or,
(3) The equivalent of an antenna pattern

2.4.6 Wave Refraction

As a wave propagates in a medium, it's speed differs from the wave speed in vacuum due to interaction with medium constituents this is characterized by the medium index of refraction n, which equals the ratio of the wave speed in vacuum to the wave speed in the medium, thus n is always greater than unity.

In the case of a gas mixture of oxygen, water vapor and Carbon dioxide as in the atmosphere the index of refraction for frequencies less than 200 GHz given by:

$$N = (n-1)10^6 = 0.0776\frac{P}{T} + 373\frac{e}{T^2} \qquad (3.4.6.1)$$

where: e = is the partial pressure of water vapor in bar.
P = is the total pressure in bar.
N = is the refractivity.

Under mean conditions (P, e, T) decreases with height such that (N) decreases roughly exponentially with height, the atmosphere can be considered as a spherically immunogenic shell, A wave incident obliquely on the top of the atmosphere will refract and therefore has a curved trajectory as its propagates through the atmosphere.
This effect is used in occultation experiments to derive information about planetary atmospheres

2.5 Atmospheric Optical Thickness

Let us consider an atmospheric thin slab of thickness D an incident monochromatic wave will be partially scattered and absorbed as it propagates through the slab. If α is the total extinction efficient (including absorption and scattering), the intensity loss is:

$$\epsilon = -\alpha I \, dz \tag{3.5.1}$$

$$I(z) = I_0 \exp(-\alpha z) \tag{3.5.2}$$

At the output of the slab the intensity is:

$$I(D) = I_0 \exp(-\alpha D) \tag{3.5.3}$$

The slab is thus characterized by a transmission coefficient given by:

$$T = \exp(-\alpha D) \tag{3.5.4}$$

The term αD is usually called the slab optical thickness τ If the slab is immunogenic (i.e α varies with altitude Z) and covers the altitudes from Z_1 to Z_2, then the slab optical thickness is:

$$\tau(\nu, Z_1, Z_2) = \int_{Z_1}^{Z_2} \alpha(\nu, Z) dZ \tag{3.5.5}$$

and the slab transmission coefficient is given by:

$$T(\nu) = \exp(-\tau) \tag{3.5.6}$$

The total normal optical thickness of a planets atmosphere is given by:

$$\tau(\nu) = \int_0^\infty \alpha(\nu, Z)\ dZ \tag{3.5.7}$$

The optical thickness at altitude Z is defined as:

$$\tau(\nu, Z) = \int_Z^\infty \alpha(\nu, \zeta)\ d\zeta \tag{3.5.8}$$

In the case where the wave is oblique, at an incidence angle θ then:

$$\tau(\theta, \nu, Z) = \frac{\tau(\nu, Z)}{\cos\theta} \tag{3.5.9}$$

If the extinction coefficient decreases exponentially with altitude:

$$\alpha(\nu, Z) = \alpha(\nu, 0)\exp\left(\frac{-Z}{H}\right) \tag{3.5.10}$$

The optical thickness is then:

$$\tau(\nu, Z) = \int_Z^\infty \alpha(\nu, 0)\exp\left(\frac{-\theta}{H}\right)\ d\theta \tag{3.5.11}$$

$$\tau(\nu,Z) = H\alpha(\nu,0)\exp\left(\frac{-Z}{H}\right) \qquad (3.5.12)$$

Where:

$$\tau(\nu,0) = H\alpha(\nu,0) \qquad (3.5.13)$$

If an atmosphere consists of a mixture of gases and particles, the total optical thickness is equal to the sum of the individual optical thickness.

$$\tau = \sum_{g}\tau_g + \sum_{P}\tau_P \qquad (3.5.14)$$

The optical thickness is a parameter very widely used to characterized the atmospheres.

2.6 Radiative-Transfer Equation

The radiative transfer equation is fundamental equation describing the propagation of electromagnetic radiation in a scattering and absorbing medium. At a given point in the medium the change in intensity $I(Z,\theta,\phi)$ as the wave traverse a distance dz in the direction of (θ,ϕ) consists of the following elements. The wave is attenuated due to absorption

in the gas and the suspended particles. This is corresponds to change the wave energy to heat.
The corresponding intensity loss is given by:

$$\frac{dI}{dZ} = -\alpha_a \ I \tag{3.6.1}$$

Where : α_a is the sum of the absorption coefficient of all gases and particles in the medium. Some of the wave energy scattered by the particles, which results in a loss of intensity in the (θ,ϕ) direction even though the total wave energy is conserved.
The corresponding intensity loss is given by:

$$\frac{dI}{dZ} = -\alpha_S \ I \tag{3.6.2}$$

Some energy is added to the wave as a result of thermal emission from the medium, this source term is given by:

$$\frac{dI}{dZ} = \Psi_t(z) = +\alpha_a \ B(\nu,T) \tag{3.6.3}$$

Some energy is added to the wave in the (θ,ϕ) direction as a result of scattering of waves incident from other directions, this source term is given by:

$$\frac{dI}{dZ} = \Psi_S = \alpha_S(z)\ J(\theta,\phi) \tag{3.6.4}$$

Where:

$$J(\theta,\phi) = \frac{1}{4\pi}\int_0^{4\pi} I(\theta',\phi')P(\theta',\phi',\theta,\phi)\ d\Omega' \tag{3.6.5}$$

In the above expression **P** is the scattering phase function which describes the angular distribution of the scattered field; therefore the radiative transfer equation can be written as:

$$\frac{dI}{dZ} = -\alpha_a I - \alpha_S I + \alpha_S J + \alpha_a B \tag{3.6.6}$$

or in a more simplified form:

$$\frac{dI}{dZ} = -\alpha(Z)\ I + \Psi(Z,\theta,\phi) \tag{3.6.7}$$

Where the loss terms and the source terms are combined. The radiative equation is often written using the medium elementary optical thickness:

$$d\tau = -\alpha \, dZ \qquad as\ a\ variable$$

$$\frac{dI}{d\tau} = +I - \frac{\alpha_a}{\alpha}B - \frac{\alpha_S}{\alpha}J \tag{3.6.8}$$

or:

$$\frac{dI}{d\tau} = +I - (1-\omega)B - \omega J \tag{3.6.9}$$

Where: $\omega = \frac{\alpha_S}{\alpha}$

2.6.1 The Solution of a Nonscattering Plane Parallel Atmosphere Using the Radiative Transfer Equation

To illustrate let us consider the case of non scattering atmosphere where the geometry is parallel plane with wave propagating at an angle (θ) relative to the vertical axis, we assume the semi-infinite atmosphere is bounded at Z = 0, which also origin for the optical thickness variable $\tau = 0$

The radiative transfer equation can be written as:

$$\cos\theta \, \frac{\epsilon}{d\tau} = I(\tau,\theta) - B \tag{3.6.1.1}$$

$$\mu\frac{\epsilon}{d\tau} = I(\tau,\theta) - \Psi(\tau,\mu) \tag{3.6.1.2}$$

Where: $\mu = \cos\theta$ **and** Ψ **is the source term**

and $\Psi = \frac{\psi_\tau}{\alpha_a}$

The solution of the above equation is given by:

$$I(\tau,\mu) = A\exp\left(\frac{\tau}{\mu}\right) + \frac{1}{\mu}\int_{\tau}^{\tau_0}\Psi(\eta,\mu)\exp\left(\frac{\tau-\eta}{\mu}\right)d\eta \tag{3.6.1.3}$$

Where: A and τ_0 **are constant and** τ **varies from** τ **equal 0 to** τ **equal** τ_m **which is equal to the optical thickness of the total atmospheric layer. In the case of inward radiation from the atmosphere toward the surface, the total intensity level** τ **is given by**

$$I(\tau,\mu) = \frac{1}{\mu}\int_{\tau}^{\infty}\Psi(\eta,\mu)\exp\left(\frac{\tau-\eta}{\mu}\right)d\eta \tag{3.6.1.4}$$

In the case of the outward radiation toward the space then:

$$I(\tau,-\mu) = I(\tau,-\mu)e^{-\left(\frac{\tau}{\mu}\right)} + \frac{1}{\mu}\int_{0}^{\tau}\Psi(\eta,-\mu)\exp-\left(\frac{\tau-\eta}{\mu}\right)d\eta \tag{3.6.1.5}$$

If the observing point is above the atmosphere, then

$$I(\tau_m,-\mu)=I(0,-\mu)e^{-\left(\frac{\tau_m}{\mu}\right)}+\frac{1}{\mu}\int_0^{\tau_m}\Psi(\eta,-\mu)e^{-\left(\frac{\tau-\eta}{\mu}\right)}\,d\eta \qquad (3.6.1.6)$$

Where $I(0,-\mu)$ is the intensity of the upward radiation μ at the surface and τ_m is the total optical thickness of the atmosphere

2.7 Basic Concepts of Atmospheric Remote Measurements

The techniques of atmospheric sounding can be divided into three general categories[21]:

(1) Occultation
(2) Scattering
(3) Emission

(1) **Occultation:** The techniques of this approach is to measure the changes, that the atmosphere impinges on a signal of known characteristics as the signal propagates through a portion of the atmosphere. The signal source could be for example the sun or any other man made source

such as radio or laser or radar transmitter.

(2) **Scattering:** this technique uses the approach of measuring the characteristics of the scattered waves in a direction or directions away from the incident wave direction, the source again could be the sun or man-made one.

(3) **Emission:** If the radiation source is the atmosphere it self, and the sensor measures the spectral characteristics and intensity of the emitted radiation.

The different atmospheric sounding techniques aim at measuring the spatial and temporal variations of the atmospheric properties specifically Temperature profile, Constituent nature, Concentration, Pressure, density profile in the rest of this section the techniques used for measuring these properties are briefly described in order to give an over view of some of the methods used in the following sections.

2.7.1 The concept of temperature measurements

If a sensor measures the radiation emitted from gases whose distribution is well known, such as carbon dioxide or molecular oxygen in the atmosphere, then the radiance can be used to derive the temperature as in equation (3.4.4.5), by looking at this equation it seems that only the mean temperature can be derived because the radiation detected at any instant of time is a composite of wave emitted from all the different layers in the atmosphere, however we can measure the radiance variation as a function of frequency near a spectral line.

2.7.2 The concept of composition measurements

The identification of the atmospheric constituents is usually based on detecting the presence of a spectral lines associated with a certain molecules. The spectral signature is in effect the "fingerprint" of gaseous constituent. In order to determine the abundance of a constituent a more detailed analysis of the spectral signature is required, the line strength is usually related to the number density of molecules, this is usually requires knowledge of the local pressure and temperature, once the temperature is derived using the radiance from a homogeneously mixed constituent as discussed earlier.

2.7.3 The concept of pressure measurements

The total columnar absorption is strongly related to the columnar mass of a constituent in the atmosphere, particularly near a resonant line of the constituent. If the constituent is homogeneously mixed in the atmosphere its total mass is then directly proportional to the surface pressure. Thus, surface pressure sounding can be achieved by devising a technique to measure the total columnar absorption of homogeneously mixed gas such as oxygen in the atmosphere.

2.7.4 The concept of density measurement

The atmospheric refractivity N is directly proportional to the atmospheric density. Thus one approach is to derive the refractivity profile as a function of altitude. This done to drive the density profile of the atmosphere using the refraction of the radio communication signal as orbiting or flyby spacecrafts are occulted by the atmosphere. The occultation technique will be discussed in a later sections.

3 Atmospheric Remote Sensing in the Visible and IR

3.1 Introduction

Sensors in the visible and IR part of the spectrum are used to measure the characteristics of the solar radiation after it interacts with the atmosphere through scattering and absorption and of the emitted radiation which originates from the atmospheric molecules.

For these characteristics, information can be derived about atmospheric temperature, composition and dynamics as a function of altitude and lateral position. Because of the relatively short wavelength high spatial resolution is easier to achieve in comparison to microwave sensors.

Imaging spectrometry can be achieved by using two dimensional detector arrays. On the other hand, the strong scattering by suspended particles significantly limits vertical sounding through cloud layers.

3.2 Interaction of Visible and IR Radiation with the Atmosphere

In the visible and near infrared regions the sun is the main source of radiation. The maximum solar irradiance occurs at 0.47 μm with about half the total energy in the visible band (0.4 - 0.76)μm.

In the case of the earth atmosphere about 35% of the sunlight is reflected back in to the space, about 18% is absorbed in the atmosphere and 47% is absorbed at the surface[22].

The thermal infrared radiation is generated mainly by the surface and the atmosphere. It becomes dominant somewhere between (4 - 18)μm depending on the planets temperature and albedo (the ratio of the light reflected by a planet to that received by it). Atmospheric constituents interact with the electromagnetic radiation all across the visible and IR region as a result of vibrational and rotational processes, thus impinging their fingerprints on the spectral signature of the radiation emitted or scattered toward space.

3.2.1 Visible and Near-IR Radiation

As sunlight passes throughout an atmospheric layer. Some of the energy is absorbed and some transmitted. At the surface, the total spectral irradiance E_g contains two components:

(1) the direct sunlight E_s

(2) The diffused skylight E_d

$$E_g = E_S + E_d \tag{4.2.1.1}$$

The direct sunlight spectral irradiance is given by

$$E_S = S \cos\theta \exp\left(\frac{-\tau}{\cos\theta}\right) \tag{4.2.1.2}$$

where: τ = the total optical thickness of the atmosphere

S = the solar spectral irradiance at the top of the atmosphere

θ = the angle of incidence (or observation)

The diffuse skylight consists of all the components which result from single or multiple scattering of the direct sunlight as well as the reflected sunlight.

3.2.2 Thermal Infrared Radiation

The total thermal spectral radiance **I** observed at a frequency ν and zenith angle θ consist of:

$$I = I_S + I_a + I_d + I_h \tag{4.2.2.1}$$

where:

I_S = surface emission

I_a = atmospheric emission upward

I_d = reflected atmospheric emission downward

I_h = reflected solar radiance

The surface emitted radiance reaching the sensor can be written as:

$$I_S(\nu,\theta)=\epsilon_s(\nu,\theta)B(\nu,T_s)\exp(-\tau(\nu,\theta)) \qquad (4.2.2.2)$$

where: ϵ_s = the surface emissivity

τ = the atmospheric spectral optical thickness

$B(\nu,T_s)$ = the Plank's function

The atmospheric emission for a plane apparel atmosphere in local thermodynamic equilibrium is given by:

$$I_a=\int_0^\infty \Psi_t(\nu,z)\exp(-\tau(\nu,z))dz \qquad (4.2.2.3)$$

$$I_a=\int_0^\infty \Psi_t(\nu,z)\exp(-\tau(\nu,z))dz$$

where: $\Psi_t(\nu,z)$ = source term = $\alpha_a(z)B(\nu,T_a(z))$

T_a = atmospheric temperature

$\tau(\nu,z)$ = optical thickness above Z

$Z=\frac{1}{\cos\theta}\int_z^\infty \alpha_a(\nu,\zeta)d\zeta$

The reflected atmospheric downward emission I_d originates in the atmosphere above the surface and is reflected by the surface. The radiant energy reflected into the solid angle $d\Omega_r$ in the direction (θ_r, ϕ_r) comes from all directions above the surface.

$$I_d(\nu,\theta_r,\phi_r) = e^{-\tau(\nu,\theta_r,\phi_r)} \int dA \int d\Omega_i I'(\nu,\theta_i,\phi_i)\rho(\nu,\theta_r,\phi_r,\theta_i,\phi_i)\cos\theta_i \qquad (4.2.4.2)$$

Where: I' = the atmospheric downward radiation

at the surface

ρ = the surface rflectivity

$d\Omega_i$ = the solid angle of incident radiation

= $\sin\theta_i d\theta_i d\phi_i$

The second integral is over a solid angle of 2π, the first integral is over the area viewed by the sensor, the reflected solar radiance term is given by:

$$I_h(\nu,\theta) = S(\nu)\cos\theta_h e^{-\tau(\nu,\theta_h)}\rho(\nu,\theta_h,\theta)e^{-\tau(\nu,\theta)} \qquad (4.2.2.5)$$

where: θ_h is the sun angle and θ is the observation angle

$I_h = 0$ at night time.

3.2.3 Resonant Interaction

Resonant interactions with the atmosphere in the visible region and IR correspond mainly to the vibrational and vibrational rotational energy levels of the atmospheric considerations.

3.2.4 Effects of Scattering by Particulates

Particulates play major role in the visible and infrared region of the spectrum because they usually are of similar size as the wavelength. In order to formulate quantitively, the effect of the scattering. The angular distribution of the scattered radiation must be specified. This is described by the scattering phase function $P(\cos\alpha)$ where α is the angle between the incident and scattered radiation. Usually $P(\cos\alpha)$ is normalized such that:

$$\int P(\cos\alpha)\frac{d\Omega}{4\pi} = \omega \qquad (4.2.4.1)$$

For the case with no absorption loss $\omega = 1$ otherwise ω is a constant smaller than one.

The simplest case is when the scattering is isotropic then:

$$P(\cos\alpha) = \omega = constant \tag{4.2.4.2}$$

an important case is the Rayligh phase function:

$$P(\cos\alpha) = \frac{3}{4}(1 + \cos^2\alpha) \tag{4.2.4.3}$$

Another important function which has been used in planetary studies is:

$$P(\cos\alpha) = \omega(1 + x\cos\alpha) \tag{4.2.4.4}$$

where **x** is constant between (- 1, + 1).

In general the phase function can be written as a series of Legender Polynomials:

$$P(\cos\alpha) = \sum_{n=0}^{\infty} \omega_n P_n(\cos\alpha) \tag{4.2.4.5}$$

In the case where the atmospheric contains clouds or aerosols, the scattering source term in the radiative transfer equation becomes important. This term is expressed as:

$$J(\theta,\phi) = \frac{1}{4\pi}\int_0^{4\pi} I(\theta,\phi)P(\cos\alpha)d\Omega \tag{4.2.4.6}$$

where:

$$\cos\alpha = \cos\theta_i \cos\theta_s + \sin\theta_i \sin\theta_s \cos(\theta_s - \phi_i) \qquad (4.2.4.7)$$

and: $\theta_i, \phi_i, \theta_s, \phi_s$ are the spherical angular coordinates of the incident and scattered becomes respectively, the radiation transfer equation in the case of a plane parallel scattering nonabsorbing atmosphere can then be written as in equation (3.6.8).

$$\mu \frac{dI(\tau,\mu,\phi)}{d\tau} = I(\tau,\mu,\phi) - \frac{1}{4\pi}\int_{-1}^{+1}\int_0^{\infty} P(\mu,\phi,\mu_i,\phi_i) I(\tau,\mu_i,\phi_i)\, d\mu_i\, d\phi_i \qquad (4.2.4.8)$$

where: $\mu = \cos\theta$ and $\mu_i = \cos\theta_i$

the previous differential integral equations cannot be usually solved analytically, in simple cases it is solved by solving for the following related integrals:

flux integral: $F = \frac{1}{\pi}\int\int \mu I\, d\mu\, d\phi$

K integral : $K = \frac{1}{4\pi}\int\int \mu^2 I\, d\mu\, d\phi$

3.3 Downlooking Measurements

The upwelling radiation carries informations about the atmosphere temperature profile (emitted component), suspended particles (scattered component) and constituents.

By measuring the spectral characteristics of the upwelling radiation in certain bands of the spectrum, the above geophysical parameters can be measured.

3.3.1 General Formulation for Emitted Radiation

Considering a plane parallel nonscattering atmosphere, a layer of thickness dz at altitude z will have an emitted spectral radiance $\Delta B(z)$ given by the following relationship[23].

$$\Delta B(z) = \alpha(\nu,z)B[\nu,T(z)]dz \qquad (4.3.1.1)$$

where: $B[\nu,T(z)]$ is the Plank's function and α is the absorption coefficient, which is a function of the local constituent and atmospheric pressure. The contribution of the layer dz to the total spectral radiance emanating the atmosphere is then:

$$\Delta B_a = \Delta B(z)e^{[-\tau(\nu,z)]} \qquad (4.3.1.2)$$

where:

$$\tau(\nu,z) = \int_z^\infty \alpha(\nu,\xi)d\xi \qquad (4.3.1.3)$$

Thus:

$$\Delta B_a = \alpha(\nu,z)B[\nu,T(z)]\exp\left[-\int_z^\infty \alpha(\nu,\xi)d\xi\right]dz \qquad (4.3.1.4)$$

$$\Delta B_a = B[\nu,T(z)]d\beta \qquad (4.3.1.5)$$

where:

$$\beta(\nu,z)=e^{-\tau(\nu,z)} \qquad (4.3.1.6)$$

$\beta(\nu,z)$ is the transmittance of the atmosphere above level z The total spectral radiance observed by the sensor is:

$$B_t(\nu)=B_s(\nu)\beta_m(\nu)+\int_0^\infty B\{\nu,T(z)\}\frac{d\beta}{dz}dz \qquad (4.3.1.7)$$

$$B_t(\nu)=B_s(\nu)\beta_m(\nu)+B_a(\nu) \qquad (4.3.1.8)$$

where: $B_s(\nu)$ is the surface spectral radiance

$\beta_m(\nu)$ is the total atmosphere transmittance

$B_a(\nu)$ is the atmospheric spectral radiance

3.3.2 Temperature Profile Measurements

The atmospheric spectral radiance can be written as:

$$B_a(\nu)=\int_0^\infty B\{\nu,T(z)\}W(\nu,z)dz \tag{4.3.2.1}$$

where: $W(\nu,z)=\frac{d\beta}{dz}$ acts as weighting function sometimes it is convenient to use instead of z another altitude dependent variable such as pressure (P) or (Y = - ln p) in this case we will have the following:

$$B_a(\nu)=\int_{p_s}^{0} B\{\nu,T(p)\}\frac{d\beta}{dp}dp \tag{4.3.2.2}$$

$$B_a(\nu)=\int_{-\ln p_s}^{\infty} B\{\nu,T(y)\}\frac{d\beta}{dy}dy \tag{4.3.2.3}$$

let us consider the case of the homogeneously mixed constituent (such as Co_2 in the atmosphere).

The emission around a single collision broadened spectral line centered at ν_0 where:

$$K(\nu)=\frac{S}{\pi}\frac{\nu_l}{(\nu-\nu_0)^2+\nu_l^2} \tag{4.3.2.4}$$

Where: K(ν) = Lorentz shape function which describe the mechanism of line broadening result from pressure - induced collision and ν_l is the Lorenz width, it is related to the mean time between collisions t_c by the following relation

$$\nu_l = \frac{1}{2\pi t_c} \tag{4.3.2.5}$$

now in the wing of the line where $\nu - \nu_0 \gg \nu_l$

$$\alpha = \rho \frac{S}{\pi} \frac{\nu_l}{(\nu - \nu_0)^2} \tag{4.3.2.6}$$

$$\alpha = \rho \frac{S}{\pi} \frac{\nu_l(p_0)}{(\nu - \nu_0)^2} \frac{p}{p_0} \tag{4.3.2.7}$$

Where: ρ is the constituent concentration.

In the case of a homogeneously mixed constituent. The concentration ρ is proportional to $(-\frac{dp}{dz})$ thus:

$$\alpha = -b\,p \frac{dp}{dz} \tag{4.3.2.8}$$

where:

$$\tau = +\frac{b}{2} p^2 \tag{4.3.2.9}$$

thus:

$$\beta = \exp\left(-\frac{b}{2} p^2\right) \tag{4.3.2.10}$$

where: b is a constant which depends on the line strength and width, the concentration of the absorber and the observation frequency.

This is leads to a weighting function W(ν,y).

$$W(\nu,y)=\frac{d\beta}{dp}\frac{dp}{dy} \qquad (4.3.2.11)$$

then:

$$W(\nu,y)=b\,p^2\exp\left(-\frac{b}{2}p^2\right) \qquad (4.3.2.12)$$

The sensor measures the collected spectral radiance B_t at a number of frequencies ν_j , the measured values can be written as:

$$B_t(\nu_j)=\int_0^\infty B\{\nu_j,T(z)\}W(\nu_j,z)dz \qquad (4.3.2.13)$$

We should note also that the previous expression didn't include the surface component for simplicity[24]. The objective is to drive the temperature profile from the values of $B_t(\nu_j)$, by looking at equation (4.3.2.13) it is viewed as a nonlinear transformation from T(z) to B(ν) as in

$$B(\nu)=F\{T(z)\} \tag{4.3.2.14}$$

and the temperature profile is derived by performing an inverse transformation:

$$T(z)=F^{-1}\{B(\nu)\} \tag{4.3.2.15}$$

This is done in an interactive process that uses the fact that the weighting function has a maximum which depends on ν and that variations of T(z) around the maximum effect strongly I(ν), while the effect is small away from the location of the peak. The theory associated with the inversions techniques which called retrieval techniques[25].

3.3.3 Simple Weighting Functions

let us assume that the temperature varies slowly and monotonously as a function of z. The Plank's function can be approximated by:

$$B(\nu,T)=B(\nu,\overline{T})+\frac{\partial B}{\partial T}(T-\overline{T}) \tag{4.3.3.1}$$

The equation (4.3.2.1) can be written as:

$$S_a(\nu)=B(\nu,\overline{T})\int W(\nu,y)dy+\int\frac{\partial B}{\partial T}W(\nu,y)(T-\overline{T})dy \qquad (4.3.3.2)$$

This equation shows that the product $\left(\frac{\partial B}{\partial T}\right)W(\nu,y)$ is a direct weighting function of the temperature. In order to illustrate the concept in a simple analytical form, let us consider the simplified case where K is assumed to be weakly dependent or even independent of temperature and pressure, then we can write:

$$\alpha(\nu,z)=K(\nu)\rho(z) \qquad (4.3.3.3)$$

and

$$\tau(\nu,z)=K(\nu)\int_z^{\infty}\rho(\xi)d\xi \qquad (4.3.3.4)$$

assuming an exponential behavior for ρ with a scale high H then we get:

$$\tau(\nu,z)=K(\nu)\rho_0He^{-\frac{z}{H}} \qquad (4.3.3.5)$$

and

$$W(\nu,z)=K(\nu)\rho_0\exp\left[-\frac{z}{H}-K(\nu)\rho_0He^{-\frac{z}{H}}\right] \qquad (4.3.3.6)$$

Which is identical to the microwave weighting function except that it is now corresponds to the Plank's function The weighting function peak occurs at an altitude Z_m given by:

$$Z_m = H\log[\rho_0 H K(\nu)] \qquad (4.3.3.7)$$

3.3.4 Composition Profile Measurements

The constituent concentration profile appears explicitly in the expression of

$$\beta(\nu,p) = \exp\left[-\int_p^\infty K(\nu,p')dp'\right] \qquad (4.3.4.1)$$

Thus a mapping transformation can be applied to derive

$$\rho(p) \ , \ \rho(y) \ , \ \rho(z)$$

from a set of measurements $S_a(\nu_i)$ using equation (4.3.3.1), (4.3.3.2) which is usually done by iteration techniques; to illustrate let use assume a simple case of an optical thin atmosphere at the frequency of observation then:

$$\frac{d\beta}{dp} = K(\nu,P)\rho(p)\exp\left[-\int_p^\infty K(\nu,p')\rho(p')dp'\right] \qquad (4.3.4.2)$$

Where:

$$\frac{d\beta}{dp} \approx K(\nu,p)\rho(p) \tag{4.3.4.3}$$

Now looking at equation (4.3.2.1), which will change to be:

$$S_a(\nu) = \int_0^\infty \rho(p)W'(\nu,p)dp \tag{4.3.4.4}$$

where:

$$W'(\nu,p) = K(\nu,p)\beta[\nu,T(p)] \tag{4.3.4.5}$$

If T(p) is known or derived from emission measurements at other wavelengths. Then $W'(\nu,p)$ the weighting function is a known function of ν , p and $\rho(p)$ can be derived by the inverse transformation of equation (4.3.4.1). Sensors operating in the different part of the visible and IR spectrum, can be used to derive composition profiles by measuring the backscattering of the solar radiation. One can for example look at a simplified case, in which the sun straight behind the sensor and the atmosphere is infinitely deep so that the ground effect then can be neglected then the following measurement can be taken:

$$I(\nu,p)=I(\nu)\exp[-K(\nu)n(p)] \qquad (4.3.4.6)$$

where: $I(\nu,p)$ is the incident radiation at the pressure level p and $I(\nu)$ is the incident solar radiation at the atmosphere, $K(\nu)$ is the absorption coefficient per molecule of the gas and $n(p)$ is the number of molecules above the level of pressure p. The amount of radiation backscattered upward from the molecules in a layer where the pressure changes by dp around level p will be proportional to $I(\nu,p)$ and dp:

$$dI'(\nu,p) = aI(\nu,p)dp \qquad (4.3.3.7)$$

where: a is the proportionality factor

If the radiation pass a gain through the atmosphere above level p the resulting upwelling is then:

$$I'(\nu)=\int_0^\infty dI'e^{-K(\nu)n(p)}=aI(\nu)\int_0^\infty e^{-2K(\nu)n(p)}dp \qquad (4.3.4.8)$$

$$\frac{I'(\nu)}{I(\nu)}=a\int_0^\infty e^{-2K(\nu)n(p)}d(\ln p) \qquad (4.3.4.9)$$

Thus by measuring the ratio $\frac{I'(\nu)}{I(\nu)}$ at a number of frequencies ν_j that give different values of K it should also be noted that we can invert the above integral in equation (4.3.4.3) and derive the profile n(p)

3.4 Uplooking measurements

Uplooking geometry is used to sound the atmosphere by emission or occultation. In the emission case, the spectral radiance is given by a similar expression as in the down-looking geometry except the integration has to be carried along the line of sight and there is no contribution from the ground. In the accultation case. The sun or in some cases another source is used and the atmospheric absorptions has to calculated along the line of sight from the source to the sensor. In both cases measurement accuracy is significantly enhanced by the fact that the optical thickness of a finite layer is significantly larger in uplooking measurements than the downlooking geometry. This is allows the detection and study of minor constituents with extremely low concentration.

3.4.1 Uplooking Measurements by Emission

The total spectral radiance emanating from the atmosphere in a limb sounding geometry is expressed in a similar way as a downlooking sensor where the total radiance observed by the sensor is given by equation (4.3.1.7) except that the integration will be along the line of sight

$$B_t(\nu,h)=\int_{-\infty}^{+\infty} B[\nu,T(x)]\frac{d\beta(\nu,x,h)}{dx}\ dx \tag{4.4.1.1}$$

where **h** is the tangent height and:

$$\beta(\nu,x,h)=\exp\left[-\int_{x}^{+\infty}\alpha(\nu,\xi,h)d\xi\right] \tag{4.4.1.2}$$

The coordinate x is related to the altitude Z by:

$$(R + h)^2 + x^2 = (R + Z)^2 \tag{4.4.1.3}$$

usually h and Z are much smaller than R thus:

$$x = \pm\sqrt{2R(Z-h)} \tag{4.4.1.4}$$

by making the transformation from x to z equation (4.4.1.1) can be written as:

$$B_t(\nu,h) = \int_0^{\infty} B(\nu,T(z))W(\nu,h,z)\ dz \tag{4.4.1.5}$$

Where: $W(\nu,h,z)$ is a weighting function

Usually most of the contribution to the emission is from altitude close to h, thus one can rewrite equation (4.4.1.1) as:

$$B_t(\nu,h) \cong B[\nu,T(h)]\int_{-\infty}^{+\infty}\frac{d\beta(\nu,x,h)}{dx}dx$$

$$\cong B[\nu,T(h)][\beta(\nu,+\infty,h)-\beta(\nu,-\infty,h)$$

$$\cong B[\nu,T(h)][1-\beta_t(\nu,h)]$$

$$\cong B[\nu,T(h)]\epsilon_t(\nu,h) \tag{4.4.1.5}$$

where:$\beta_t(\nu,h)$: is the total atmospheric transmittance along the path. $\epsilon_t(\nu,h)$: is the total emittance.

Thus if we know T(h) we can derive $\epsilon_t(\nu,h)$ and hence the total absorber amount m(h) along the detection path.
For a uniformly mixed gas, we may write for the total constituent mass m(h) the following expression:

$$m(h) = C\int\rho(x)dx = C\int\rho(Z)\sqrt{\frac{2R}{Z-h}}dZ \tag{4.4.1.7}$$

where: C is the mixing ratio and $\rho(z)$ is the atmospheric density. The measurement of $B_t(\nu,h)$ as a function of h is acquired by scanning the field of the view of the sensor with a wide vertical plane or by using a sensor with a wide vertical field of view and a linear array of detectors in the sensor focal plane such as CCD camera.

3.4.2 Uplooking Measurements by Absorption

In the case of absorption, the sensor observes the spectral emission from a source (usually the sun) as the line of sight is occulted by the atmosphere this allows the measurements of the total transmittance $\beta_t(\nu,h)$ along the line of observation, and hence the total absorber mass m(h), to a first order the measurement does not depend on Knowing the temperature profile, as in the case of emission mode, on the other hand, absorption measurements can be done only during source occultaion as viewed from the sensor.

4 Detection Methods and the Principle of Sensor Choice

The average reflectivity of an atmospheric target or even a surface area over a wide band of the spectrum is basically a total signature of that target and it's surrounding. In the case of black and white photographs, it corresponds to the gray levels of the different pixels. In the case of color photography (true color or false color), it corresponds to the hue, brilliance, and saturation of the color. The signature is used to separate the composition of the target units and it's surrounding and to classify them into general categories. In some cases, identification can be achieved, such as in the use of color photograph to classify vegetated areas versus water, snow, and sand. The spectral signature corresponds to high resolution (spectrally) radiometric measurements over a fairly broad region of the spectrum. In this case, target units can be separated, classified, and identified based upon unique characteristic in their reflectivity spectrum, such as a diagnostic absorption band or combination of absorption bands, a diagnostic reflectivity change at a certain wavelength, or ratio of reflectivities in two separate spectral regions. The spectral signature is the most diagnostic tool in the remotely identifying the composition of a target or a target cloud. A trade-off exists between the spectral resolution, spectral coverage, radiometric accuracy and identification accuracy. The analysis of radiometric and spectral signatures in target studies can be divided into three general steps of increasing complexity namely detection and delineation, classification and identification [26].

4.1 Detection and Characterization

The first step in the analysis of multispectral images is to recognize an delineate areas with different reflectivity characteristics. This is can be done manually or with computers by simply delineating areas with image brightness within a certain range of values. In general, change in brightness is associated with changes in chemical composition of the target, or its physical properties (roughness, slope, etc.). Change in brightness can also result from changes in the illumination geometry or atmospheric conditions of the different atmospheric constituents[27].

In the case of multispectral images, the delineation process should take into consideration albedo variation in any one of the spectral channels. In many satiations, accurate characterization of image units is better done by using ratios of reflectivity in two different spectral bands.

This will allow the minimization of nonrelevant effects such as slope changes of a particular target. To illustrate, let us assume that the reflectivity of a certain target unit as a function of the wavelength λ and incident angle θ is given by:

$$R(\lambda,\theta) = g(\lambda)f(\theta) \tag{5.1.1}$$

If we consider two neighboring areas A and B of identical composition but having different slope aspect, then their reflectivity will be different at each and every spectral band. However, if we consider the ratio r at two separate bands

$$r = \frac{R(\lambda_1,\theta)}{R(\lambda_2,\theta)} = \frac{g(\lambda_1)}{g(\lambda_1)} \tag{5.1.2}$$

The effect of the slope change is eliminated and only the change in the composition is characterized. Characterization can also based on a number of other criteria, such as presence or absence of a certain spectral feature e.g., absorption line, reflectivity step, combination of lines, spectral slope at a certain wavelength.

The selection of a specific delineation criteria is usually based on experience and on an understanding of the spectral behavior of the objects, surfaces, covers, or constituents being studied.

4.2 Classification

The next step after Characterization is to classify units based on a set of criteria. Classifications extend not only to individual images, but also to a number of images taken at different times of the same area or of different areas. The classification criteria range from the most simple, all areas with identical reflectivity in a certain spectral band being put into the same class, to more sophisticated criteria, such as equality of the coefficient of polynomial type expansion of the spectral signature as a function of wavelength over a wide spectral range. Some intermediate criteria include specific spectral absorption bands, spectral response slope in specific spectral regions, or the presence of spectral features. With the advent of multispectral imaging systems with a large number of high resolution spectral bands, more sophisticated classification techniques are needed. One example of such a technique is the wave form analysis approach. In this case the natural spectral function $F(\lambda)$ is expanded into a polynomial series

$$F(\lambda) = \sum_{n=0}^{N} A_n P_n(\lambda) \tag{5.2.1}$$

The specific polynomial selected is based on experience in analyzing specific types of data. For instance, it was found that a Chebyshev polynomial expansion is very sensitive to the lower frequency information and filters out the higher frequency variations in the illuminating sun spectrum. The wave form analysis replaces the set of measurements points with the coefficient of the corresponding polynomial expansion, which reduce the number of variables needed to describe a data set.

4.3 Identification

The last step in the spectral analysis of imaging data is the unique identification of the classified elements. This requires a detailed knowledge of the spectral signatures of the constituents being sought, as well as of the other materials in the scene, and the development of a spectral signature library of all expected constituents. In an ideal case, if a certain constituent, or a family of component, is the only one which has a certain spectral feature, such as an absorption line at a certain wavelength, the identification becomes simple. The identification feature could be a single absorption line or an association of lines. As an example illustrating a constituent identifications on a pixel by pixel basis using imaging spectrometry the data acquired by an a CCD camera, which could allow the acquisition of the spectral region over a certain bandwidth, where each image pixel over that range can be clearly observed as different areas in the image with a variety of spectral responses. When compared to a set of reference spectra in a spectral library, the composition of each pixel can be identified. If a reference spectral library is not available, the surface pixels can be classified into areas of identical spectra, within a certain error margin. Then field checking in one single area of each class will allow complete identification of the constituents in the whole scene.

4.4 Passive Imaging Sensors

A large number of visible and infrared imaging sensors have been flown in space to study the earth and planetary surfaces. Imaging systems can be divided into three general categories: framing cameras, Scanning systems, and pushbroom imagers. Comparison of different imaging systems can be seen in Table 5.4.1 The framing camera takes a snapshot of an area of the surface or the atmosphere, which is then projected by a camera optics on a film, return beam vidicon (RBV), or two-dimensional array of detectors located in the camera focal plane. Framing camera systems have been used on most of the planetary missions, in a RBV large format camera. The scanning systems use a scanning mirror which projects the image of one surface resolution element on a single detector. The across-track scanning covers the imaged swath across the track. In some cases a limited number of detectors are used so that each scan covers a set of across-track lines instead a single one. The platform motion carries the imaged swath along the track. The major disadvantage of such system is the presence of moving parts and the low detection or dwell or stay time for each pixel. The pushbrooom imagers delete the scanning mechanism and use a liner array of detectors to cover all the pixels in the across-track dimension. This allows a much longer detector stay time on each surface pixel, thus allowing much higher sensitivity and a narrower bandwidth of observation[28].

4.4.1 Sensor Eelements

The main elements of an imaging system are sketched in Fig.5.4.1.1 The collector defines the maximum wave power that is available to the sensor. The maximum power is equal to the product of the collector area by the radiant flux density of the sensor altitude, of the wave incoming from the surface, the collector could be a lens or a reflecting surface such as a plane or curved mirror.

$$P_{\max} = A \times M \tag{5.4.1}$$

Where: $M = d\frac{\phi}{dA}$ radiant flux density watt/m^2 where M is emittance or E irradiance and $\phi = \frac{dQ}{dt}$ watt which is radiant flux and Q = Radiant energy in joule

Where $W = \frac{dQ}{dv}$ joule / m^3 which is radiant energy density. The focusing optics focus the collected optical energy onto the detecting element or elements (lenses and / or reflectors) for focusing, shaping and correcting the wave beam. The scanning element is only used only in some imaging systems to allow a wide coverage in the case where few detecting elements are used. When a large array of detecting elements or films are used, the scanning elements is usually not necessary. In order to acquire imagery at a different spectral bands, the incident wave is split into its different spectral components. This is achieved by the dispersive element, which could consist of a set of beam splitters / dichroics, a set of filters on a spinning wheel, or dispersive optics such as prism or grating.

The wave finally focused on the detecting element where its energy is transformed into a chemical imprint in the case of films or is transformed into a modulated electrical current in the case of array detectors or return beam vidicon.

4.5 Electro-Optic Detectors Selection

The detector transforms the incoming wave into a form of recordable information. The electro-optic detector which transforms the wave energy into electrical energy that is usually transmitted to digital recording medium. Electro-optic detectors are generally classified on the basis of the physical processes by which the conversion from radiation input to electrical output is made. The two most common ones are thermal detectors and quantum detectors[29].

Thermal detectors rely on the increase of temperature in heat sensitive material due to absorption of the incident radiation. The change in temperature leads to change in resistance or voltage with a thermocouplers usually using thermoelectric junctions, which can be measured. Typically, thermistor bolometers use carbon or germanium resistors with resistance change of about 4% per degree. Thermal detectors are usually slow, have low sensitivity, and their response is independent of the wavelength. They are not commonly used in modern remote sensors.

Quantum detector use the direct interaction of the incident photon with the detector material which produces free charge carriers. They usually high sensitivity and fast response but they have limited spectral region of response are characterized by a parameter D^* which is equal to:

$$D^* = \sqrt{\frac{A\Delta f}{NEP}} \tag{5.5.1}$$

Where: A is the area detector

Δf is the circuit bandwidth

NEP is the noise equivalent power.

These detectors are classified into three major categories: **photoemissive, photoconductive and photovoltaic.**

In **photoemissive detectors,** the incident radiation leads to electron emission from the photosensitive intercepting surface. The emitted electrons are accelerated and amplified. The resulting anode current is directly proportional to the incident photon flux. These detectors are usually operatable at a wavelengths shorter than 1.2 μm because the incident photon must have sufficient energy to overcome the binding energy of the electron in the atom of the photosensitive surface. This is expressed by the Einstein photoelectric equation:

$$E = \frac{1}{2}mv^2 = h\nu - \phi \qquad (5.5.2)$$

Where: ϕ = work function = energy to liberate an electron from the surface and m is the electron mass, and v is the velocity of the ejected electron. Thus ϕ must be less than $h\nu$ in order to liberate an electron.

The critical wavelength of the incident wave is given by:

$$\phi = h\nu_c$$

then: $\nu_c = \frac{h}{\phi}$ and since $\nu = \frac{c}{\lambda}$ then one can say:

$$\lambda_c(\mu m) = \frac{4.135\times 10^{-15}(eV\cdot \text{sec})\times 3\times 10^{14}\left(\frac{\mu m}{\text{sec}}\right)\left(\frac{\mu m}{\text{sec}}\right)}{\phi(eV)}$$

$$\lambda_c(\mu m) = \frac{1.24}{\phi(eV)} \tag{5.5.3}$$

The lowest ϕ for photoemissive surfaces is for alkali metals. Cesium has the lowest ϕ = 1.9 eV, which gives $\lambda_c = 0.64\mu m$ lower values of ϕ can be achieved with composite surfaces. For instance, for a silver-oxygen
composite $\phi_c = 0.98 eV$ and $\lambda_c = 1.25\mu m$

In **photoconductive detectors,** incident photons with energy greater than the energy gap in the semiconducting material produce free-charge carriers which cause the resistance of the photosensitive material to vary in inverse proportion to the number of incident photons. This requires substantially less energy than electron emission, and, consequently, such detectors can operate at a longer wavelength in the thermal infrared.

In **photovoltaic detectors,** the light is incident on a p-n junction modifying its electrical properties, such as the backward bias current.

The Quantum detectors can also be built in arrays. This feature allows the acquisition of imaging data without the need of scanning mechanisms which are inefficient and provide short integration time per pixel. The most advanced imaging sensors been developed in the detector arrays is the charged coupled devices (CCD) which I will be discussing in more details in incoming sections.

4.6 Camera Systems for Remote Sensing.

In this section I will try to describe the two types of camera systems most frequently used in remote sensing applications. Before acquiring standard video signal format data, I found it important to design an acquisition system best suited to our applications. It was necessary to gain a fundamental understanding of the data-acquiring sensors in order to develop or utilize the algorithms which would be supported by the image processing systems performing the analyses[30].

4.6.1 Vidicon-based Systems:

Vidicon tubes are frequently utilized to acquire imagery in remote sensing applications ranging from planetary exploration to ground-based television image acquisition. The main component in a vidicon system is a glass tube containing a scanning electron beam mechanism with a photosensitive surface at the end opposite the electron beam source. The photosensitive surface is designed to produce a buildup of electric charge on the back surface, proportional to the amount of light falling on the front (outer) surface of the photosensitive material. The back surface is flooded with electrons before image exposure, producing a uniform saturated charge distribution. When the image is focused on the front surface of the material. The resultant charge distribution is characterized by a high number of electrons in the dark regions of the image and a low number of electrons in the lighter regions. The scanning electron beam then scans the charge distribution line by line. The scanning beam replaces the electron charge in the regions where the charge was depleted by exposure to light. The fluctuations in the electron beam current caused by replacement of the depleted charge are proportional to the light intensity, and the fluctuating beam current read out through load resistor. The sequential scanning produces a series of lines of analog data. The analog signal is sampled a fixed number of times for each scan line and then is digitized. This process produces a two-dimensional digital image that is then available for computer processing.

Vidicon systems are available with a variety of spatial resolutions. Most of vidicon systems provide at least 512 scan lines, with 512 point digitized per scan line.

A variety of scanning speeds are also available, and the choice of photosensitive material used in a vidicon system is often based on the desired scanning speed. A system in which the charge distribution is read out over a period of many seconds requires a photosensitive material that will retain the charge intensity and special location for that period of time. Faster scanning requires material that will not retain the charge distribution for a long periods of time.

Vidicon systems can be troubled by residual image problems because of the need to retain the charge distribution long enough for the image-scanning process to be performed. The retention capability may cause incomplete readout of the charge distribution, and a portion of the charge distribution may then be present in the next image that is scanned. Residual image problems are usually reduced significantly by saturating the surface with electrical charge between exposures.

Vidicon systems often introduce a variety of artifacts into imagery. The scanning electron beam is not perfectly linear, and some geometric distortion is often introduced by vidicon systems as a result of nonlinear scanning of the charge distribution. The electron beam can also be deflected towered or away from high-contrast boundaries in the charge distribution during scanning (caused by high contrast detail in the scene). This effect can introduce local geometric distortion at locations within the scanned image. Vidicons may also introduce artifacts into scanned imagery because of defects, or blemishes, within the photosensitive material used to acquire the imagery. The degree of charge retention may also not be uniform within the photosensitive material, and addition charge depletion, or "leaking," can occur during the scanning process. If a few seconds is required to scan the charge distribution, the charge at the lower regions of the image may deteriorate somewhat before the electron beam arrives at that area to replace the depleted charge. It is possible to compensate for some of these distortions with computer processing; techniques for distortion removal are many and often make the process of the analysis more complicated, due to the need for developing the right algorithms for fast and accurate analysis[31].

4.6.2 Charge Coupled Devices (CCDs):

CCDs are emerging as important components in image acquisition systems. A CCD is a solid-state imaging device utilized for a variety of remote sensing applications. It can be viewed as a fixed array of potential wells on a small square or rectangular solid-state surface. Each well accumulates electrical charge proportional to the incident light intensity at each well position. An image is acquired by exposing the array to a desired scene. The exposure creates a two dimensional distribution of electric potential stored within each of the potential wells. The digital image is acquired by reading and digitizing the potential stored within each well. CCD types: There are two important types of charge-coupled devices[32]:

(1) Surface channel CCDs

(2) Bulk channel CCDs

The surface channel CCDs transfer the signal charge in a potential well at the surface of the semiconductor body at the interface of the silicon and silicon dioxide. The device are considered "charge coupled" because the depletion regions on the silicon surface overlap so that, the potential wells merge or couple. An electrical consequence of such coupling, is that any mobile minority charge carriers accumulate in the region of the highest interface potential.

The peristaltic CCD is an epitaxial or ion implanted silicon layer is employed so that the maximum potential does not lie at the silicon dioxide interface but in the bulk silicon itself. The mobile minority carriers then reside at the potential maximum in the interior of the silicon. The transfer electrodes then function to modulate the channel potential for changing the level of the potential wells.

The basic principle of the CCD imaging: As an optical imaging device the CCD analog shift register may be used to collect and read out optically generated signals The basic structure is illustrated for an N-channel array. An optical system is used to focus an image (depicted as a single spot) on the front face of the CCD. Initially, anyone set of electrodes, for example, is held at the positive clock voltage, thus creating a potential well under each of these electrodes; the other electrodes are held at zero volts or small resting potential. Photons entering a silicon substrate, either through or between the electrodes (depending on the electrode material), generate electron-hole pairs by virtue of the photoelectric effect. The minority carriers (electrons) generated within the depletion regions or within a minority carrier diffusion length of the depletion regions, are collected under each electrode. The number of electrons collected under a given electrode within a given period of time, usually called the integration period is proportional to the local light intensity. Thus the pattern of charge that collects under the electrodes is an analog replica of the light intensity across the original image. The end of the integration period the charge is read out by clocking the array in a conventional manner, care being taken to ensure that the clocks run long enough to clear out every charge packet. Fig.5.6.2.2 shows the single output pulse that would ideally result from imaging a light spot. At the end of the readout period the device is again switched to the integration mode and the cycle is repeated. During the readout period light still incident on the array. The signal is sent to A/D converter (interface) after being readout from the CCD image sensor, then go through personal computer to finish the measurement as shown in Fig.5.6.2.3

5 Video Digitizer and Design Consideration

In order to enable computer processing of data acquired by the camera systems. A variety of devices have been designed to convert conventional video signals from analog to digital format. A video signals are analog signals that are acquire in a fixed format. A video signal is composed of a sequence of images that are transmitted to a viewing monitor at a rate of 30 images (or frames) per second. Each of the component images is composed of a fixed number of lines of analog signal data "(NTSC format requires 512 points per line)". An analog video signal with a frame time of one thirtieth of a second constitutes a high data rate signal. If a single frame of standard NTSC video data is converted to digital format. A digital image of size 512 samples by 525 lines will be generated. The analog video data is refreshes every one thirtieth of a second (1/30) and this is an effective data rate of approximately (6 Mbytes) per second (assuming one byte per pixel)[33].

The basic idea of video digitizing involves "freezing" and then digitizing a frame of video. Most computing systems cannot acquire a stream of digitized video pixels at a 6 Mbyte per second data rate, and some form of rate buffering is required. Rate buffering is a process through which high rate data are stored in an intermediate storage device as they are acquired at a high rate and then readout from the intermediate storage at a lower data rate that can be accommodated by the next device that must access the data.

The computer system that is used for subsequent digital processing then reads out the digital frame buffer at a lower data rate (typically 2 Mbytes/sec or less for most computer systems). The digitized data rate are transferred at the lower rate from the digital frame buffer to another auxiliary peripheral storage, where they can be accessed for further computer processing. The frame buffer is then available to receive another digitized video image. This type of device is often called a frame grabber. Other video digitizing systems perform rate buffering by slowing down the analog-to-digital conversion process to a speed at which several video frames rather than a single frame are digitized. As an example, the data rate can be slowed to one fifth. The input analog signal rate by digitizing the first one fifth of the video frame, then the second one fifth of the video lines from the next frame, etc. for a 525 line video signal, lines 1 to 105 of the digital image would be derived from the first analog video frame, lines 106 to 210 would be derived from the second video frame etc. The video digitizers that operate at rates less than one thirtieth of a second per digitized frame all utilize more than one video frame for digitizing. Some perform digitizing of blocks of sequential lines from sequential frames and others digitize sequential columns of pixels from sequential frames These slower digitizer are less expensive than frame grabbers but can be used only in applications in which the scene does not change rapidly between successive video frames.

Imaging system design considerations:

Several fundamental decisions must be made during the design of image acquisition devices these decisions concern the number of intensity levels to be recorded in each spectral band, The number of spectral bands in which imagery is to be acquired. The spatial resolution that will be preserved in the sampled digital imagery, the size of the output digitized images, etc. Complex trade off studies are required before each of these parameters can be established for a particular image acquisition device to provide an insight into the decision processes faced by a system designer in designing image acquisition hardware, the following is a description of the three main areas in which design decisions are required[34].

Radiometric Resolution :

All image acquisition devices provide a range of discreet digital intensity levels that correspond to the brightness of the scene sampled by the image acquisition device. The fundamental parameter that determines the radiometric accuracy or precision of digitized intensity values is the number of bits per picture element "pixel" that is selected to represent the scene brightness in the sampled image. If only 3 bits per picture element are utilized, the sampled imagery will contain only seven discreet levels if 8 bits per pixel are quantized, 255 possible digitized intensity values will be provided by the system. The full dynamic range of the analog signal is displayed as a vertical bar at the Fig.6.1 if one bit is used to digitize the analog signal, a zero or one will be produced by the digitizer. The only intensity information provide by One bit system would be wether the analog signal is above or below midpoint of the full dynamic range. If two bits are used, the analog signal could be determined to a resolution no better than one quarter of the total dynamic range. From the Fig.6.1 it illustrates the increasing precision to which the analog signal can be represented by digitized intensity values as more bits are used to quantize the input signal. For the input analog signal level V - shown in Fig.6.1 a one-bit digitizer will produce a value of zero. a two-bit digitizer will produce a binary value (01) corresponding to decimal value of one with a total possible range from (0 - 3) a 3 - bit digitizer would produce a binary value of (010 - decimal 2) within a range from (0 to 7), etc. 8 - bit digitizer would produce a binary value of 010.....0 for input signal level denoted by V , and 8 - bit quantizing would yield a digital range of values extending from (0 to 255). The trade off involved in determining the number of bits per pixel to be by an image acquisition system involve the radiometric resolution required for a particular application, the communication data rate, and data storage capacity. The larger the number of bits digitized per pixel, the longer the digital transmission of image data will take, and the more digital storage will be required to store the imagery. The 8-bit bytes are standard addressable units of storage in many current digital computer systems and it's quit common to utilize 8-bits per pixel in digital images. Even when the image acquisition system utilizes a sensor that is incapable of resolving 255 brightness levels in the original scene

Spatial resolution :

The image acquisition system optics constitute an important component in determining the smallest spatial resolution that can be detected by a particular digital system. A second component is sampling frequency with which the continuous spatially distributed analog image is sampled. The analog intensity levels present across one line of an image that is being sampled by a digital system. Individual pixel intensity values are read from the analog signal and converted to digital intensity values are read from the analog signal and converted to digital intensities at a discrete set of points along the line. One choice of sampling frequency a digitized pixel intensity value will be acquired at each position indicated by an arrow in Fig.6.1, the spatial resolution present in a sampled digital image is a function of the frequency at which the analog signal values are sampled, following the Nyquist theorem which stated that a continuous signal can be reconstructed perfectly up to a particular spatial frequency from a set of discrete samples if the sampling is performed at twice the frequency of interest. As an example of the use of Nyquist theorem. If we consider an image acquisition system with an optics system that provides a net scaling factor from object space to focal plane of 10^4:1 this system will cause an object 100m across in object space to be reduced to an image of size 1 cm in the focal plane. Now suppose that a particular application requires that the objects or future of size as 2m must be resolvable in the digitized imagery produced by the system a 2m object will be reduced to a size of 0.02 cm in the focal plane because the optics scaling factor (0.02cm = 2m x 1cm/100)m. The Nyquist theorem indicates that the focal plane must be sampled at twice the desired spatial frequency. In this case we wish to preserve objects as small as 0.02 cm in the focal plane, and so sampling must occur at twice this frequency, or every 0.01 cm in the focal plane. The size of the output digital images is often determined by the spectral resolution requirements imposed on the imaging system, in the above example if it were required to scan a 100m area in object space at 2m resolution conversion to the focal plane dimensions indicates that an image of size 100 x 100 pixels will be required.

Spectral resolution:

In designing an image system one must determine the number of spectral band in which an image is to be sampled. The selection is a function of the particular application, for a broad band sensor covering the visible to the near infrared one can allows using the right filter select the proper spectrum suitable for specific application with different spectral resolution capability which will have a strong influence on the acquisition system design considerations. Since each spectral band added to the system can conceivably add a full-size image component to every multispectral set of image components being acquired.

6 Differential Absorption Schemes (DASE)

The differential absorption technique used to determine the concentration of an atmospheric pollutant at a distance R Fig.7.1 over a path length ΔR, is based on the use of two physical effects of interaction of radiation with a medium, light scattering and light absorption. The backscattered signals depend on the scattering and absorption properties of the atmosphere. The difference in return signals is caused by the differential absorption effect due to absorption differences of the pollutant molecules at different wavelengths.

By comparing the relative attenuation of the elasticely backscattered signals at two close-lying laser wavelength λ_1 and λ_2 the first of these wavelengths is selected to correspond to an absorption peak of the pollutant to be measured, while the second is selected to correspond to an absorption trough as shown, for example, in Fig.7.1 for Nitrogen dioxide NO_2. The attenuation of the two colinear laser beams, as they traverse the sample length, are due to two factors: the wavelength selective absorption by the pollutant, and the elastic scattering by the atmospheric molecules (Rayleigh scattering), and by particles (Mie scattering). The attenuation due to elastic scattering can be assumed to be the same for both wavelengths, if they are close enough, and hence the relative absorption of the two laser signals will be due to the concentration of pollutant molecules in the path.

The pollutant molecular concentration is thus essentially determined by an absorption method, which has the potential for high accuracy, in that only relative measurements are required of the relative attenuation of two colinear laser beams as they traverse the sample length ΔR. This relative attenuation is easily detected, since it is determined from comparison, at the optical receiver, of the elasticaly backscattered signals, at the same wavelengths as the transmitted signals. Since the elastically backscattered signals are relatively large, compared with, for instant, Raman or florescence backscatter, and since the bandwidth of the optical receiver can be made very narrow, only sufficiently large as to match the bandwidth of outgoing laser signals, the signal to noise ratio of the system can be greatly improved, permitting excellent detection sensitivities with the DASE system. These are typically three orders of magnitude better than can be achieved with the resonance or Raman schemes.

In previous work at the City College, the DASE LIDAR system has in fact been demonstrated to be capable of, to a large extend achieving its expected potential, in terms of determining concentration and spatial distribution of atmospheric molecular pollutants at ranges (10 Km), concentration levels (10.05 ppm), and spatial resolutions (100 m) of practical interest to urban pollution monitoring. However, the DSAE system is still a lidar system , which means it obtains the pollution concentration along the path of outgoing lidar beam. To obtain a more complete view, it is necessary for the laser beam to scan the seen being viewed, and at sufficiently to ensure that different parts of the frame being scanned reflect the reality of the changing situation. While in theory this is possible, in practice the high powers need for the laser, and the complexity, cumbersomeness and high cost of such a scanning lidar system and receiver have drastically restricted its practical applications.

It is to meet the needs of the environmentalists for a system to provide, at reasonable cost and practicality, an approximate picture of the pollution conditions affecting a scene and region being observed, That the computed imaging topology technique approach now being proposed, was conceived.

7 Imaging Detection of Atmospheric Molecular Pollution

7.1 Theory

The basic approach for the proposed imaging differential absorption scheme is shown schematically in Fig.8.1.1. It determines the total pollution along any line of sight being viewed, Eg A-B, by measuring the relative attenuation of the sunlight, or any other light, being reflected by any target at the end of the line, B, at each of the two close lying wavelengths, each corresponding respectively to an absorption peak and trough of the pollutant being monitored.

The relative attenuation is determined, as in the case of DASE lidar, by comparing the amount of reflected light received from the point in question (B), at each of the two wavelengths. This comparison is made by viewing the scene being monitored, alternately through two narrow band filters, each matching one of the absorption (peak or trough) lines of the pollutant molecule being monitored. These viewing are made simultaneously through two video cameras, or sequentially through one camera, if the frames succeed one another before the scene being viewed has time to be changed substantially.

The comparison of the received signals at each of the wavelengths, at each point of the frames being viewed would be carried out by appropriate electronic processing of the signals, and subsequent video display of the result. To better understand the technique being proposed, and to obtain an appreciation of the accuracies that may be achieved by it, and it is necessary to examine optical absorption processes in the atmosphere, and the effect of the molecular pollutants on them.

7.2 Detection Limitations of the Passive System

To examine the system we construct a model with certain constrains for easier calculations. To clear the complexity of the detection problem we will assume the following :

1- The differential return signal is defined as the difference between the signal with a target gas and the signal without a target gas .

2- The calculation is done at a single frequency for convenience

3- the target compound was assumed to have a peak absorption of $1x10^{-3}$ m^2/mg (a cross section of $3.5x10^{-18}$ cm^2) at 4500 $\mathring{A}$ which is typical value for the No_2 "the gas in question"

Given a cloud of target gas pollutant at a given distance from the CCD as our sensor Fig.9.1.1, that totally fills the field of view (FOV) of the CCD . The radiance incident on the CCD is the result of radiances from :

(1) The background (assumed to begin immediately behind the target cloud)

(2) The target cloud

(3) The intervening atmospheric gases

The radiance from an infinitesimal layer "assumed to be at the temperature of the gas target" is

$$N = \int_0^x [K_T(\lambda)N_x(\lambda) - K_T(\lambda)N_x^{'}(\lambda) + K_A(\lambda)N_x(\lambda) - K_A(\lambda)N_x^{'}(\lambda)]dx \qquad (8.2.1)$$

Where:

K_T = extinction coefficients of the target gas.

K_A = extinction coefficients of the atmosphere.

N_X = radiance of the blackbody at temperature of the infinitesimal layer.

N\` = radiance incident on the infinitesimal layer traveling to the CCD.

x = length variable which integrated for range (R) and target cloud length (L).

All the above variables are functions of the wavelength, assuming homogeneous atmosphere and target cloud species . Integrating the above equation gives the power incident on the CCD assuming that R >> L gives:

$$P_p = \left[e^{-K_A R} e^{-K_T L} N_{BG} + (1 - e^{-K_A R} e^{-K_T L}) N_T\right] A_c \Omega_x \qquad (8.2.2)$$

Where : R = the distance to the target cloud

L = the length of the target cloud (m).

A_C= the collector area of the CCD camera.

Ω_x= the solid angle of the acceptance of the CCD

N_{BG}= the radiance of the background

N_T = the radiance of the blackbody at the temperature of the target background

setting $T_A = e^{-K_A R}$ and $T_L = e^{-K_T L}$ in equation (8.2.2) gives

$$P_p = [T_A T_T N_{BG} + (1 - T_A T_T) N_T] A_c \Omega_x \qquad (8.2.3)$$

where: T_A = the atmospheric transmittance

T_L = the target cloud transmittance

and $K_T = \alpha_T C$

where: αT= the absorptivity of the target

C = the concentration of the target cloud (mg/m^3)

In equation (8.2.3) if the radiance of the background equal the radiance of the blackbody of the target cloud i.e

$$N_{BG} = N_T \tag{8.2.4}$$

If we substitute equation (8.2.4) in equation (8.2.3) we obtain

$$P_P = N_{BG} A_c \Omega_x = N_{BG} A_c T_o \tag{8.2.5}$$

Where: T_O = the transmittance of the optics

Looking back at equation (8.2.5) one can see easily that the incoming radiation contains no information about the spectral properties of the gas in question, which set the condition from equation (8.2.4) for the detection to happen as:

$$|N_{BG} - N_T| = \Delta N > 0 \tag{8.2.6}$$

The interpretation of this condition to some degree depends on the constraints of the model. In this case, the spectral range needed to monitor the target cloud is sufficiently small compared to variations in the CCD sensitivity. Another requirement of (8.2.1) is that the pollutant cloud should fall in the field of view (FOV) of the CCD, this would make the signal returned from the target cloud not $\left(\frac{1}{R^2}\right)$ dependent. However the signal still depends on atmospheric transmittance $T_A = e^{-K_A R}$ which is itself range dependent.

7.3 Analysis of Optical Propagation and Absorption in the Atmosphere

The atmosphere attenuates a transmitted optical beam by elastic (Rayleigh, Mie) and inelastic scattering, and molecular absorption. Transmittance of radiation in the atmosphere is complicated by the dependence of scattering and absorption on a number of different physical properties of the atmosphere. In general, for propagation of monochromatic radiation of intensity I(r), along an atmospheric path, the attenuation is given by [14]:

$$I(r) = I_o \exp\left[-\int_0^r \alpha \, dr\right] \tag{8.3.1}$$

Where I(r) is the intensity at distance r from the source, and α is the atmospheric volume extinction coefficient at r given by :

$$\alpha = \alpha_R + \alpha_M + \alpha_A \tag{8.3.2}$$

where : α_R = Rayleigh absorption coefficient

α_M = Mie absorption coefficient

α_A = molecular absorption coefficient

The Rayleigh extinction coefficient,α_R, is related to the wavelength, by :

$$\alpha_R \sim \left[\frac{1}{\lambda^4}\right] \tag{8.3.3}$$

While an empirical relationships for the Mie extinction coefficient is given by :

$$\alpha_M(\lambda) = \left(\frac{3.91}{V}\right)\left(\frac{0.55}{\lambda}\right)^{0.583^{\frac{1}{3}}} Km^{-1} \tag{8.3.4}$$

Where : V is the visibility.

Values of Rayleigh and Mie extinction coefficients are given in Table 8.3.1. As can be seen from Table 8.2.1, at the wavelengths of interest to pollution monitoring, ranging from approximately 300 nanometers to 600 nanometers, and for typical visibilities of 10 Km or less, Mie scattering predominates over Rayleigh. Thus, the typical wavelength changes between an absorption peak and an absorption trough in, for example Nitrogen Dioxide, of approximately 0.15 nanometers, in the 450 nanometers spectral range, would , according to equation (8.1.3) above, cause a change in extinction coefficient of approximately 0.3 %. In this context, it should be noted that a visibility of 10 Km, means that based on the values of Table 8.2.2, the transmission coefficient for light at 450 nanometers over a distance of 5 Km is 15 %, and a change of 0.3 % in the extinction coefficient would cause a change of approximately 0.15 in this 15% transmission, or 1% of that value. Thus, the changes in transmission due to the effect of wavelength change on Mie scattering would mask changes in pollution concentrations that caused changes in transmission of less than 1%, between both the wavelengths being probed. As will be seen in the discussion below, this is an insignificant barrier to the applications of the technique to the measurement of even relatively low level of ambient pollutants.

Equation (8.1.1) can be written as:

$$I = I_0\left(\exp\left[-\int_0^r (\alpha_R+\alpha_M)dr\right]\right)\left(\exp\left[-\int_0^r (\alpha_A)dr\right]\right) \quad (8.3.5)$$

Thus, the ratio of intensity received from equal sources at λ_1 and λ_2 I_2 , I_1 at a range L is given by the following relation :

$$\frac{I_1}{I_2} = \left(\frac{\exp\left[-\int_0^r (\alpha_{R1}+\alpha_{M1})dr\right]}{\exp\left[-\int_0^r (\alpha_{R2}+\alpha_{M2})dr\right]}\right)\left(\frac{\exp\left[-\int_0^r (\alpha_{A1})dr\right]}{\exp\left[-\int_0^r (\alpha_{A2})dr\right]}\right) \quad (8.3.6)$$

If the two wavelengths, λ_1 and λ_2, are close lying, then, as seen in the earlier discussion, the attenuation due to elastic scattering will be approximately the same for both of them, and the first two terms of equation (8.3.6) above will cancel, leaving

$$\frac{I_1}{I_2} = \exp\left(-\int_0^r (\alpha_{A1}+ \ \alpha_{A2})\,dr\right) \quad (8.3.7)$$

which can be written in terms of the absorption cross-section for the pollutant molecules, $\sigma_{abs}(\lambda_1)$, and $\sigma_{abs}(\lambda_2)$, at each of the wavelengths, and the molecular concentration N(r) at a range r , as

$$\frac{I_1}{I_2} = \exp - \int_0^r [\sigma_{abs}(\lambda_1) - \sigma_{abs}(\lambda_2)] \cdot N(r) \; dr \qquad (8.3.8)$$

$$\frac{I_1}{I_2} = \exp - \int_0^r [\sigma_{abs}(\lambda_1) - \sigma_{abs}(\lambda_2)] \cdot N(av) \cdot L \; dr \qquad (8.3.9)$$

Where N(av) is the average molecular pollutant concentration over the total viewing range, L from which :

$$N(av) \cdot L = \ln\left\{\left(\frac{I_1}{I_2}\right)\left(\frac{1}{[\sigma_{abs}(\lambda_1) - \sigma_{abs}(\lambda_2)]}\right)\right\} \qquad (8.3.10)$$

For Nitrogen dioxide NO_2 the absorption cross-sections are:

$$\sigma_{abs}(447.85\mathrm{n}m) = 6.38 \times 10^{-19} \; Cm^2$$

$$\sigma_{abs}(450.00\,nm) = 3.5 \times 10^{-19} \; Cm^2$$

From equation (8.3.10), Table 8.3.2 we can determine that a Nitrogen dioxide NO_2 concentration of 0.03 ppm extending over a 1 Km range, will result in

$$\frac{I_1}{I_2} = 1.05 \tag{8.1.11}$$

A change in the received intensity which is relatively easily measured. If the range is increased, or concentration, by a factor of 10, then the ratio of the received powers will be increased to approximately 1.6. As can be seen from the above discussion, even relatively low pollution concentrations result in appreciable ratios of received signal at the peak and off the peak absorption wavelengths.

8 System Implementations

8.1 Approach for the Video Measurement Technique

The intent of this measurement technique is to compare two images taken from the same sample-space, the first seen through an on-peak absorption filter ($4500\overset{\circ}{A}$) and the second seen by an off-peak absorption filter ($4478.5\overset{\circ}{A}$) to determine pollution concentrations.

It is necessary to obtain the ratio between two different intensity levels as shown in equation (8.1.10), which are a function of the gas concentration. The arrangement for the video technique is shown in Fig.9.1.1, in this approach the analog video output from the CCD feeds to an A/D converter, then to a frame grabber and finally to the host PC. This computer then processes a flow of scanned frames through the memory, which are generated by the frame grabber, and by issuing a command to the computer, it will then capture one frame at a time.

Each captured frame is saved under a separate file name. The information in each file serves as raw data for future comparative analysis. The image frame file is stored in memory-mapped locations in the ASCII format. An interactive computer program written in Assembly language, which could be totally automated, process the selected sample-space from a given frame.

The program does an internal transformation from the ASCII format to a hexadecimal format, then calculates the number of pixels in each of the intensity levels per the selected sample-space.

For demonstration purposes, a histogram showing pixels distribution is produced at each of the intensity levels.

The the area under the curve of the intensity a function of each of the two wavelengths or statistical centroids serves as a weighting function for the intensity differential value. This corresponds to peak and off-peak absorption of the gaseous pollutant which according to equation (4.3.10) represents the concentration measurement.

Repeating the previous process for each of the frames, further comparisons are made between the subtracted images of filtered and unfiltered sample space, as well as between two filtered selected sample-space of the same frame.

8.2 System Components

The basic components of the image processing system used in the experimental setup shown in Fig.9.2.1 consists of three basic structures, image acquisition, image processing and image display. I will describe the equipment used and my reasons for choosing this specific equipment, some of which I designed and built specifically for use in these experiments.

Image Acquisition.

At the early stage of the work, part of the experiment performed using a Vidicon-type camera, the Panasonic model WV-1550. This camera is considered to be one of the best low light level cameras on the market, covering the visible range with a horizontal resolution of (650 lines), and a signal to noise ratio (S/N) of 44dB at AGC OFF. The camera has automatic and manual light control, which was used to turn the automatic gain control OFF to avoid internal light compensation, which had been a source of measurement error. In performing the experiment, the camera was set up as an acquisition device.

Some interesting observations occurred during the experiment. The output of the standard video signal was measured, one field at the time, using 447.85 nm and 450.00 nm filters, and was discovered to be nonlinear instead of linear. The comparison of the output was first done using a single camera, and was more linear towards the center, especially at the edge of the video field. This fact raises a doubt about the sensitivity of the device in detecting the proper ratio.

A possible explanation for this occurrence is that some nonlinear, so-called "subunity gamma" tubes do not have a unique sensitivity for all illuminations, gamma being the slope of a log-log plot of light transfer characteristics. Gamma tubes are dependent on the sensitivity of spectral-energy distribution of the illumination falling on the storage target elements of the camera tube. Another problem is encountered when using a He-Ne laser to probe the gas cell. The lag or incomplete erasure of the storage target, which depends on the charge transport characteristics, changes the capacitance of the target and the electron-velocity distribution of the scanning beam. Because of these problems with the vidicon tube, another linear video detector was used. The choice was the totally linear CCD device.

CCDs are becoming popular for a variety of reasons. The linear radiometric response of CCDs, and their sensitivity to minute changes in light intensity, can be seen in the following experiments. It is possible to perform accurate radiometry with these devices, and the systems are so precise that is not uncommon to digitize individual pixel intensity values to 12 bits precision. CCD spectral response is broader than vidicon or even newvicon tubes or film systems. Another important factor is the fixed position of each potential well, which provides high geometric precision of sampled imagery. The devices are small, lightweight and require no mechanical parts or scanning electron beams. The high reliability of CCDs gives them a superiority over other solid-state electronic devices, and made them an excellent choice.

Based on the aforementioned reasons, an image-sensing device made by the Electro-Physics Corp., the IR Microcam model CCD1200, was chosen. The IR Microcam is an ultra-miniature infrared viewing CCTV camera, based on a charge-coupled device (CCD) image sensor, that features high sensitivity and signal-to-noise ratio extending to the 1100nm. The Microcam also features precise image geometry, low lag, high resistance to image burn-in, and a miniaturized design. The camera is useful in applications involving detection and alignment procedure. It can also be used for monitoring of radiation, darkroom processes, surveillance in a darkened environment in conjunction with infrared spotlights and illuminators, and imaging of objects at temperatures above $600^{\circ}C$. The following specifications are determined by the manufacturer:

Spectral response: Visible to 1100 nm
Picture elements: 384 (H) by 491 (V)
Horizontal resolution: 280 TV lines
Scanning system: 2 : 1 interlace, 525 lines/60Hz
Minimum illumination: 3 lx (0.3 fc)
S/N ratio: 46 dB
Video output: 1.0 Vpp at 75 ohms
Temperature range: $0^{\circ} to 40^{\circ}C$
Power requirements: 12V DC or 120 V/60Hz, ~2.9W
Connectors: Video output BNC, 12 pin for 12V Dimensions (WHD): 1.7" x 1.2" x 5.1"
weight:0.56 lb

Typical spectral response characteristics are shown in Fig.9.2.2

The second part in the image acquisition system is the analog to digital converter and frame grabber which were built in the laboratory. Shown in Fig.9.2.3 is the block diagram of the A/D converter, while the interface circuit to the frame grabber and to the IBM computer, is shown in Fig.9.2.4. The software program which was used to accomplish various tasks in the measurements (event, period, pulse width, and frequency counting, graphics, calibration, linearization, I/O driver), is listed in appendix A. The A/D converter used in the experiments, Model DASH-8, manufactured by the Merta Byte Corp, has the following features:

8 A/D channels with 12 bit resolution
4000 Samples/Sec.
Hardware supports 30,000 Samples/Sec. in Assembly Language
Programmable Scan Rate
Foreground/Background Operation
7 Bits of Digital I/O (4 Outputs, 3 Inputs)
Interrupt Handling
Precision 10 Volt Reference Output
+/- 12 and +5 Volt Power from IBM PC/XT
Output Frequency from 37 Hz to 1 MHz

The flash converter were used to digitize the NTSC video signal from the CCD camera with input connected to the parallel printer port of the IBM/XT with 46K of on-board RAM. The resolution of the captured pictures was: 320 x 400 with 16 gray level.

Image processing:

The software used to capture the image is a product of Perfect Vision. It can capture a black and white image in 1/60 of a second, and with the interlaced output of the CCD captures an image every 1/30 of a second. The digitized picture refreshes itself automatically on-screen every 5 seconds. With the help of the menu-driven program, the screen image can be captured and saved ether on a floppy or hard disk, and can be processed using a program written in Assembly language, creating a gray-scale Histogram. The frame can be loaded in from the disk as a frame file in the form of raw data, to perform the division of two pictures, to find the corresponding intensity ratios of each pixel, or to demonstrate the difference in light intensity levels in a specific location in the frame. Calculations may be made down to the level of 4 pixels, which is the limit stipulated by the Hercules card, with a resolution of a 720 x 348 4(gray). In addition, several other operations may be performed by analyzing the file material statistically.

Image display:

To provide an output product that can be seen by the observer. The display of the output signal was sent to computer video monitor supported by a Hercules card to display the digital image at the same time the analog output of the CCD camera was sent to a Video RGB monitor model PVM-1270Q made by SONY corp. Its a color monitor support NTSC system with RGB inputs capable of accepting both digital and analog signals with a high resolution-500 lines with video input and 600 lines with RGB inputs. The RGB inputs was useful in super imposing the output of two cameras simultaneously each connected to different gun of the monitor. It also have a video/sync loop-through, capability is useful for multiple connections.

Optical components:

Two broad band filters one is centered at $4478.5A^{\circ}$ and the other is centered at $4500A^{\circ}$ Fig.9.2.5, and Fig.9.2.6 shows the transmission characteristic of each.

One air-spaced Glan-Taylor beam splitter

8.3 Experimental Setup to Demonstrate Feasibility

The setup of the experiment shown in Fig.9.3.1, was created to simulate the conditions in which NO_2 gas is normally monitored. A sampling chamber of 40 Cm was chosen, with an inlet and an outlet as shown. A flow control valve with two supply lines was attached to the inlet, one for filtered air and one for NO_2, the outlet was connected to an exhaust system.

At one end of the sampling chamber, a simulated ambient light was projected onto the background target, which then reflected the light through the sampling chamber and into the CCD cameras. At the other end of the chamber, with a total optical path of 100 Cm., the CCD1 video camera was positioned opposite gas filter ($4500 \mathring{A}$). Halfway between the sampling chamber and the CCD1, a beam splitter was used to project the same image into the CCD2 opposite the second filter ($4478.5 \mathring{A}$) with the same optical path length of CCD1. (A single camera with rotating filters for ON and OFF-peak and trough absorptions would suffice.)

The output of the video cameras is fed to the analog / digital converter, then to the frame grabber (which I designed and assembled, in the laboratory) and finally to the host PC. At the same time, the video cameras outputs in its analog form is displayed on an RGB monitor. This enables the superimposition of two different camera's output signals in two of the three basic colors at the same time on the same monitor screen.

Given commands through a pull down menu, the computer capture one frame at a time from a flow of scanned pictures generated by the frame grabber, which displays a new image frame every five seconds. Each captured frame is saved as a separate file and downloaded to a graphic printer after performing the previously explained analysis.

Two images are then compared irrelevant of the background target. The entire measurement process is repeated in three consecutive experiments, using three kinds of background target. The first background target is over saturated white; the second, undersaturated white (or oversaturated black); and the third, an equal combination of black and white. It is my intention to prove that the change in intensity of the measurement is independent from the effects of a target background which is believed to be related to the process of light absorption by the gas. The experiment was repeated using different concentration levels of NO_2, after flushing the previous experiment's gas from the sampling chamber.

Prior to the previous experiments, a precaution was taken in measuring the linearity of the detecting device. A variable density filter as shown in Fig.9.3.2 was placed opposite the CCD and recorded intensity versus wavelength measurements using the oscilloscope to measure the output voltage of the composite standard video signal.

Another experiment was conducted to check the signal-to-noise ratio at the ground level (no signal, or totally blank) and a uniform white light. Based on that measurement a null adjustment was performed to set the dc bias to the electronic circuitry.

8.4 Experimental Results and Conclusions

The following set of results are taken from a sample-space of 100x100 pixels over 16 gray levels. The corresponding measurements which demonstrate the ratio between two different intensities for each of the two filters were calculated by the computer program as follow:

Case (1) Target pattern #1 LTESd (Figures 9.4.1,2,3,4,5,6,7 & 8).

$I_1 = 5.31$
$I_2 = 4.61$

$I_1/I_2 = 1.15$

Case (2) Target pattern #2 RTESd (Fig. 9.4.9).

$I_1 = 8.90$
$I_2 = 7.73$

$I_1/I_2 = 1.15$

Case (3) Target pattern #3 MTESd (Fig. 9.4.10)

$I_1 = 7.89$

$I_2 = 6.68$

$I_1/I_2 = 1.15$

The previous set of measurements in the three cases mentioned above corresponds to a No_2 concentration of 180ppm which is measured after calibrating the CCD reading with and without the presence of gas. Pressure inside the gas cell was kept equal to atmospheric pressure by adjusting the outlet control valve of the gas cell, in order to secure an identical flow of output and input.

Three files of raw data (ZZ4.raw,ZZ0.raw & ZZ045.raw) were captured using the frame grabber representing one complete set of data using pair of filters (4478.5A & 4500A) shown with their three-dimensional representation and the corresponding topographical contour mapping beside their ratios Figures 9.4.10a,10a1,10b,10b1,10c & 10c1.

The next set of results (Figures 9.4.11,12,13,14,15,16,17,18 & 19). shows a three-dimensional representation of the intensity of each pixel, scaled to show its ratio to a sample space inside the gas cell. Several sets of measurements were obtained using different levels of concentration. These include both high and low level concentration measurements. Blanking techniques were used to eliminate the rest of the uncounted-for ratios. Contour maps of the intensity grid are provided to show the distribution of specific ratios within the x-y plane. In addition, three color photographs Figures.9.4.20,21 & 22 are provided of three-dimensional graphs, depicting intensity levels in the Z direction generated via the computer program, as displayed on the computer's color monitor in their actual data form.

Finally, three sets of digitized images showing the actual results of the simulation experiment are included. In these images (Figures.9.4.33,34,35,36,37 & 38), a separate color was assigned to the specific ratio, using 4478.5A and 4500A filters. In each set, which is comprised of three images, there is an image taken with each of the two filters. The third image is a ratio of on-peak and off-peak absorption of No_2.

Another group of images shows an alignment plate of the sixteen color registers Figures 9.4.23,24,25,26,27,28,29,30,31 & 32. A combination of red, green and blue, integrated with a gray level scale, demonstrates the shifts of the different ratios in relation to various levels of No_2 concentration Figures 9.4.42 & 43

.

Calibration plates Figures 9.4.25 & 29 were first created using the sampling chamber without the presence of gas, then using a No_2 concentration of 180ppm under atmospheric pressure. A default setup for the color registers was recorded as a basis for later judgements of the varying concentrations Figures.9.4.44 & 45.

The image of two scaled ratios was superimposed over an image of the original calibration plate Fig.9.4.29. Subsequently, the blanking technique was used to show the ratios alone, retaining the edge details of the sampling chamber Fig.9.4.30.

A similar set of images utilizing different concentration levels of No_2 was taken, with the sampling chamber filling the field of view (Fov) of the CCD camera Figures 9.4.39, 40, & 41.

The final image, Figure 9.4.47 illustrates an accidental leak of No_2, which was taken during the process of capturing an image of the sampling chamber without a target background, as shown in Figure 9.4.46. The outlet tube was accidentally removed from the back of the sampling chamber, causing an escape of No_2 into the surrounding atmosphere, and which was only discovered after processing the image taken during the experiment. This "accident" serves as a culminating proof of the ability of the remote image sensing technique using a specific topographical layout in the detection of gases and other pollutants in the atmosphere.

$\lambda(\mu m)$	$a_R(Km^{-1})$		$a_M(Km^{-1})$	
		V = 1Km	V = 5Km	V = 10Km
0.20	0.708	7.00	2.20	1.400
0.30	0.140	5.60	1.40	0.840
0.40	0.440	4.70	1.10	0.580
0.45	0.027	4.40	1.01	0.496
0.50	0.018	4.134	0.86	0.441
0.60	0.0083	3.70	0.72	0.350
0.80	0.0026	3.10	0.54	0.240

Table 8.3.1 Rayleigh and Mie absorption coefficient [under atmospheric pressure (Inaba, 1976, Table 5.2)]

Process		Differential cross section cm^2
Elastic Scattering	Rayleigh Scattering	10^{27}
	Mie Scattering	$10^{21} - 10^{-24}$
Inelastic Scattering	Raman	10^{-30}
	Resonance Raman	10^{-26}
	Fluorescence (lifetime 10^{-6}-10^{-8})	10^{-14}- 10^{-17}
	Absorption	10^{-14}- 10^{-17}

Table 8.3.2 Typical Cross Section values for Scattering process (Inaba, 1976, Table 3.4)

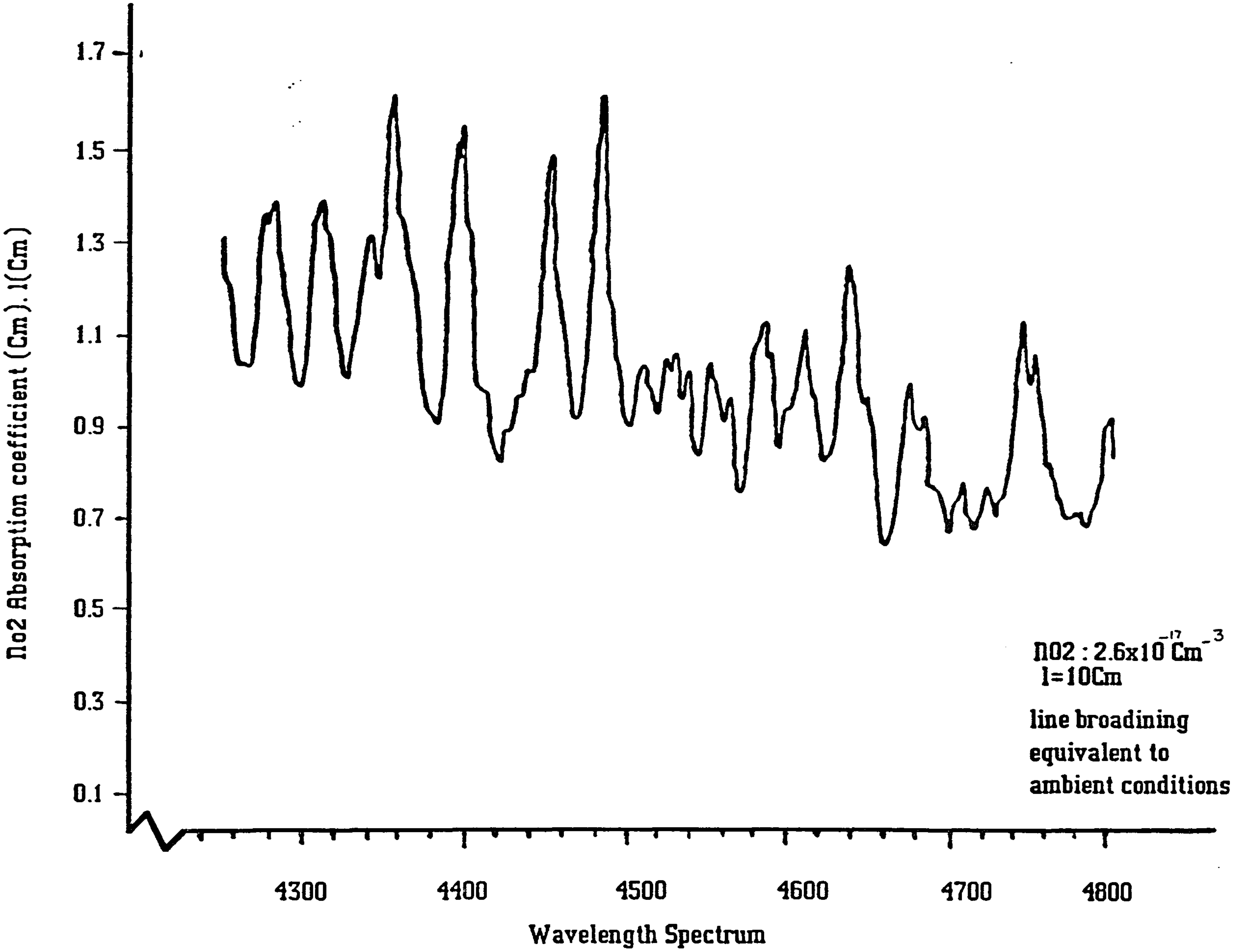

Fig.3.2.1 Πo2 Absorption Spectrum

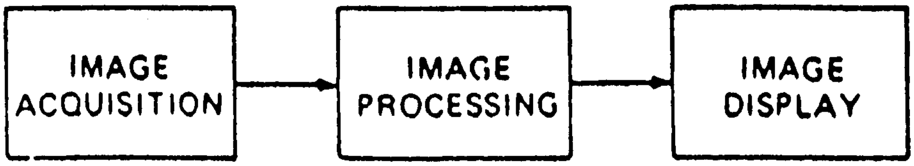

Fig.5.4.1.1 The Three basic components of an image processing system

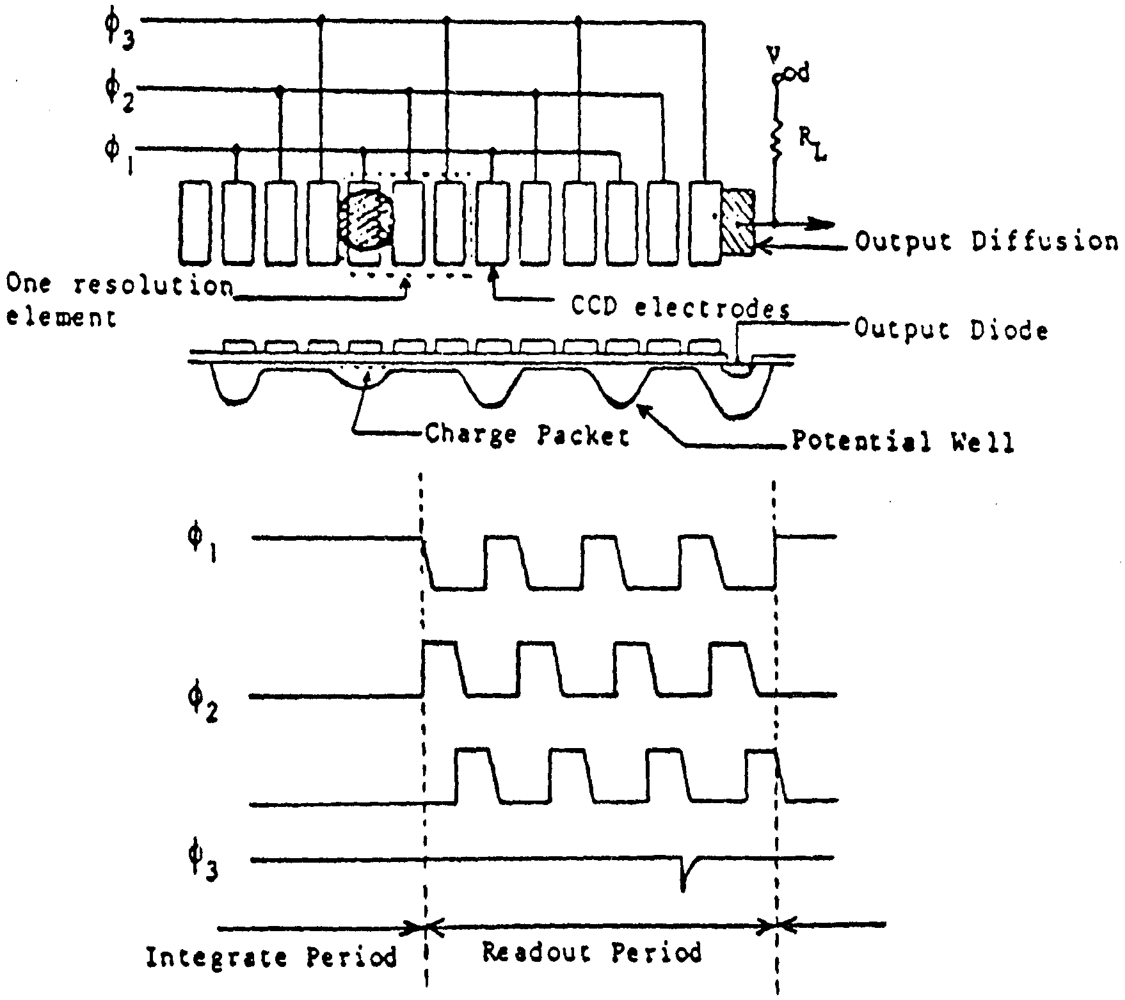

Fig.5.6.2.2 CCD Read Out Mechanism

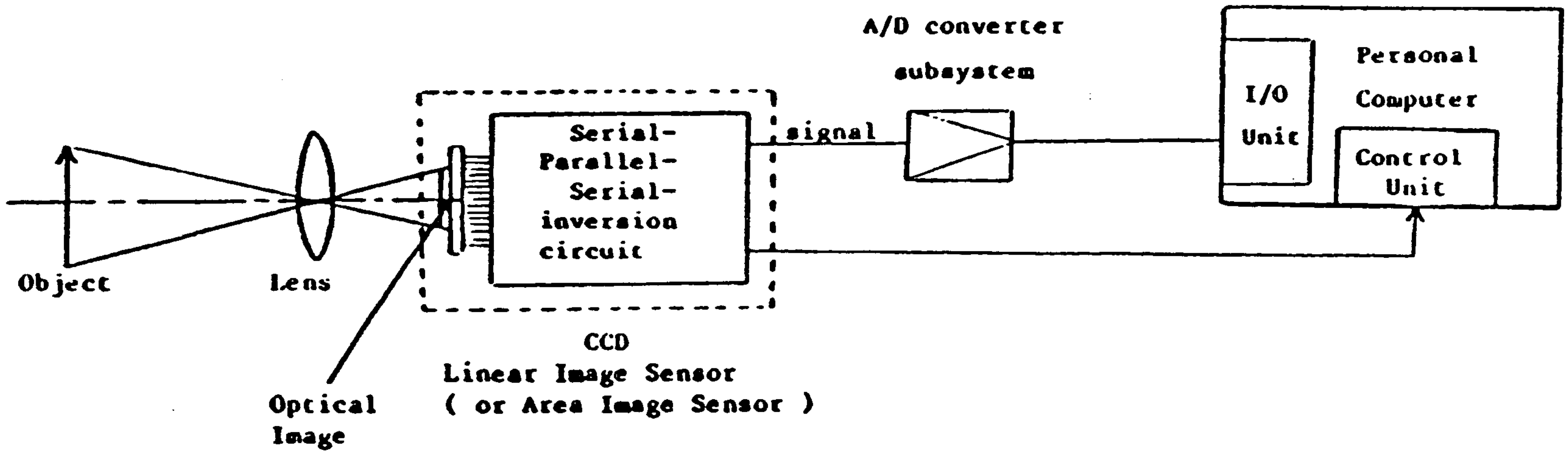

Fig.5.6.2.3 Block diagram of the A/D converter and PC interface

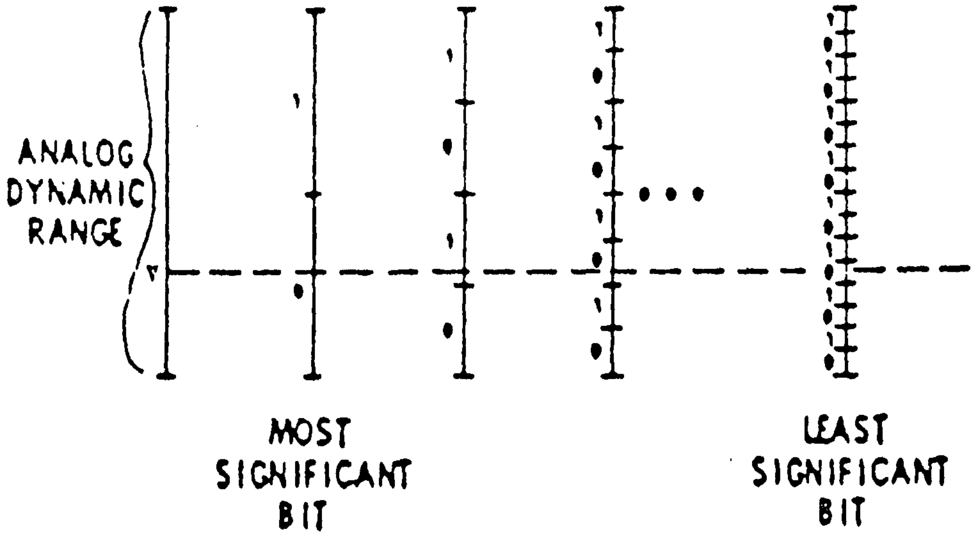

Fig.6.1 The Principle of Digitizing analog signal

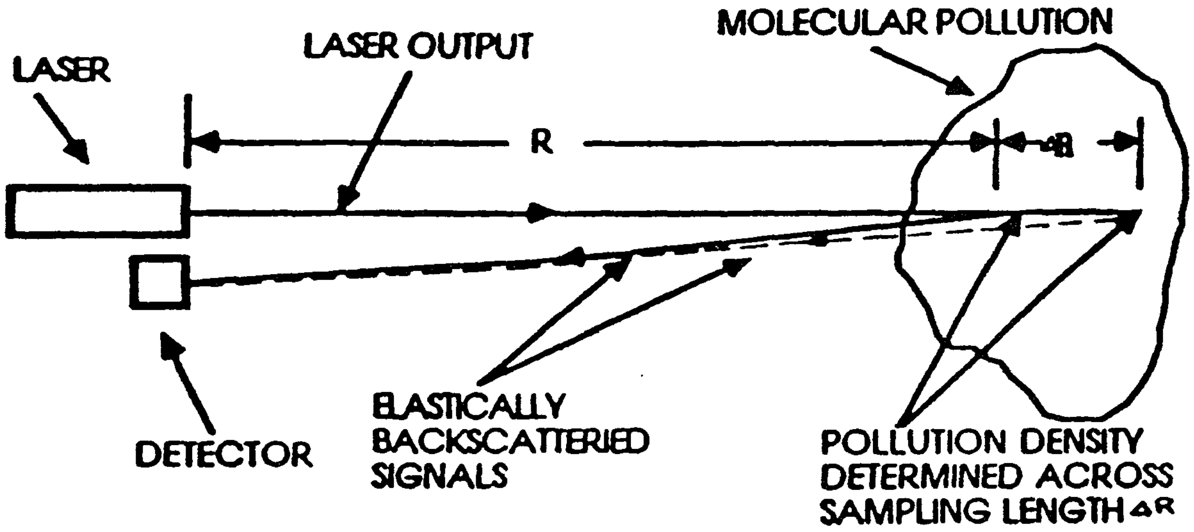

Fig.7.1 **THE DASE SCHEME**

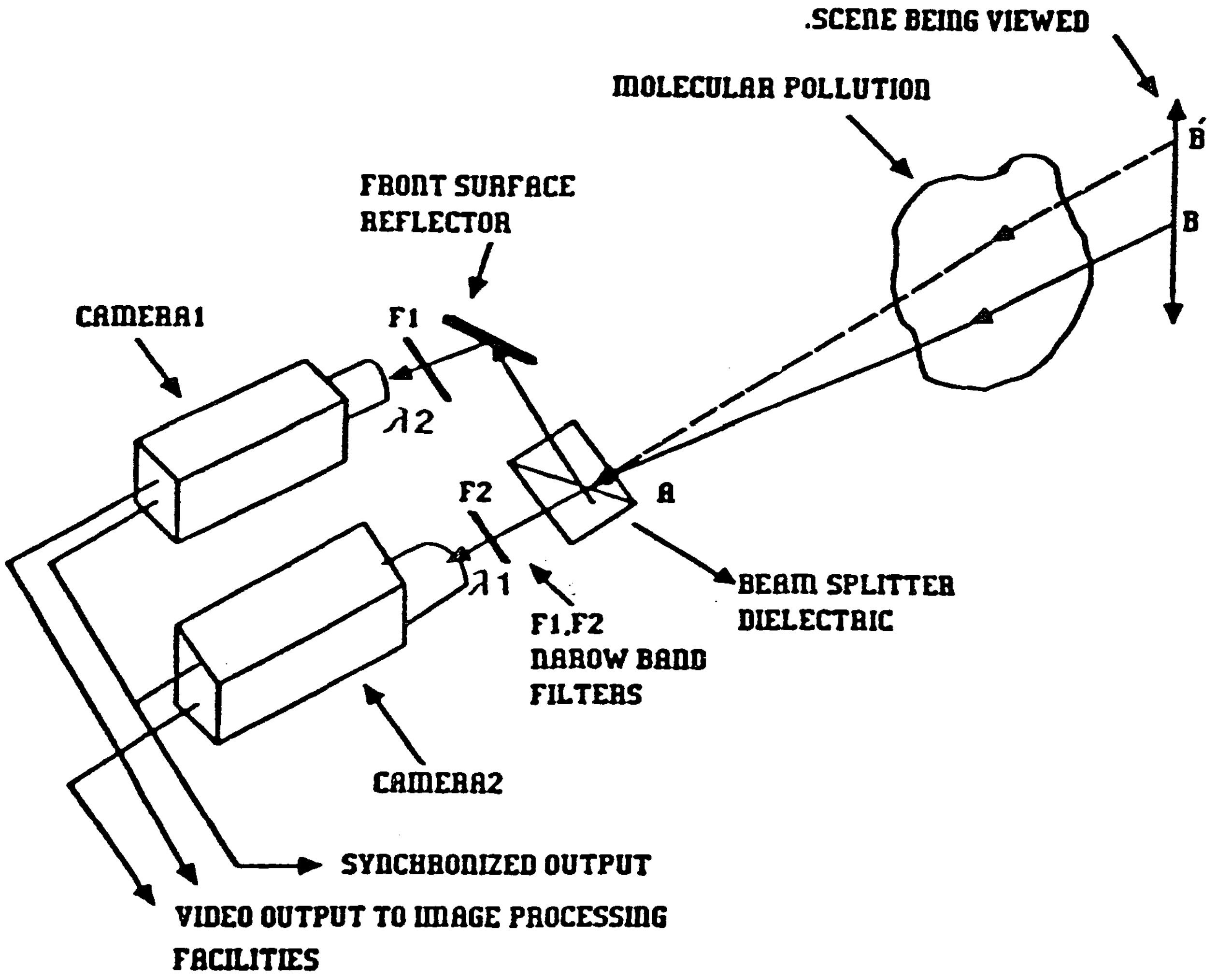

Fig.8.1 VIDEO POLLUTION MONTORING
(SIMULTANEOUS MODE)

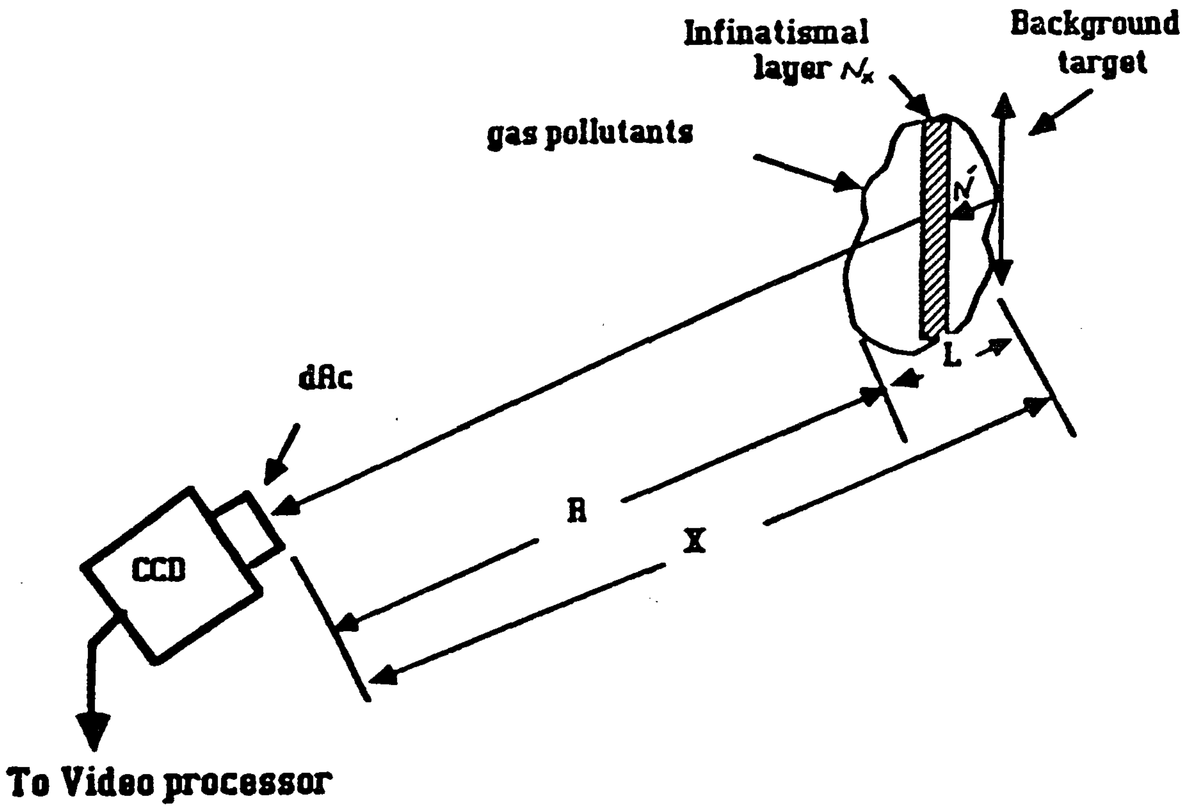

Fig.9.1.1 Detection Limitation of the System

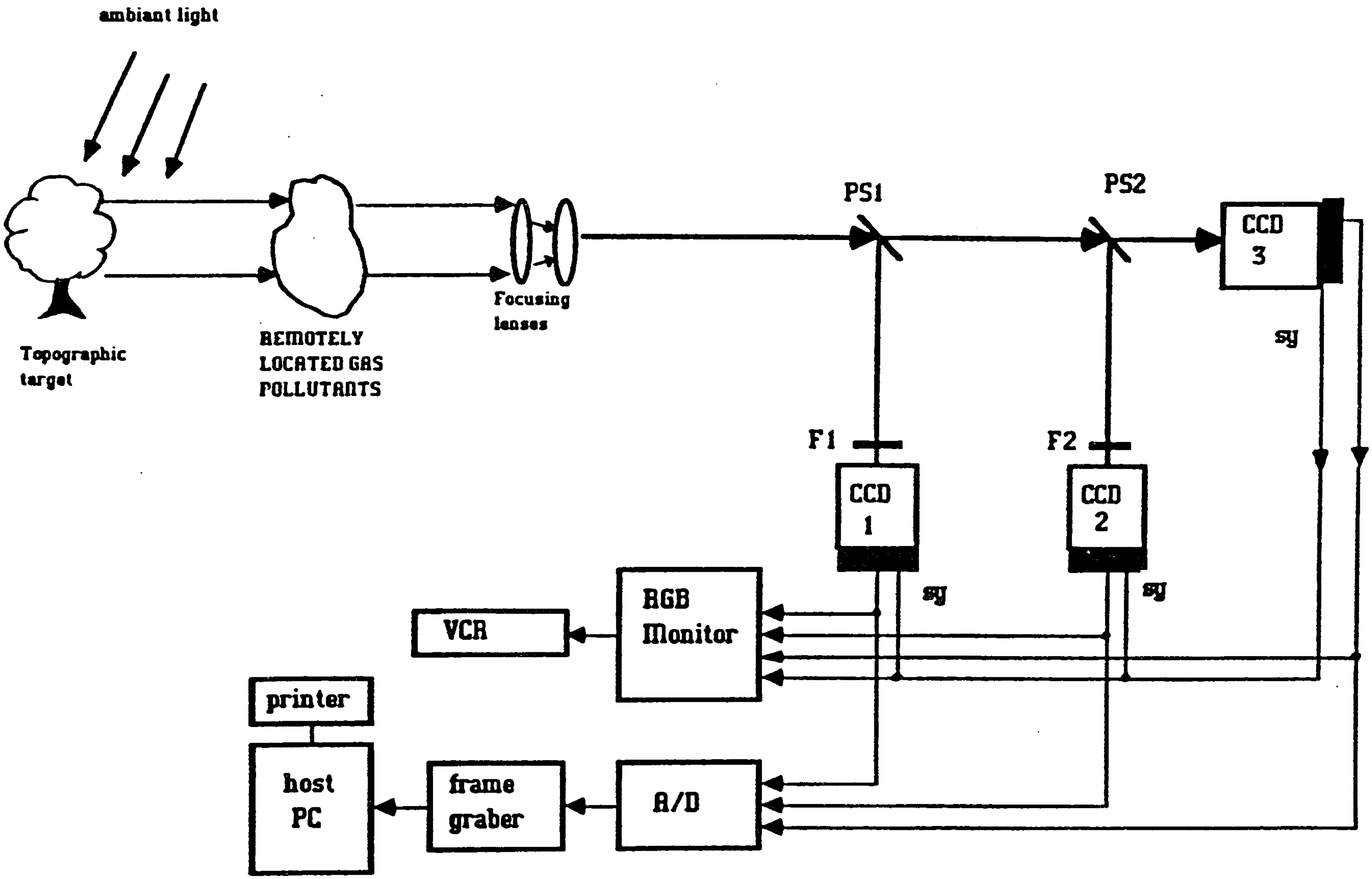

Fig.9.1.2 System Arrangement for the video technique

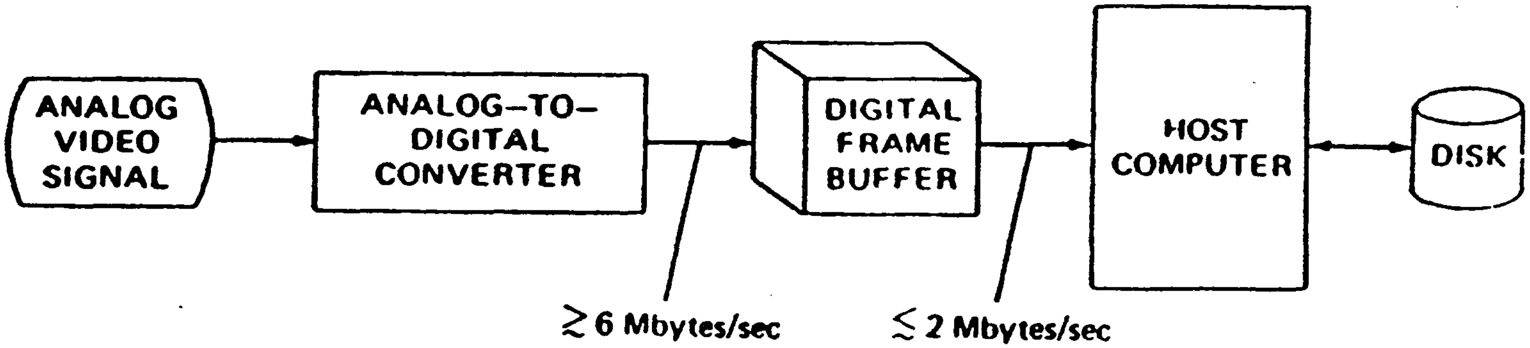

Fig.9.2.1 The rate buffering during video frame digitizing

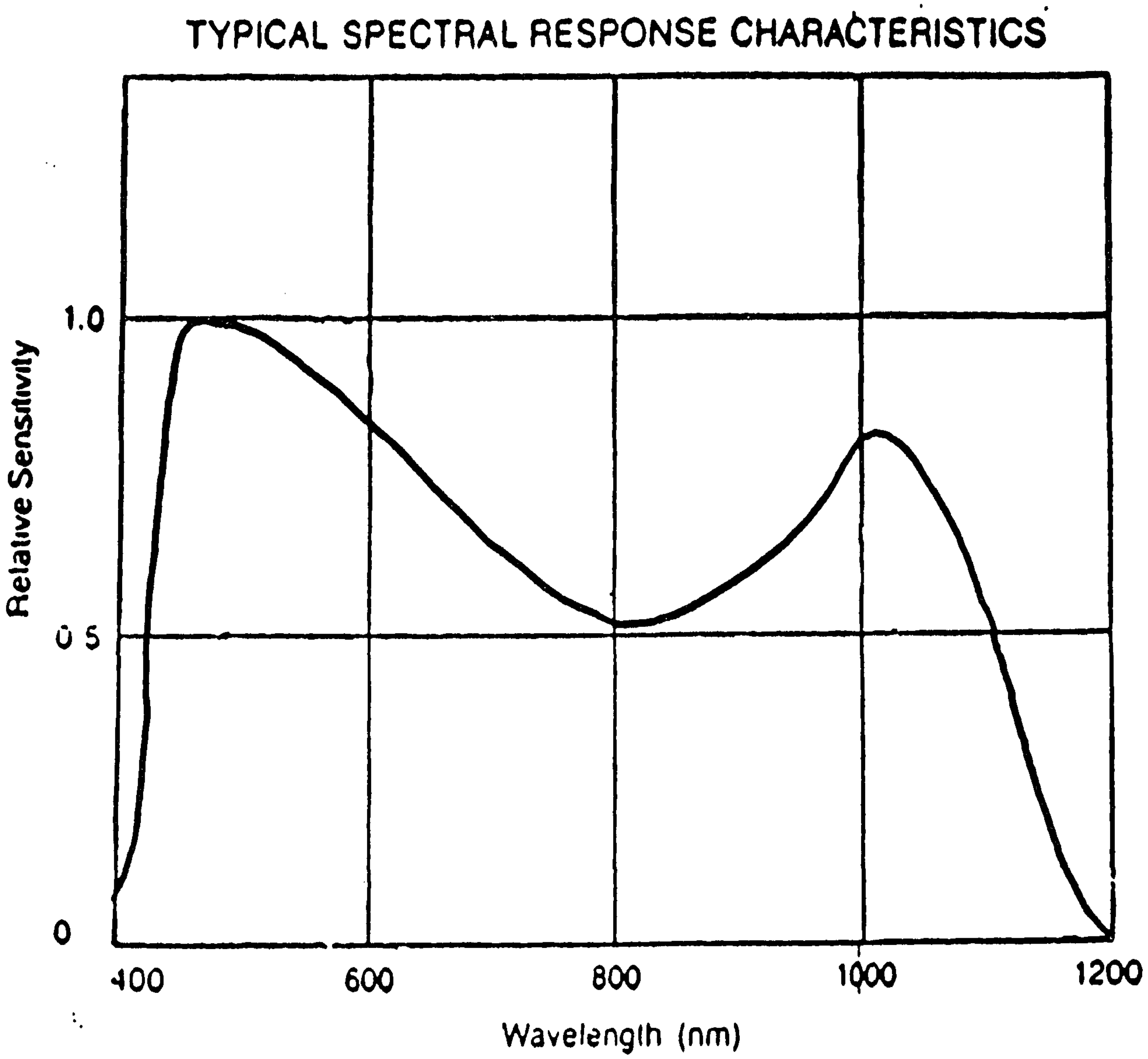

Fig.9.2.2 Typical spectral response charactristics for IR Microcam model CCD1200

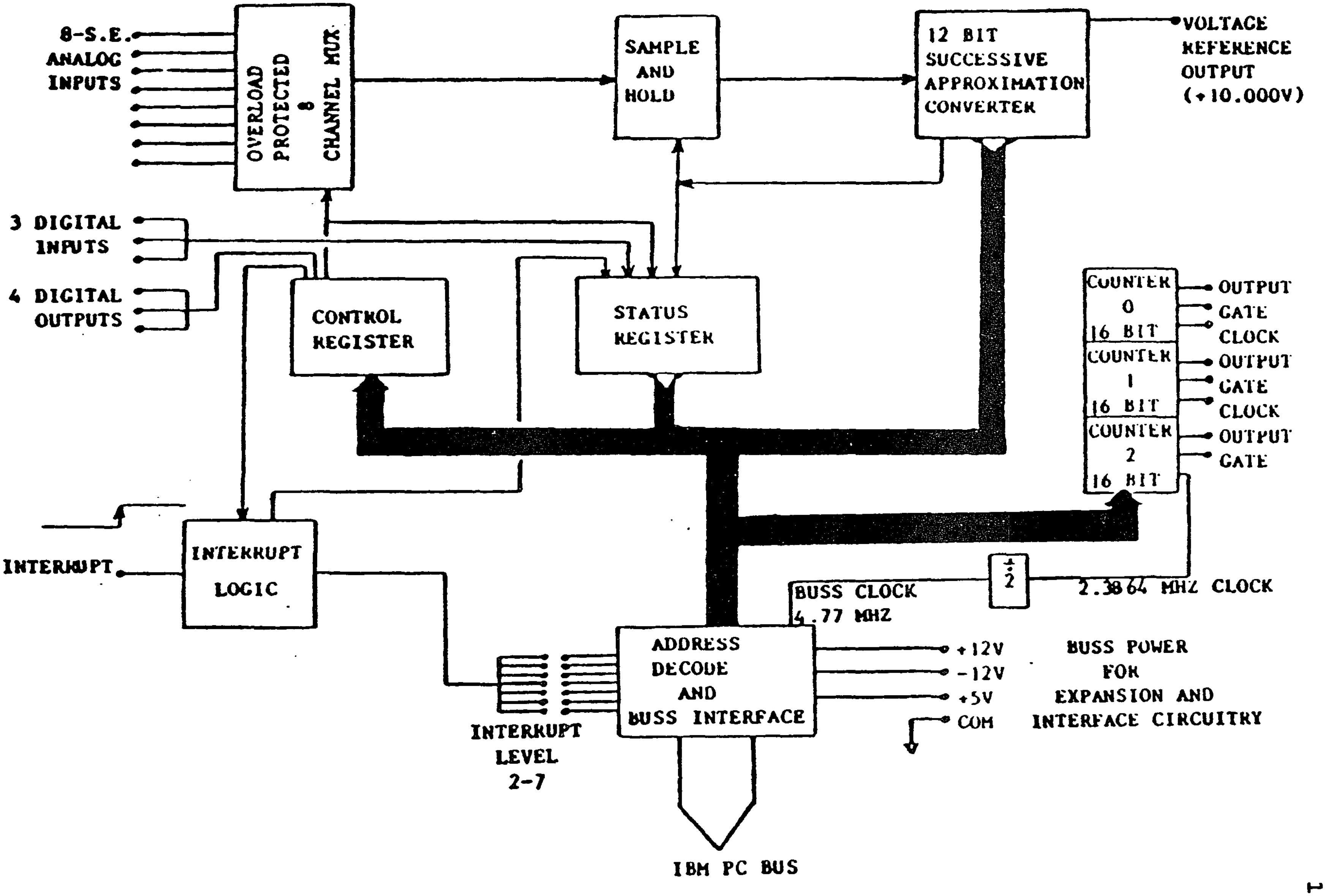

Fig.9.2.3 Block diagram of the A/D converter Bus controller interface

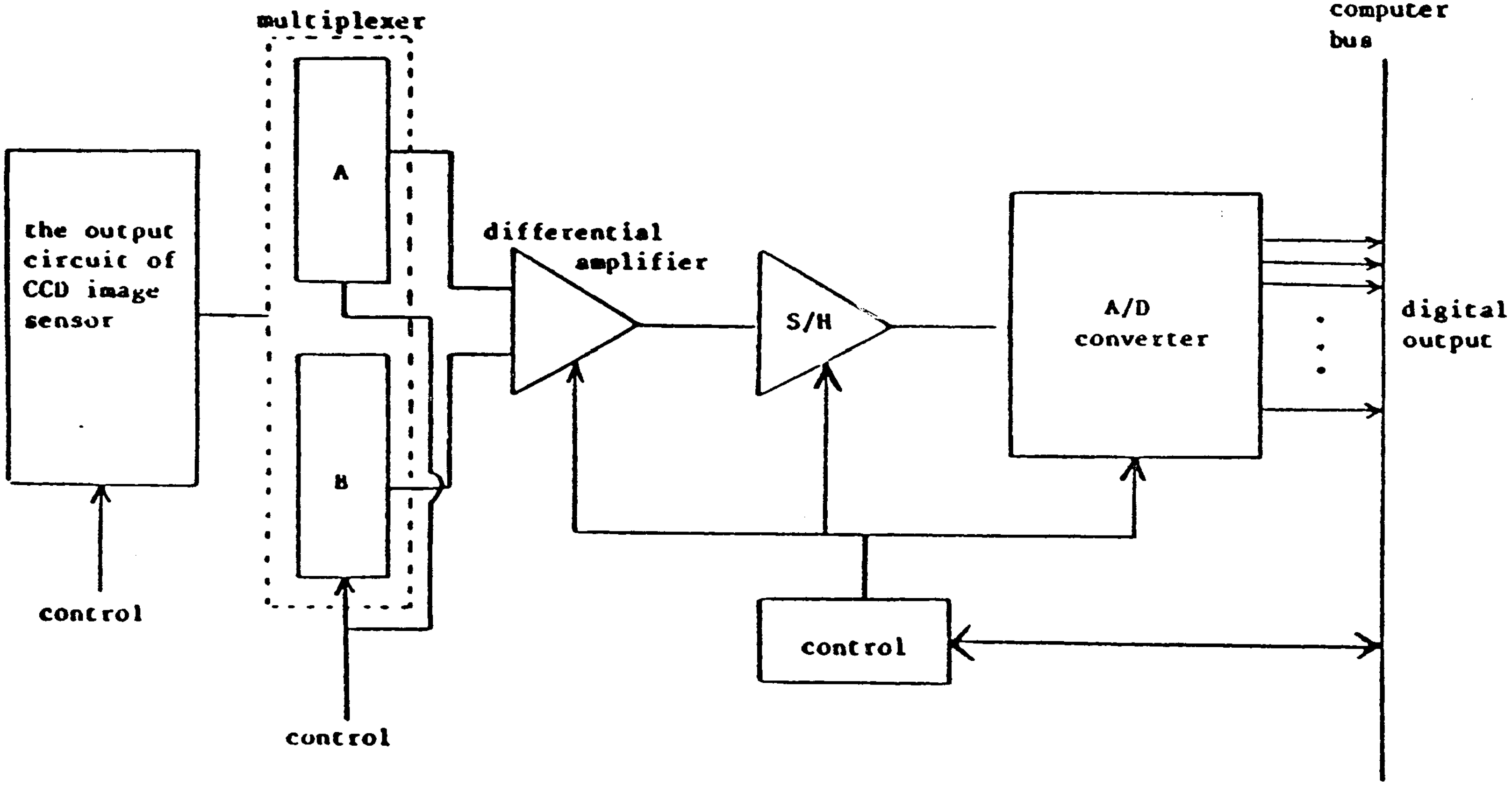

Fig.9.2.4 · Block diagram of the A/D converter and its subsystem with differential inputs and programable gain

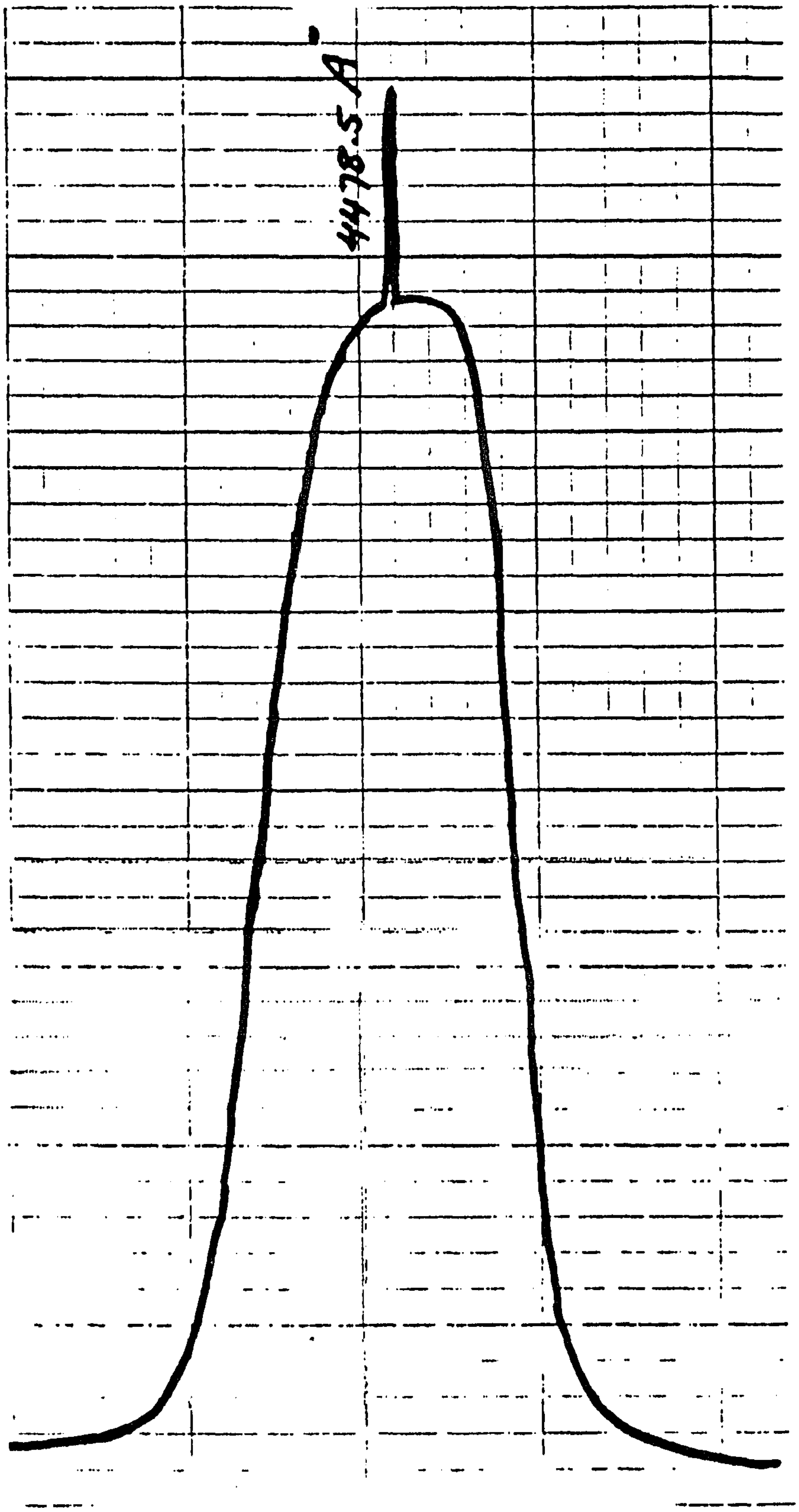

Fig.9.2.5 Transmission charactristics for the broad band Filtar centered at 4478.5Å

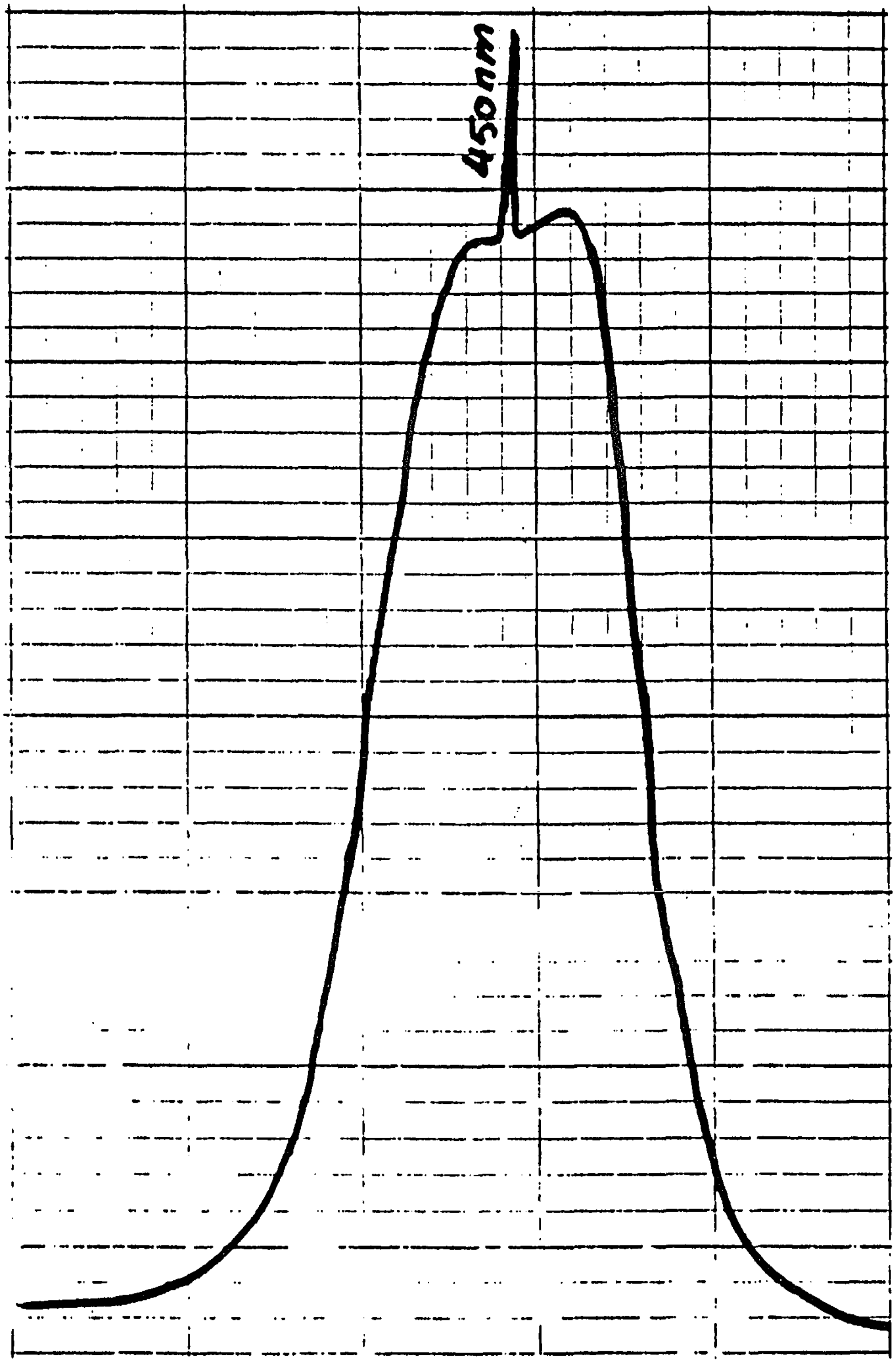

Fig.9.2.6 Transmission charactristics for the broad band Filtar centered at 4500Å

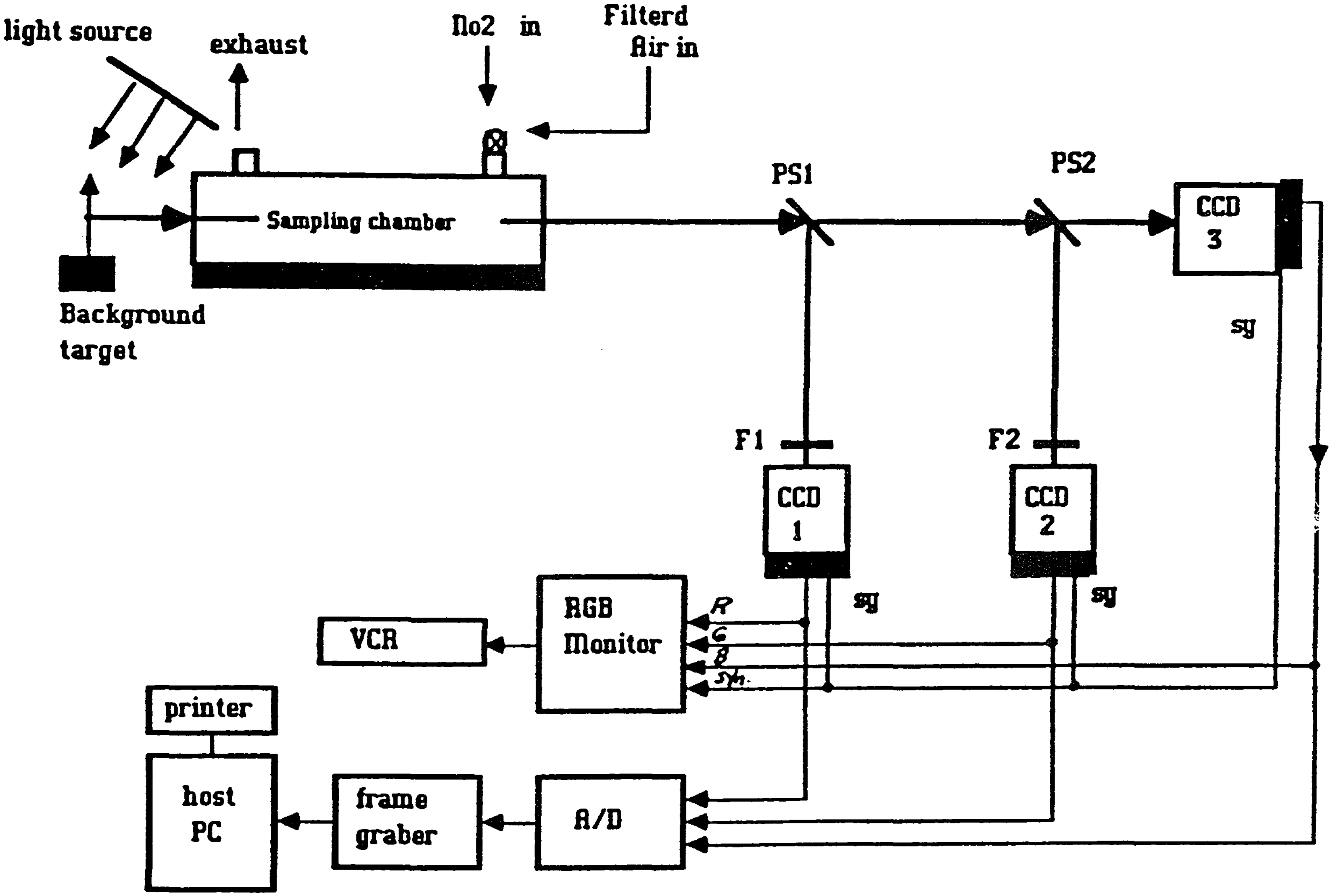

Fig.9.3.1 experimental setup #1

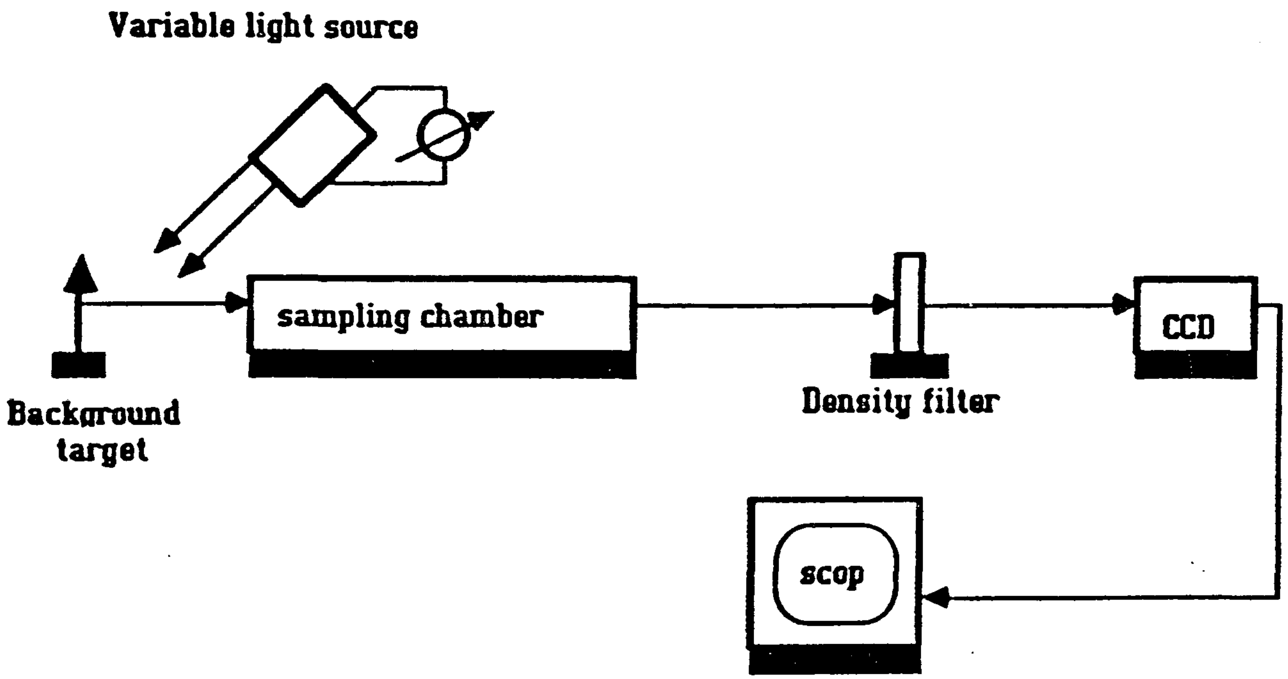

Fig.9.3.2 Experimental setup to examin linearity

of the CCD camera

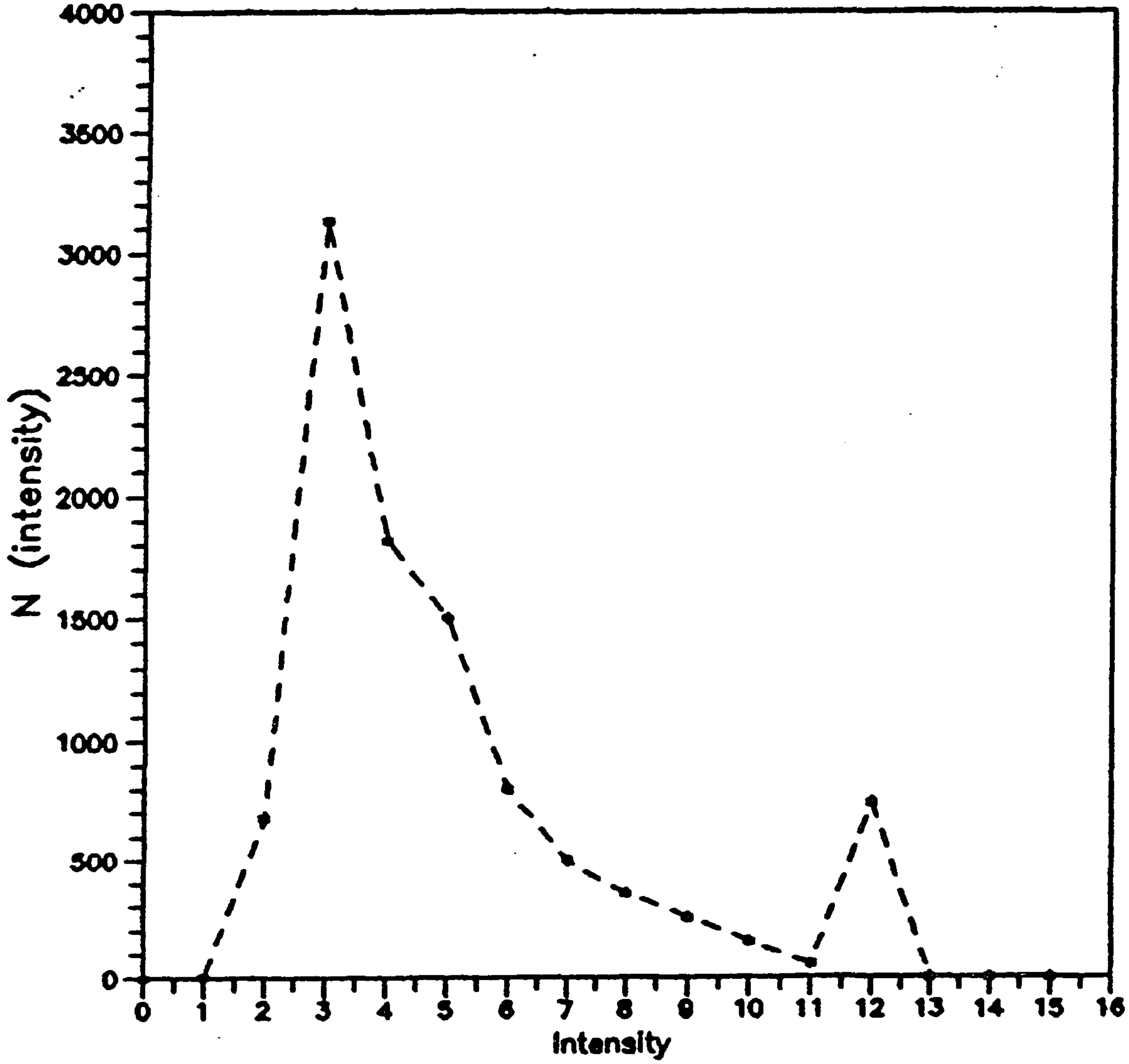

Fig.9.4.1 Case(1) Target pattern #1
NO_2 present LTES1
No filter present

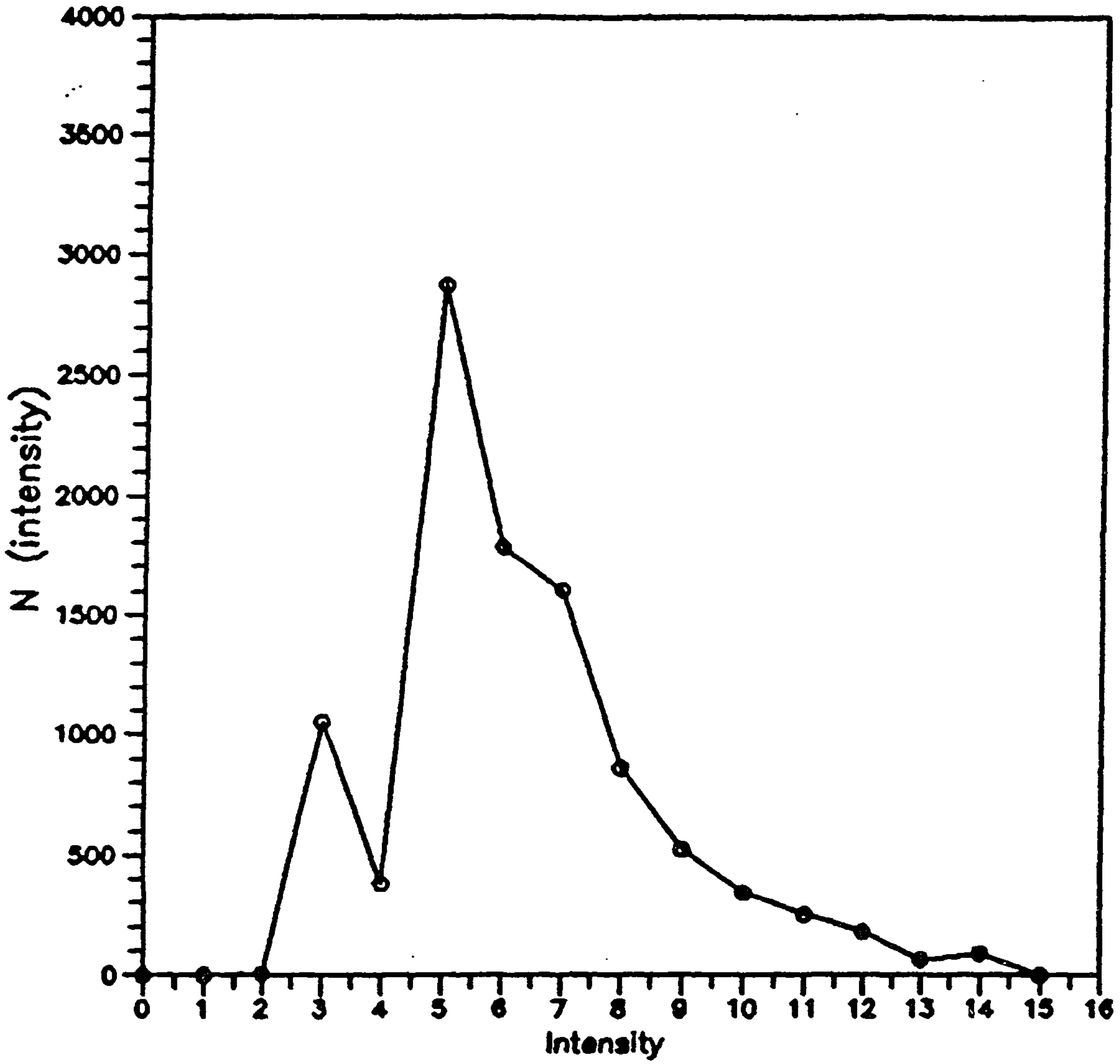

Fig.9.4.2 Case(1) Target pattern #1
NO$_2$ present LTES2
Using filter (4500 A)

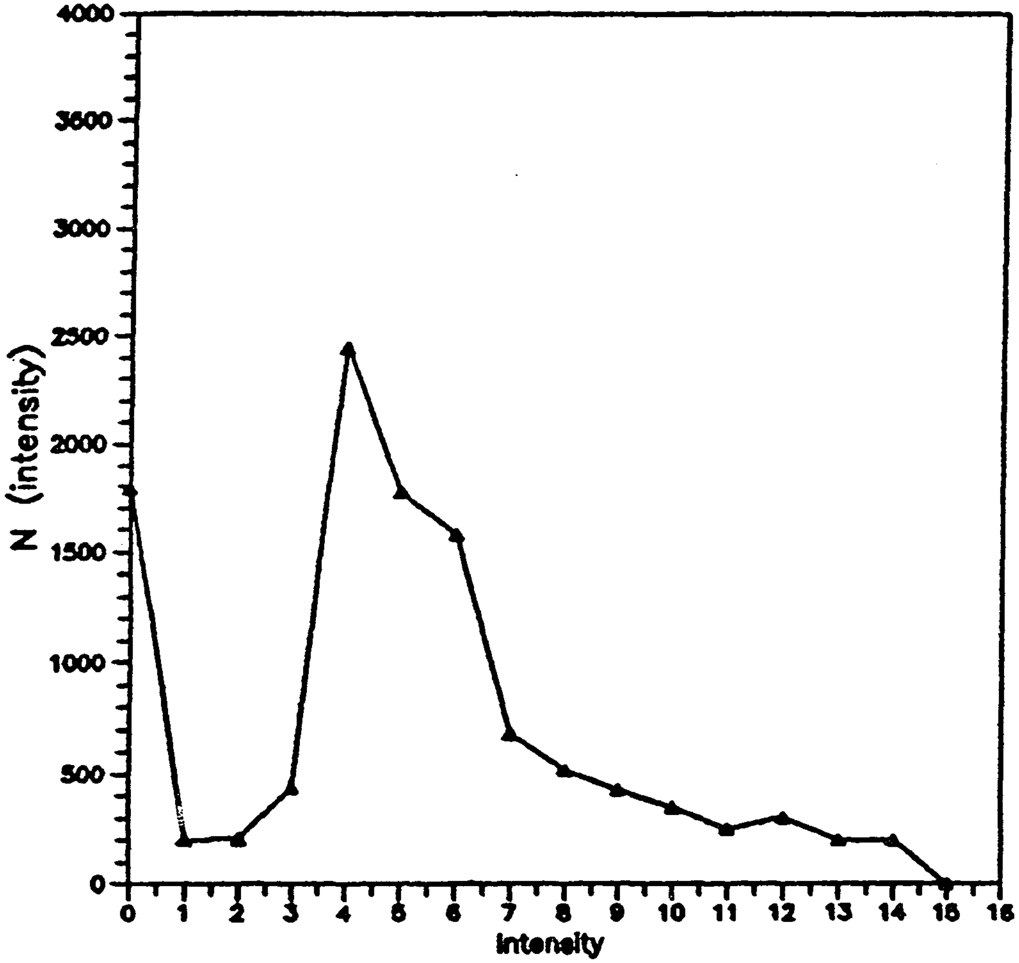

Fig.9.4.3 Case(1) Target pattern #1
NO$_2$ present LTES3
Using filter (4478.5 A)

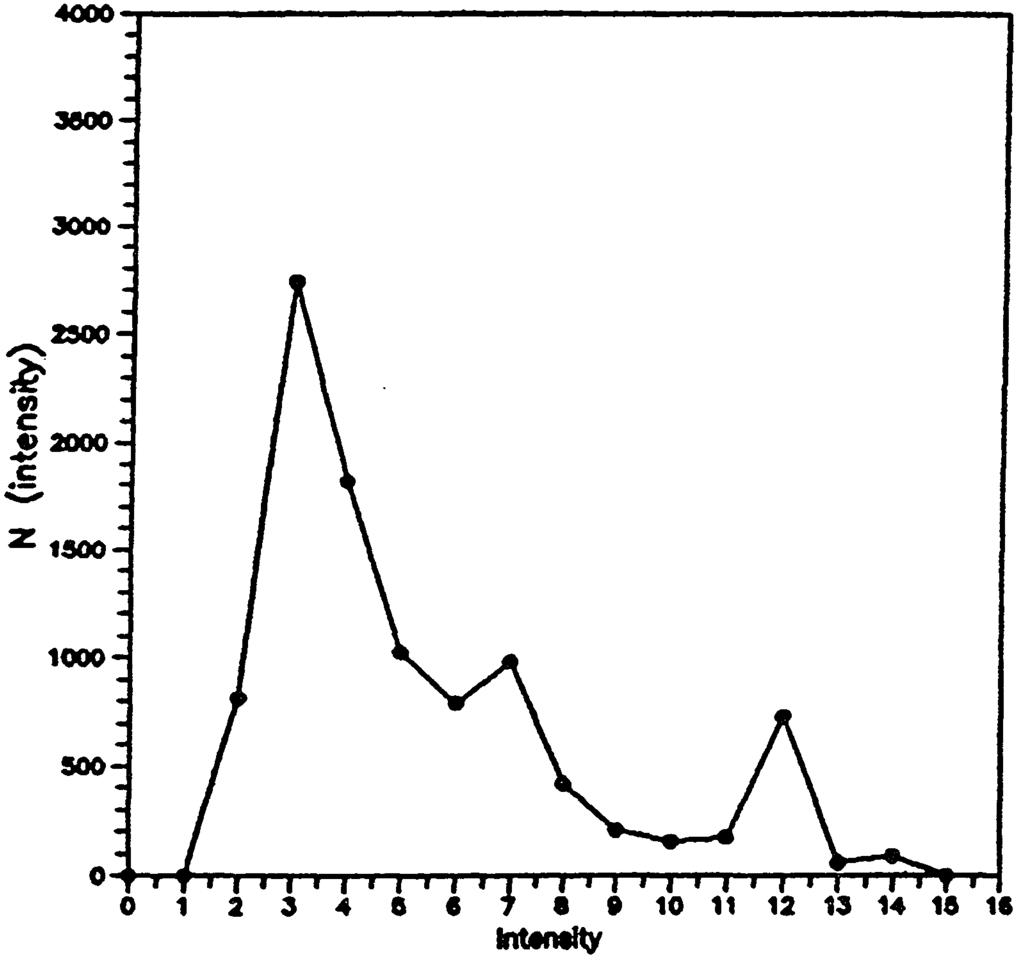

Fig.9.4.4 Case(1) Target pattern #1 LTES12d
The difference between sampled area
with and without the filter (4500 A)

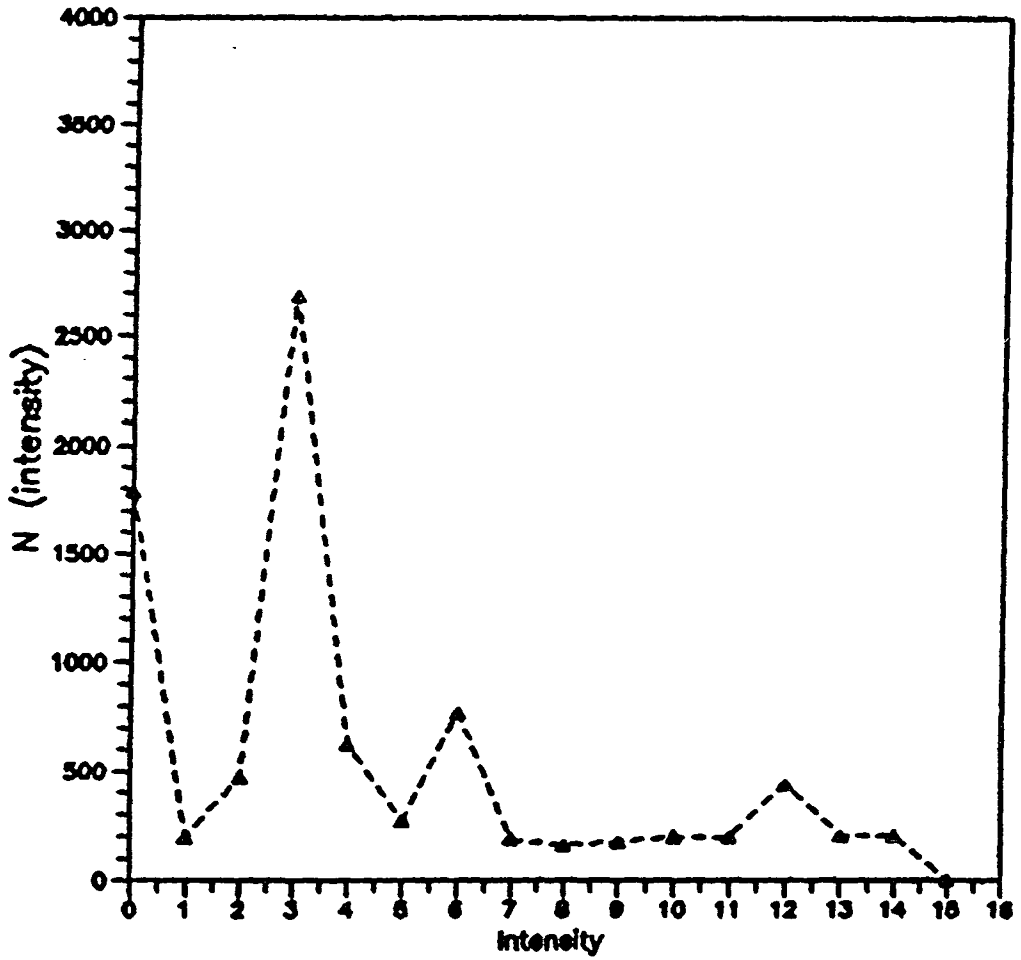

Fig.9.4.5 Case(1) Target pattern #1 LTES13d
The difference between sampled area
with and without the filter (4478.5 A)

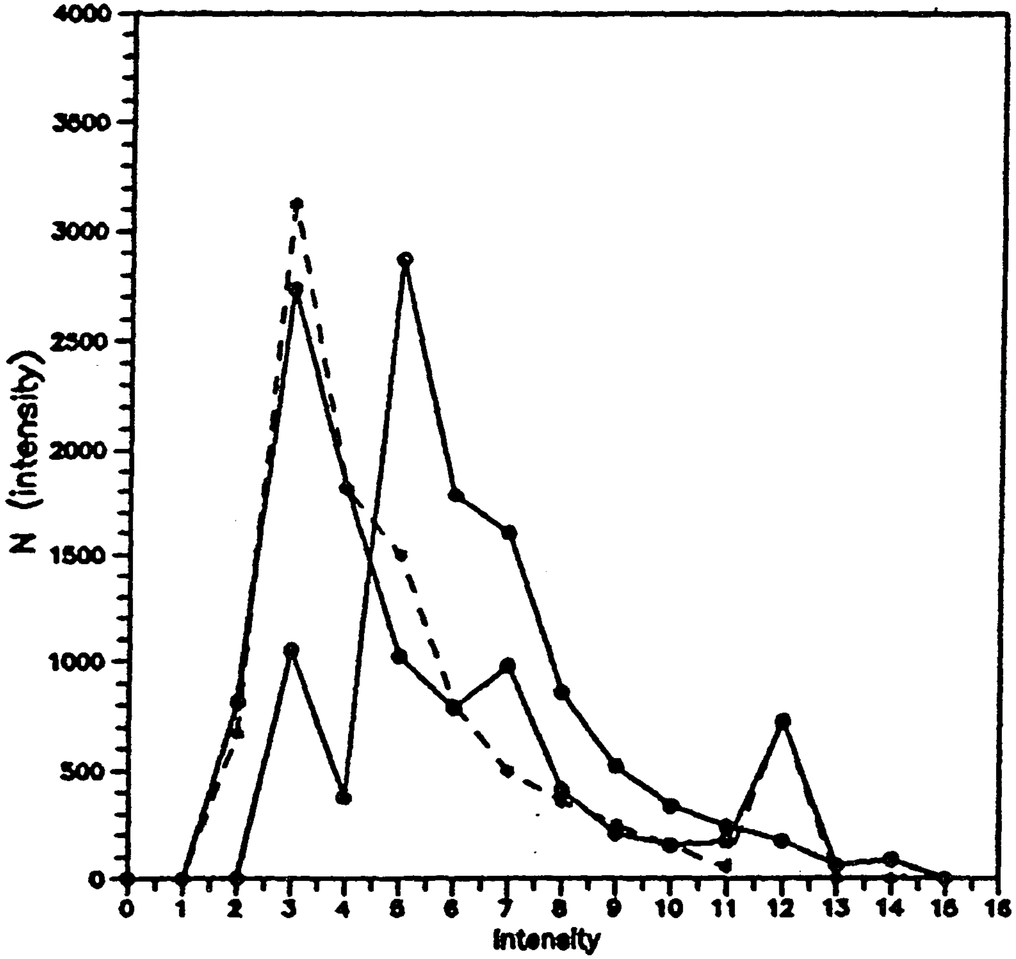

Fig.9.4.6 Case(1) Target pattern #1 LTES1,2,d
Comparison between sampled area
with and without the filter (4500A)
and the difference of both

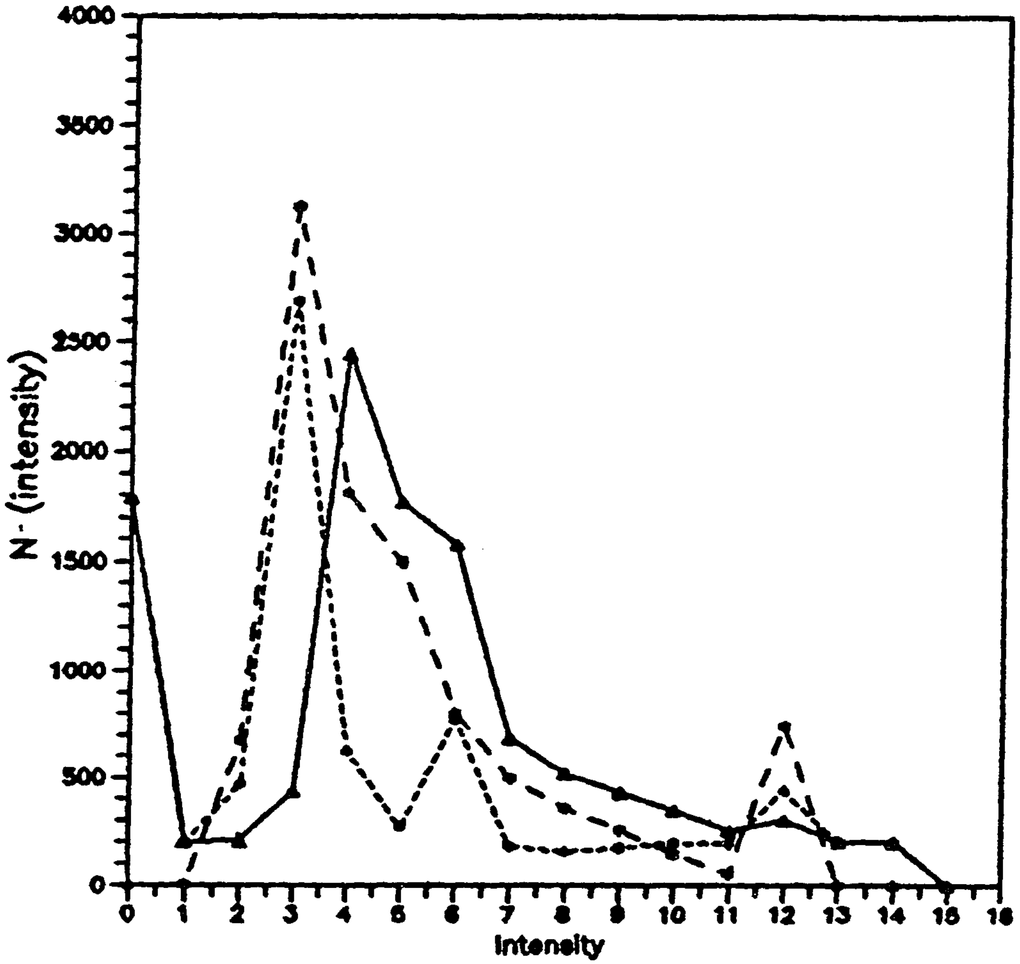

Fig.9.4.7 Case(1) Target pattern #1 LTES13dc
Comparison between sampled area
with and without the filter (4478.5A)
and the difference of both

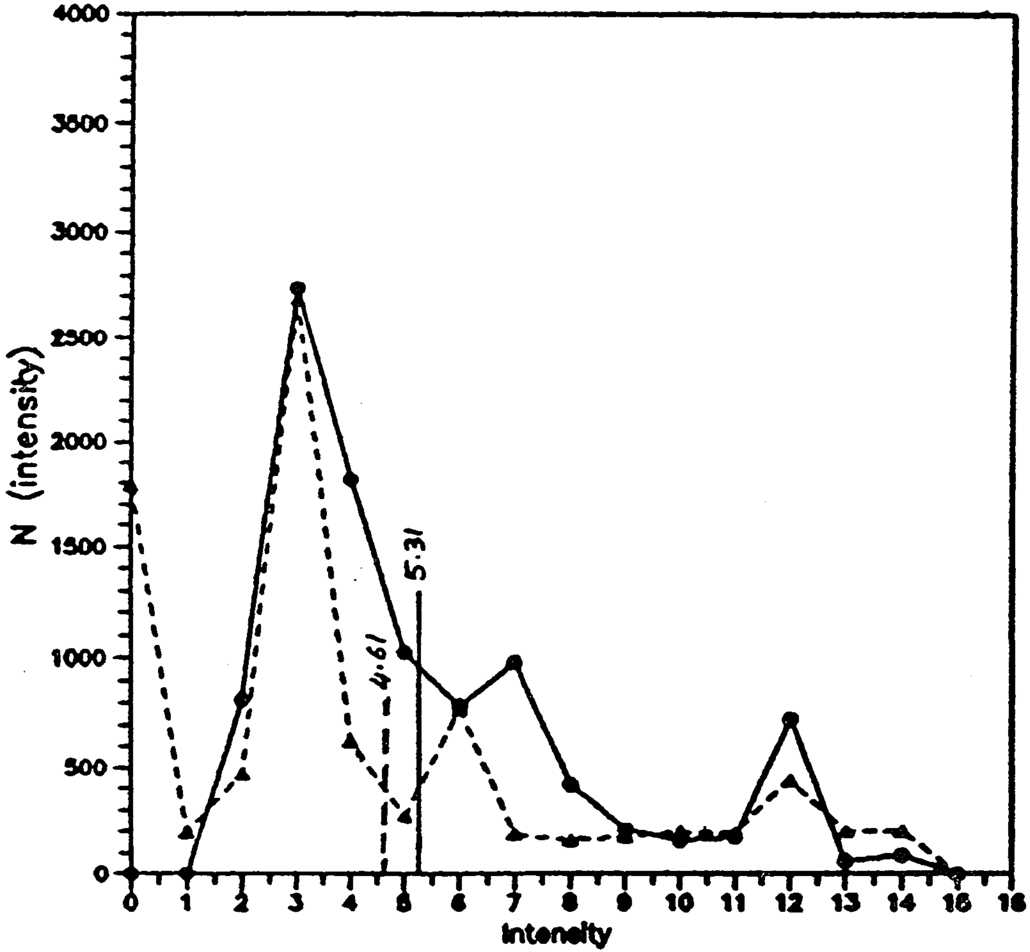

Fig.9.4.8 Case(1) Target pattern #1 LTESd
The difference between the two filters
in term of their intensities (centroide)
-▲-▲-▲- (4478.5A) —●—●— (4500A)

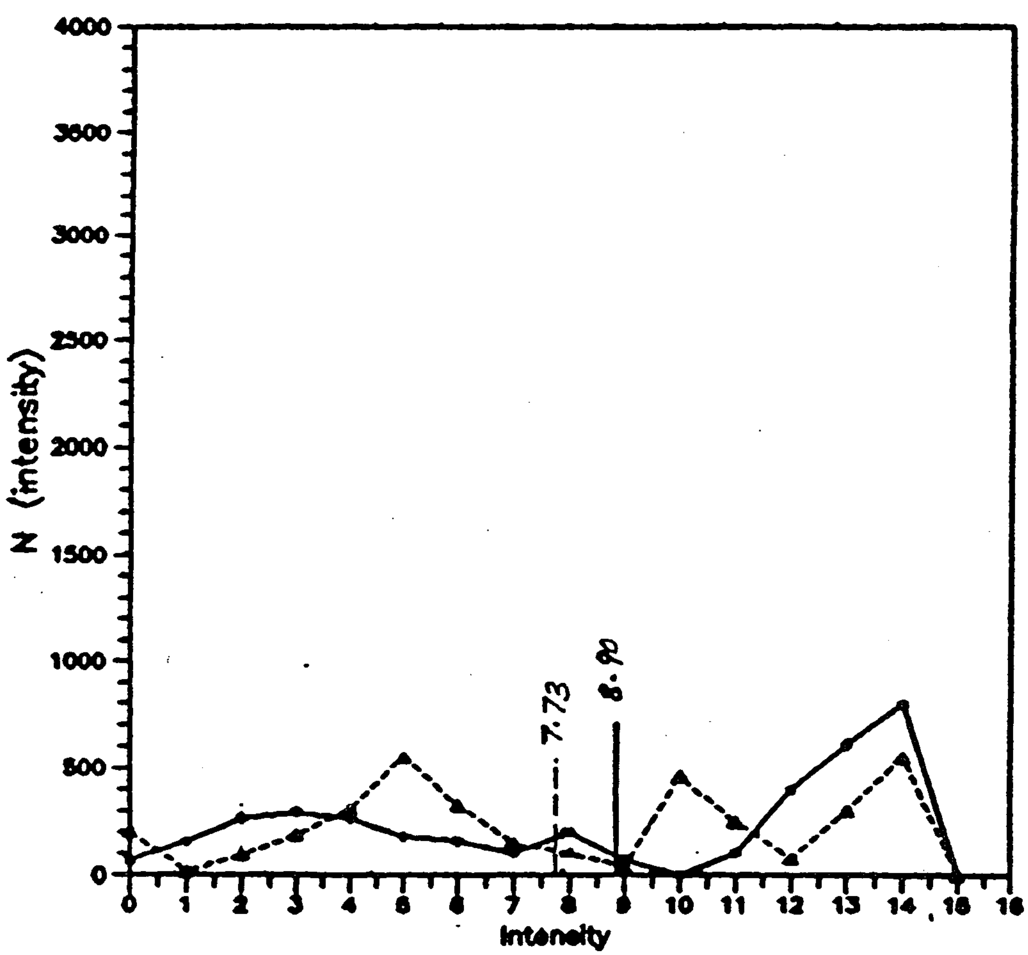

Fig.9.4.9 Case(2) Target pattern #2 RTESd
The difference between the two filters
in term of their intensities (centroide)
--▲--▲--▲ (4478.5A) —o—o— (4500A)

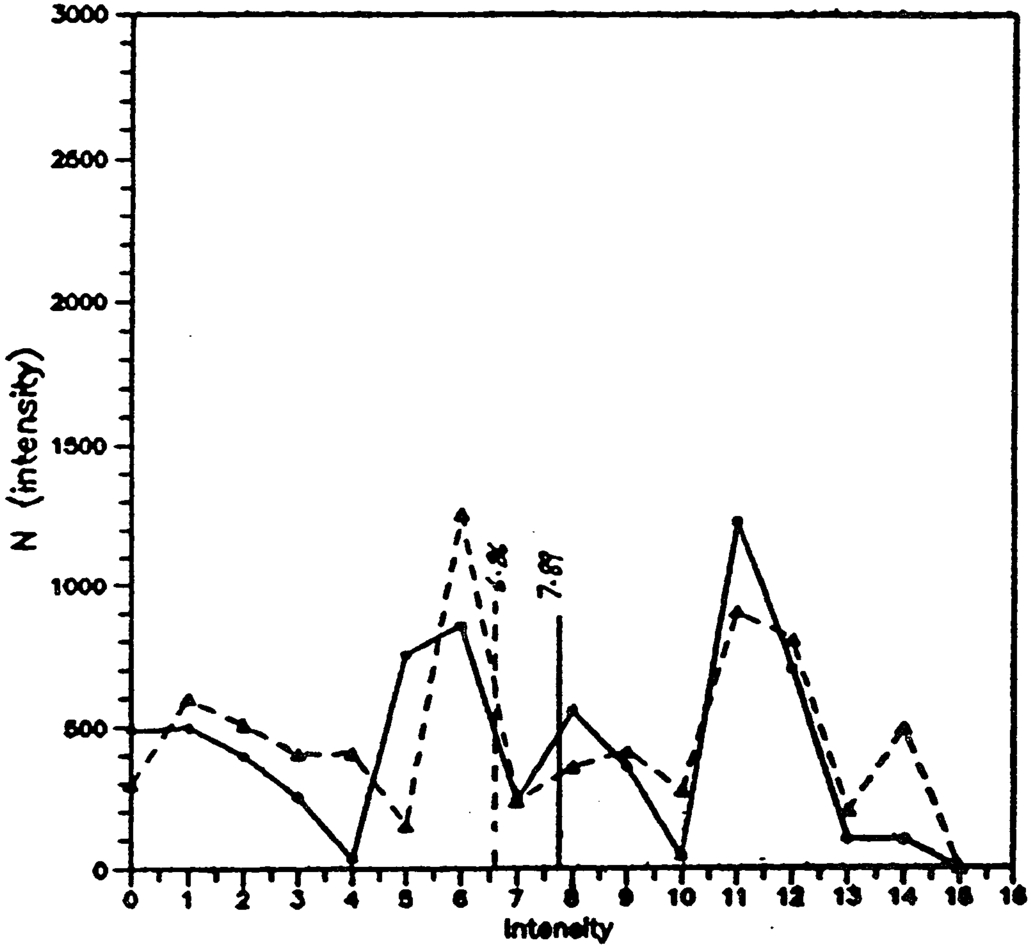

Fig.9.4.10 Case(3) Target pattern #3 MTESd
The difference between the two filters
in term of their intensities (centroide)
-▲--▲-▲- (4478.5A) —○—○— (4500A)

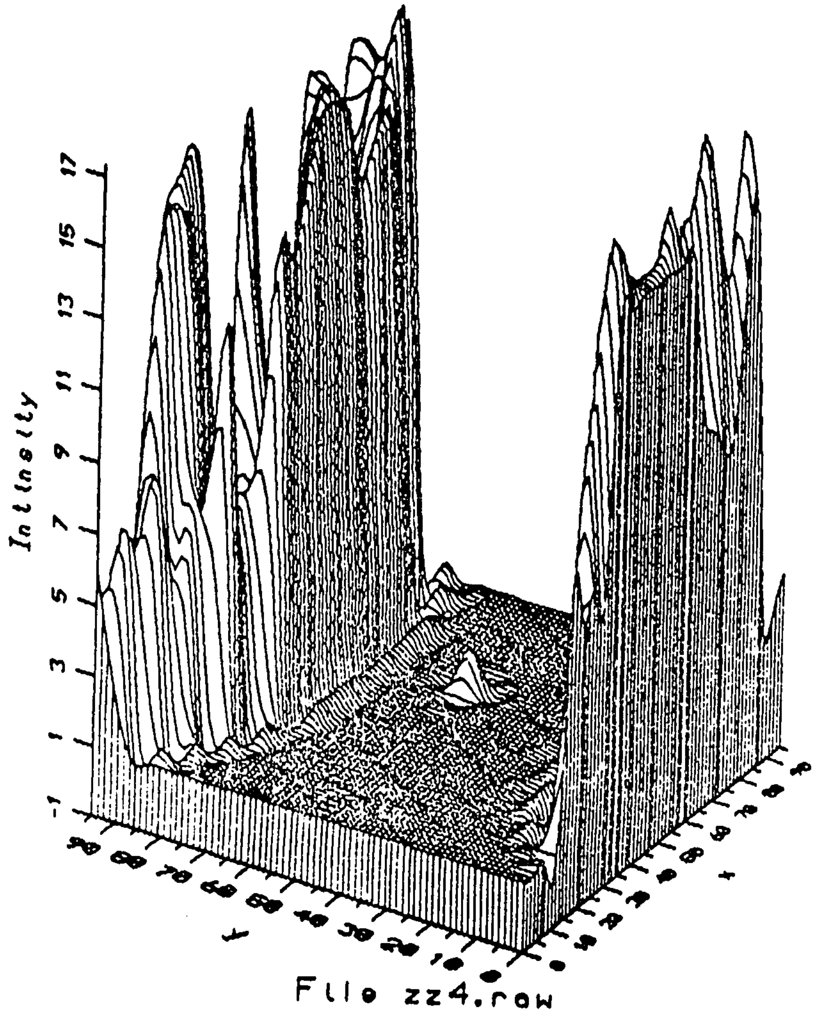

Fig.9.4.10a Raw data using 4478.5A filter

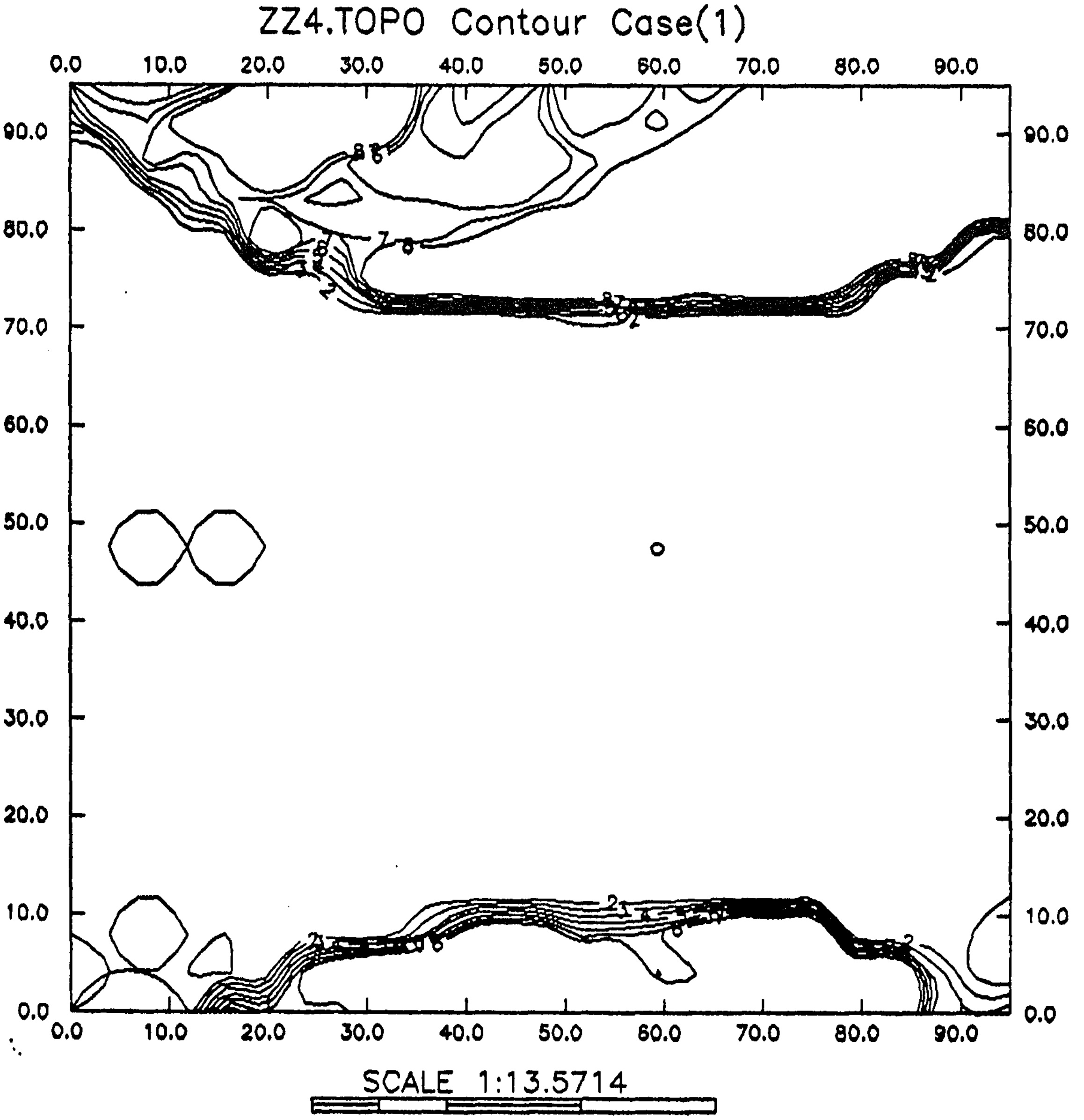

Fig.9.4.10a1 Raw data using 4478.5A filter contour map

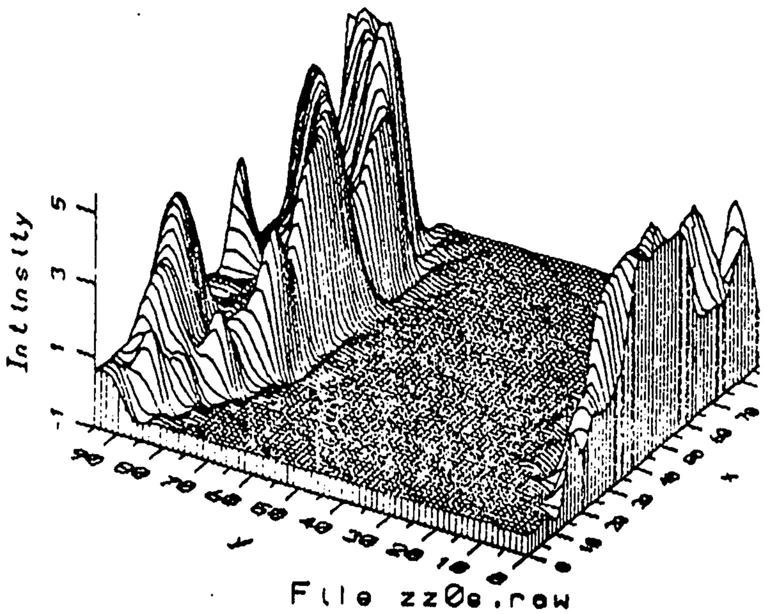

Fig.9.4.10b Raw data using 4500A filter

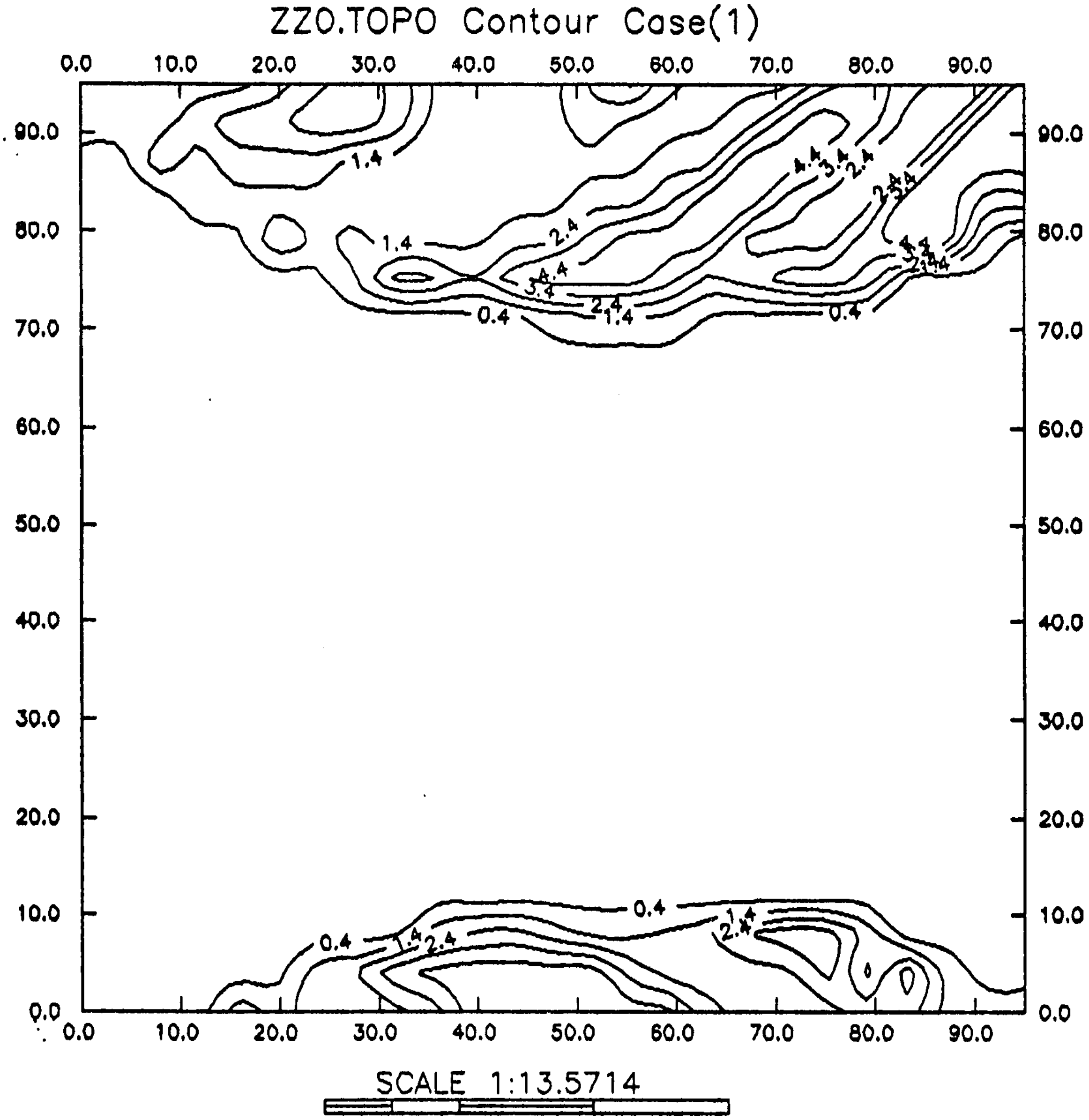

Fig.9.4.10b1 Raw data using 4500A filter contour map

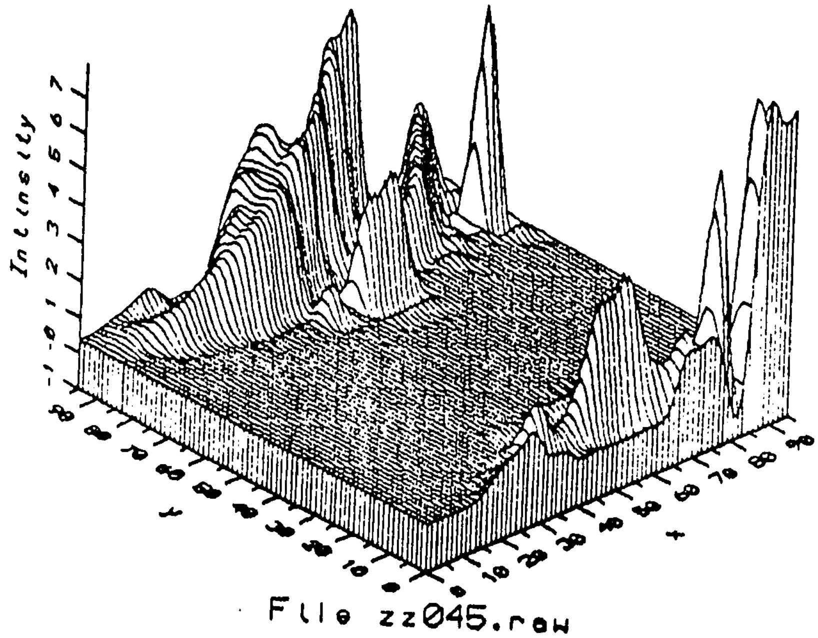

Fig.9.4.10c The ratio of ZZ0 & ZZ4

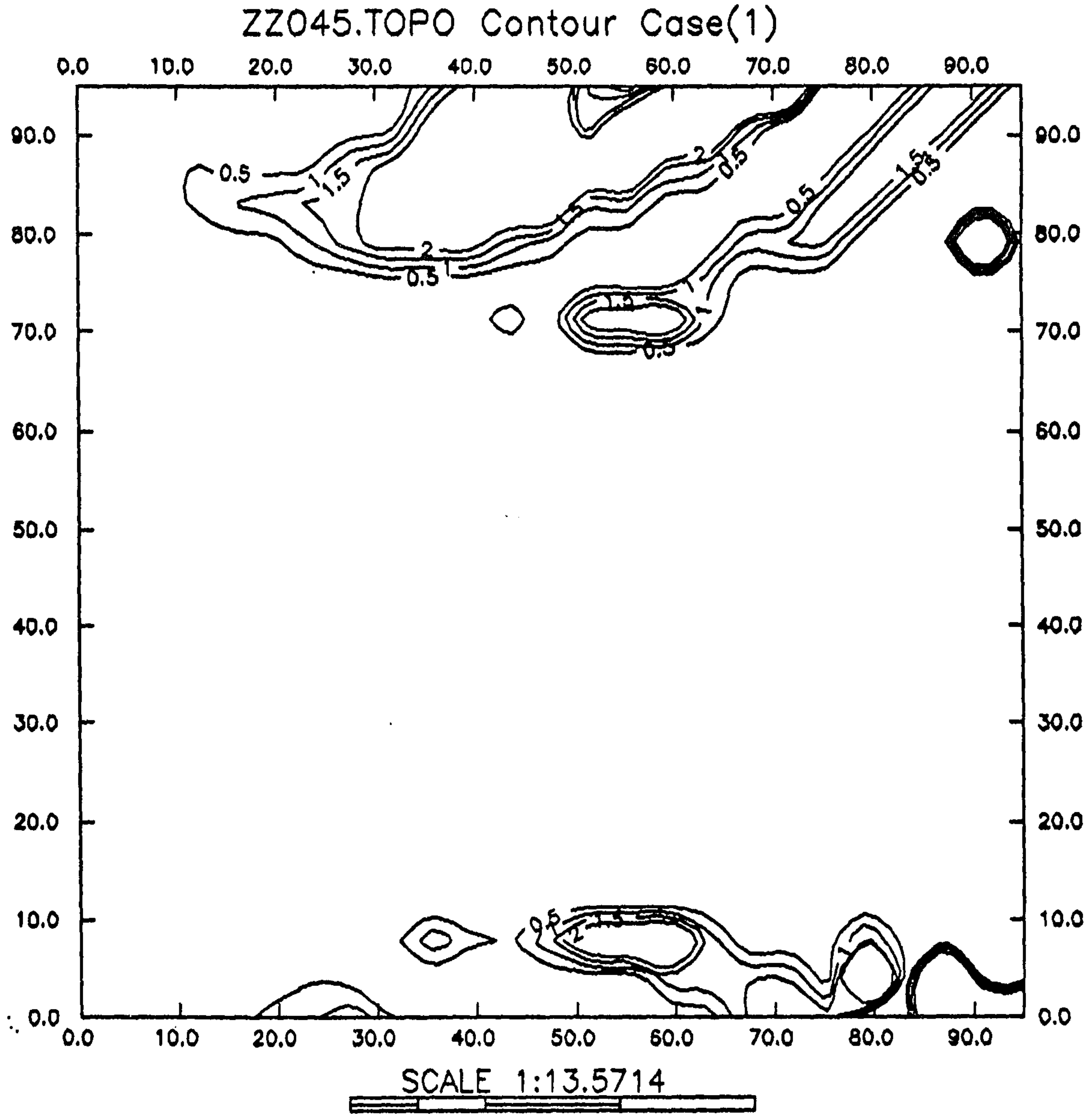

Fig.9.4.10c The ratio of ZZ0 & ZZ4 contour map

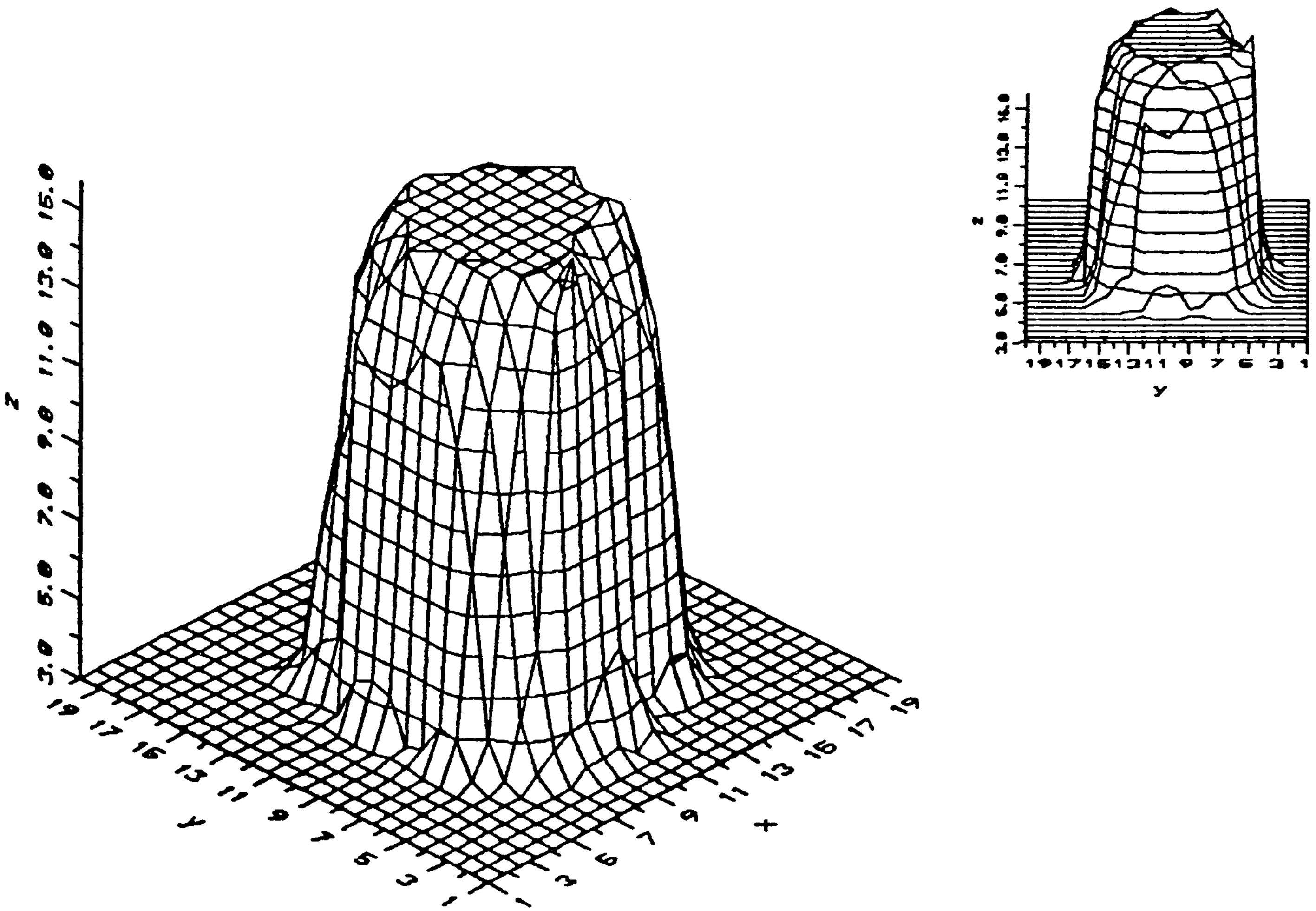

Fig.9.4.11 The Scaled Ratio I1/I2

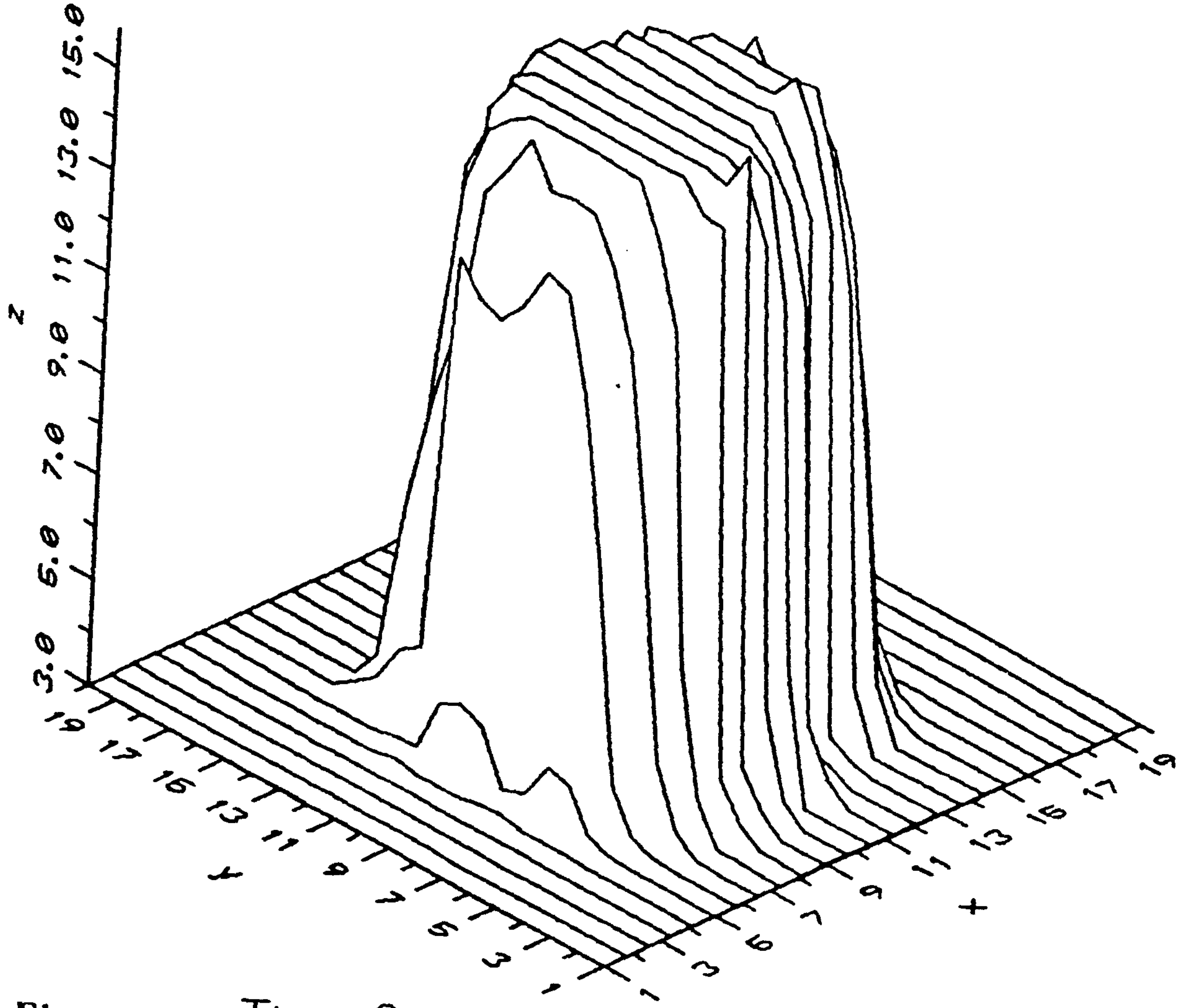

Fig.9.4.12 The Scaled Ratio I1/I2

Fig.9.4.13

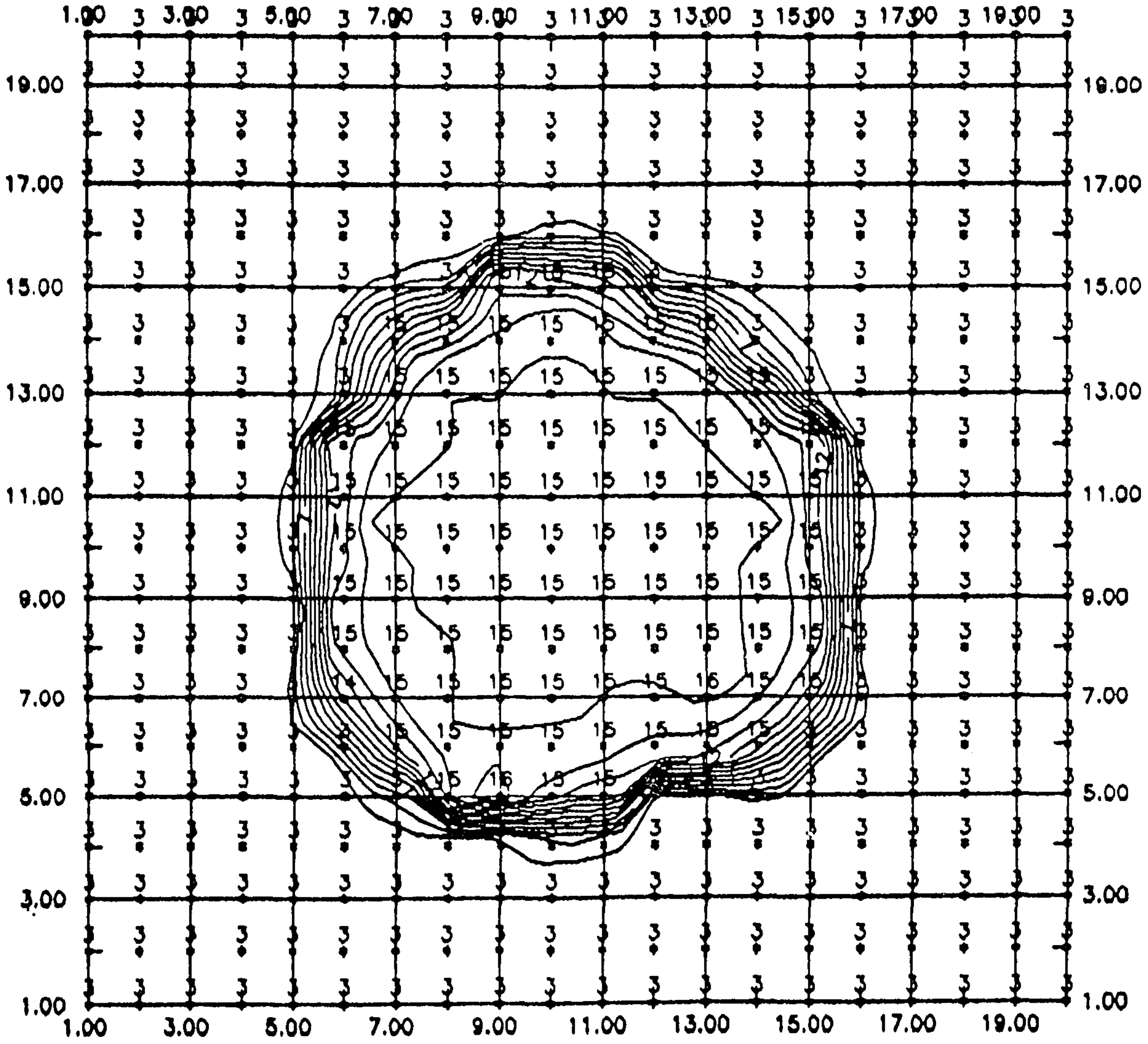

Contour map from Intensity grid (I1/I2)

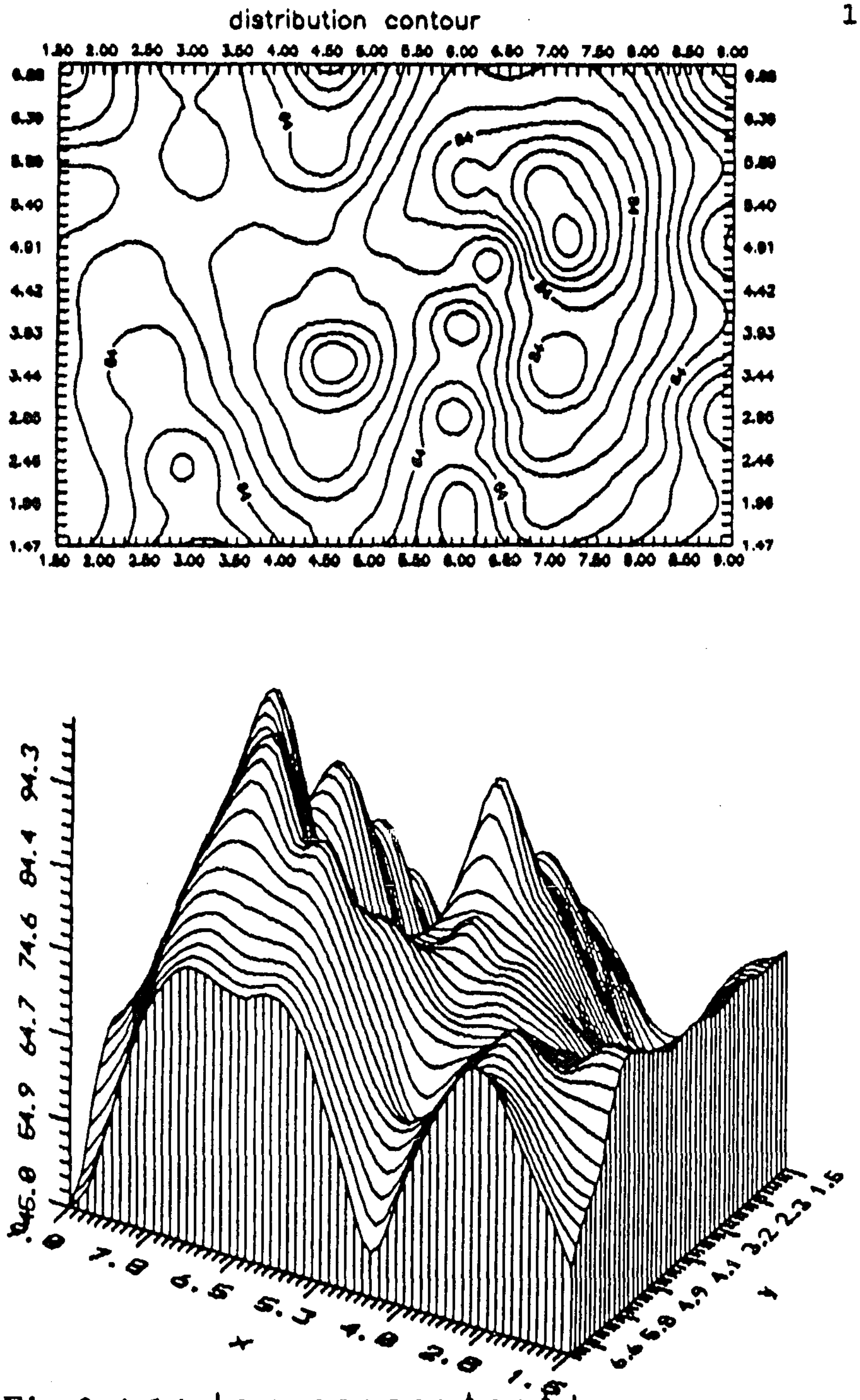

Fig.9.4.14 low concentration

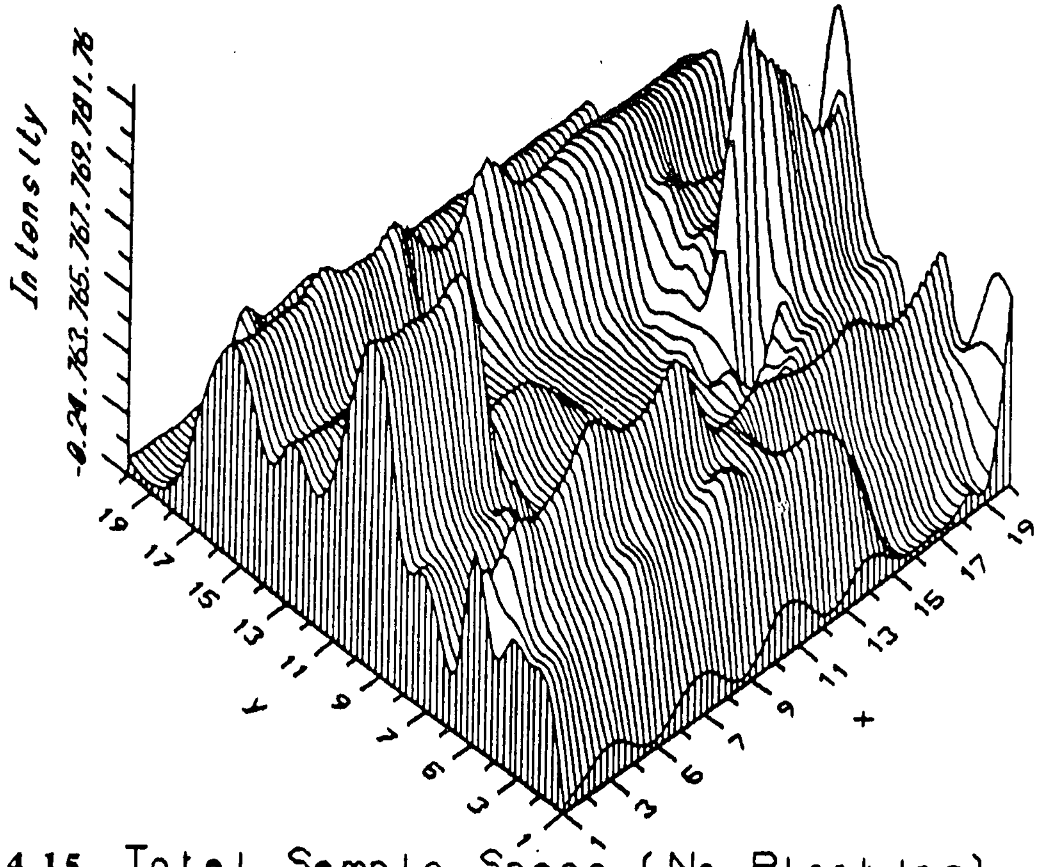

Fig.9.4.15 Total Sample Space (No Blanking)

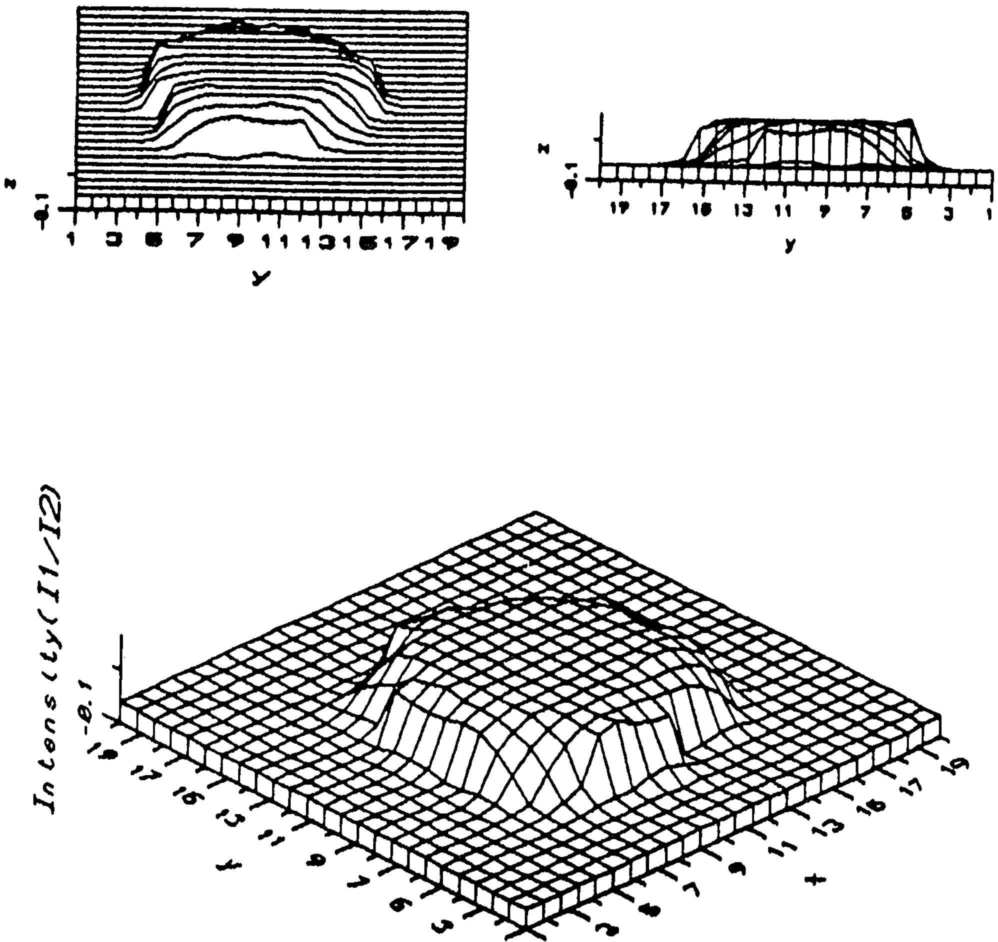

Fig.9.4.16 Ratio I1/I2=(1.5-1.6) No Scale Factor

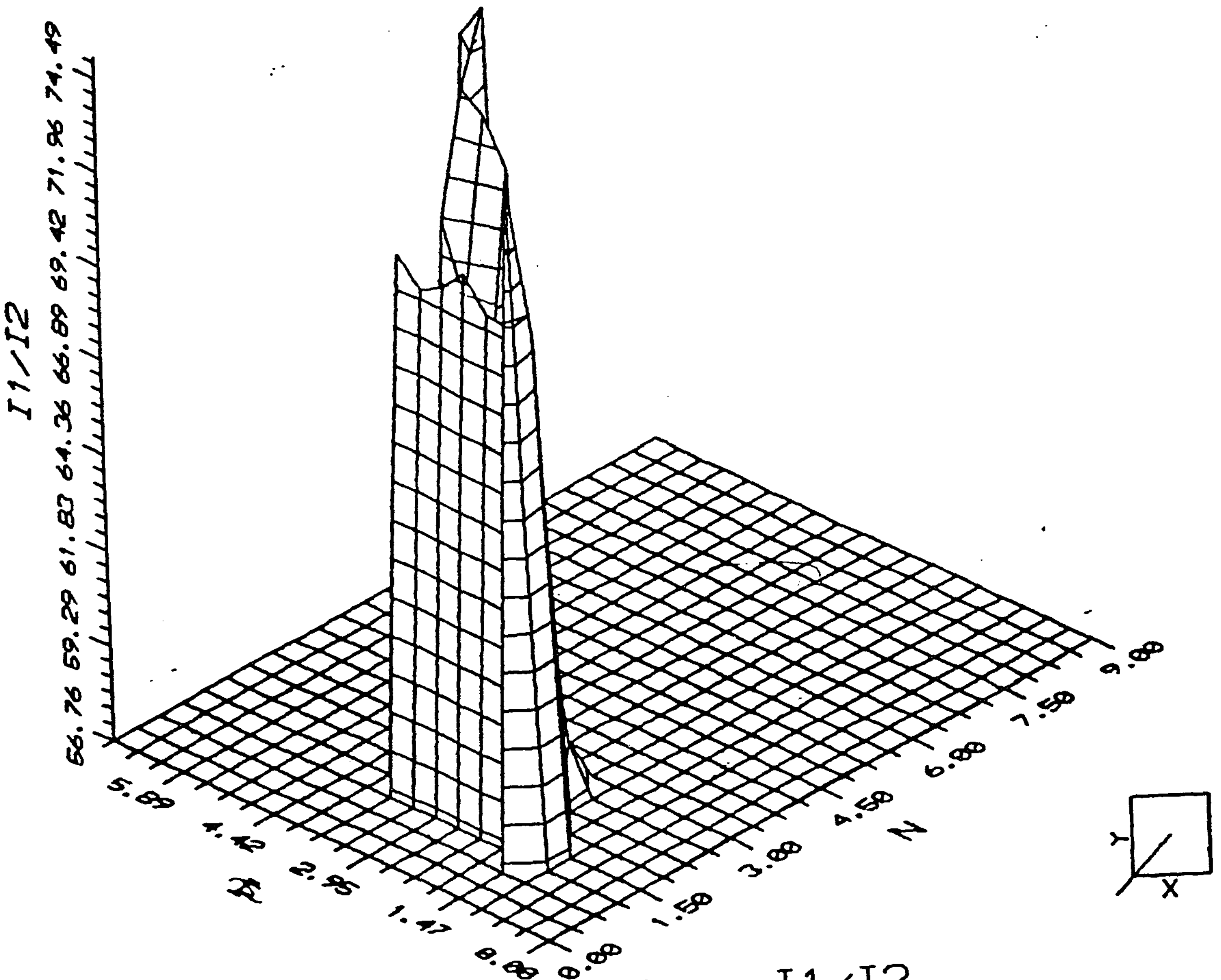

Fig.9.4.17 Gas Distribution I1/I2

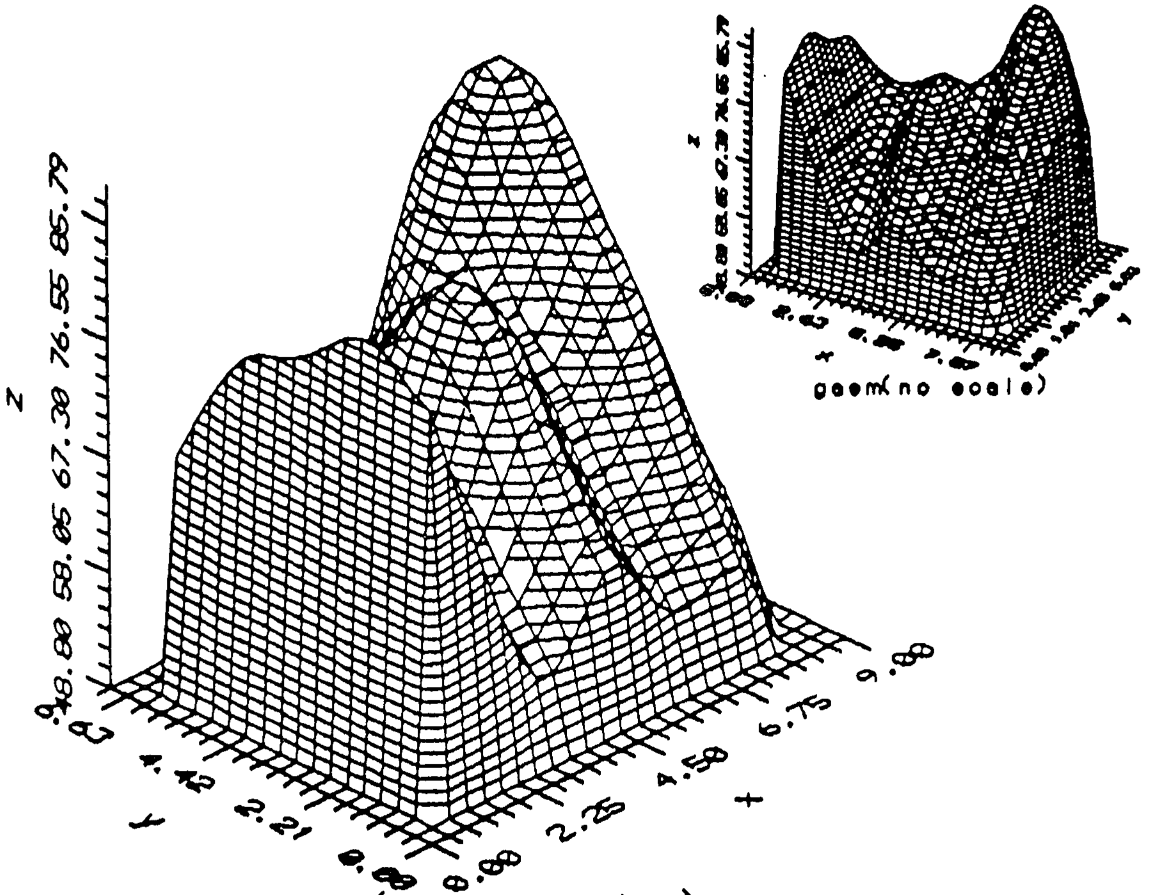

Fig.9.4.18 gasm(no scale)

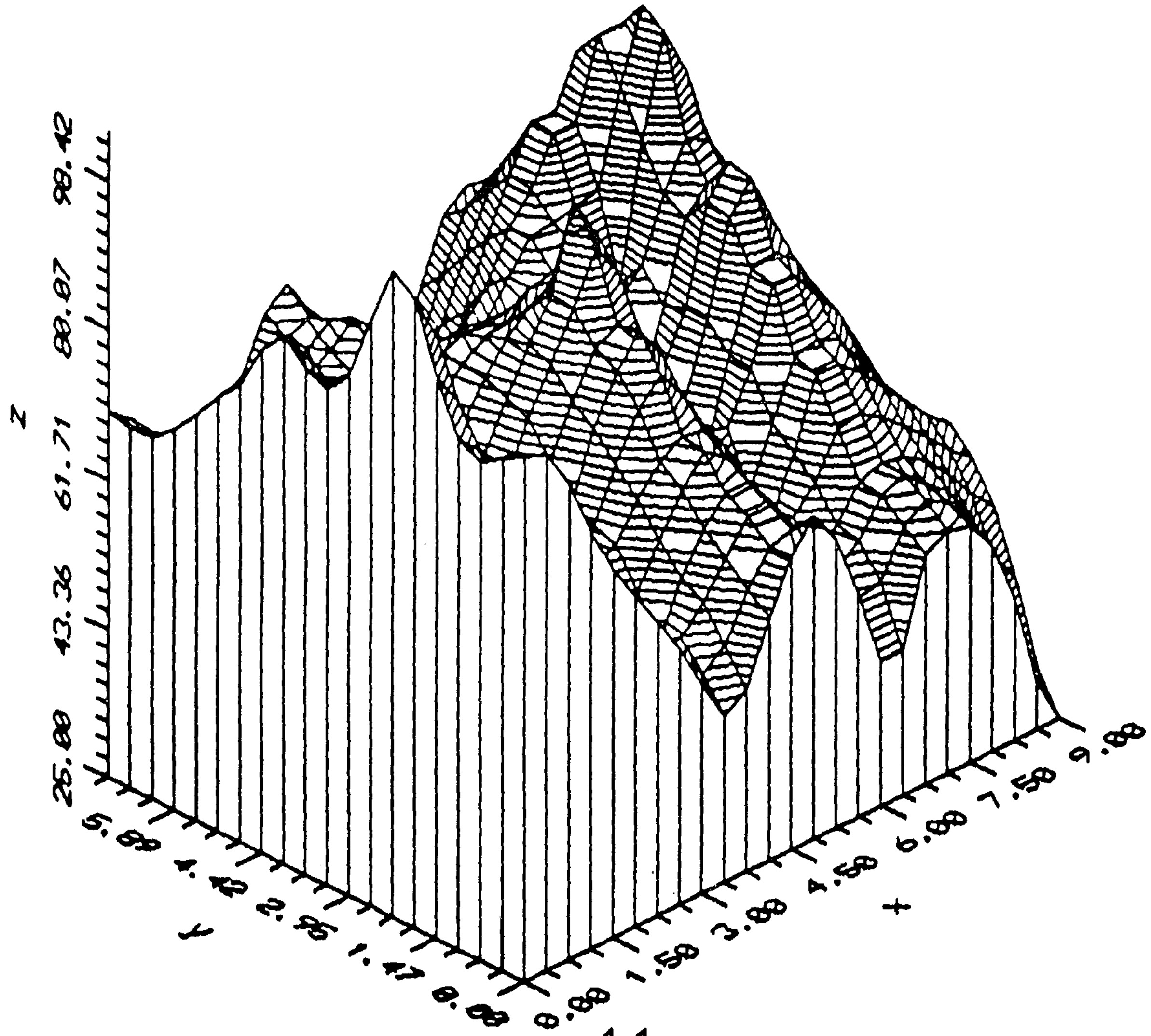

Fig.9.4.19 gas11

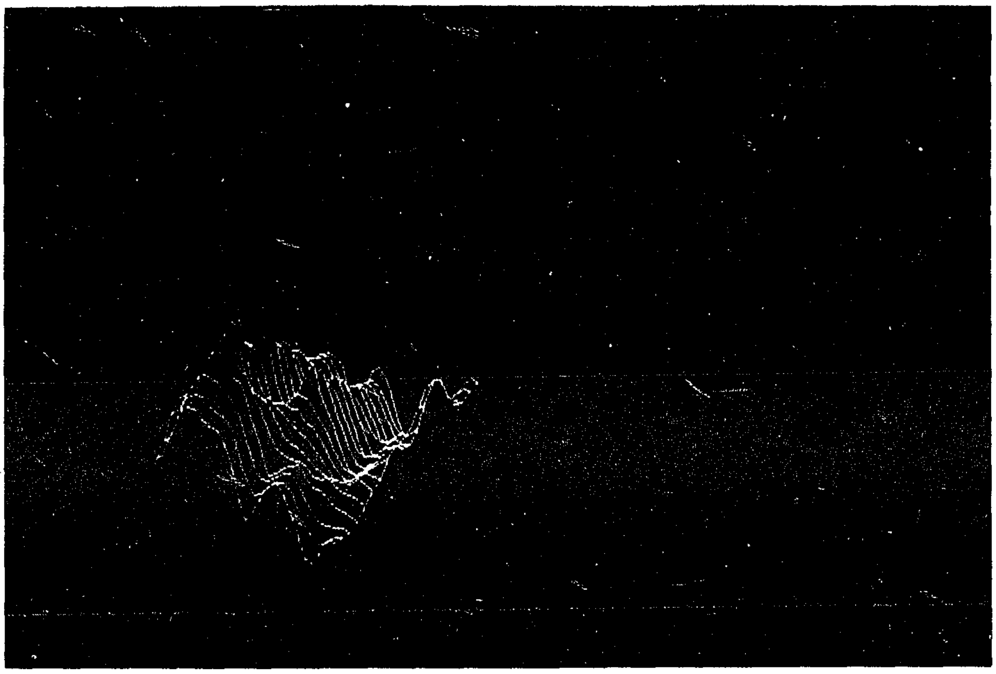

Fig. 9.4.20 Three dimentional representation group (1) using filter 4478.5A

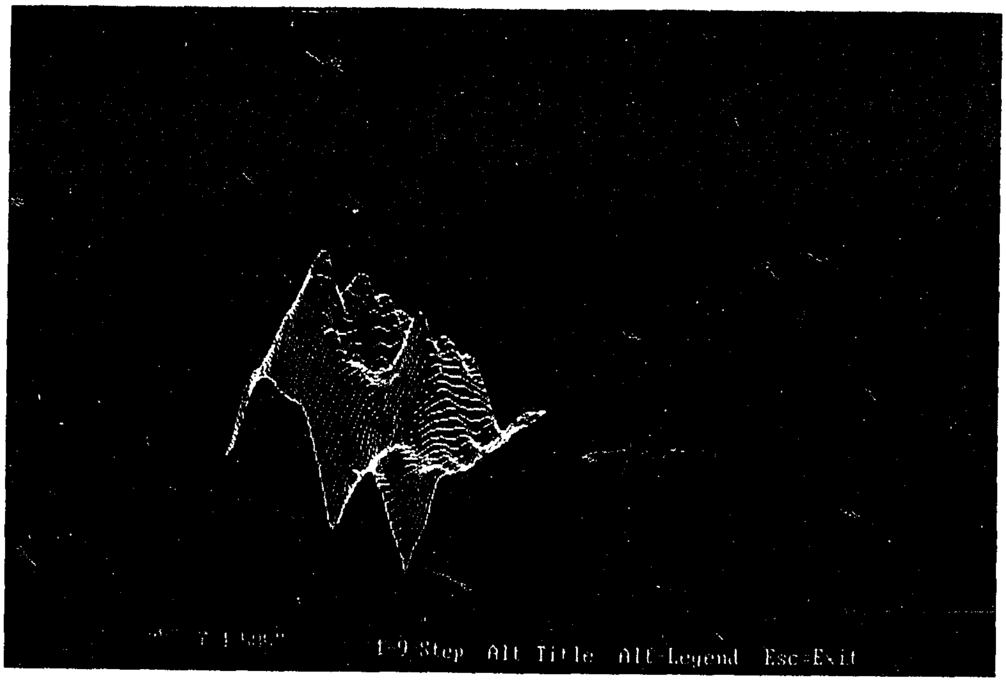

Fig. 9.4.21 Three dimentional representation group (1) using filter 4500 A

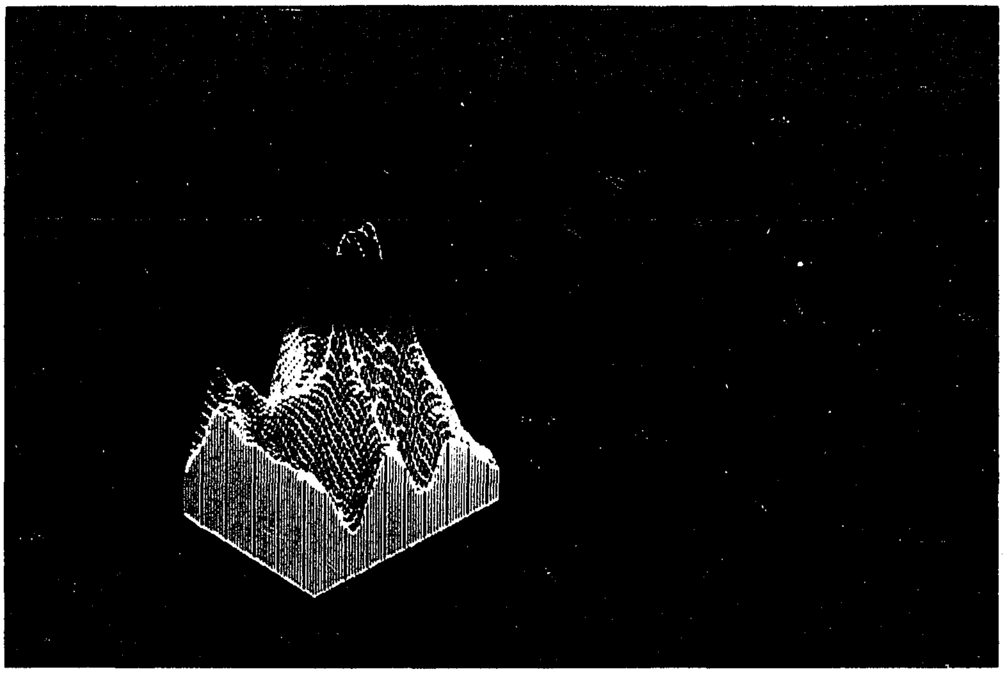

Fig. 9.4.22 Three dimentional representation group (1)
Scaled ratio of I_1 & I_2

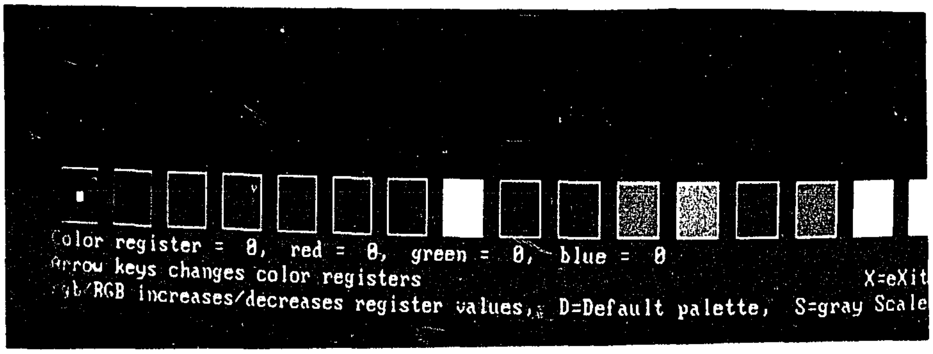

```
Color register =  0,  red =  0,  green =  0,  blue =  0
Arrow keys changes color registers                                X=eXit
rgb/RGB increases/decreases register values,  D=Default palette,  S=gray Scale
```

Fig. 9.4.23 Default palette for color registers

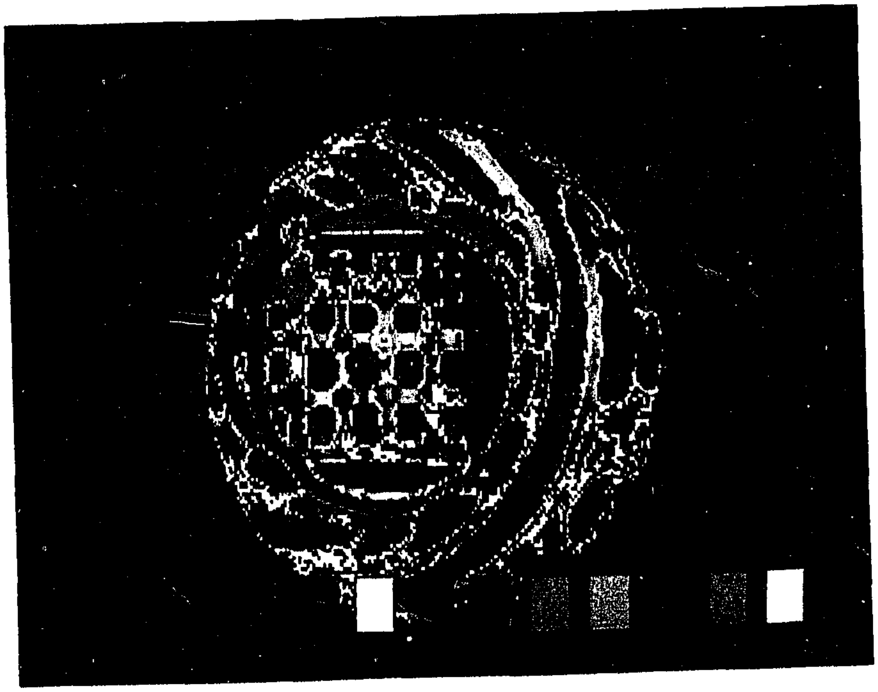

Fig. 9.4.24 Default alignment palette for the sampling chamber

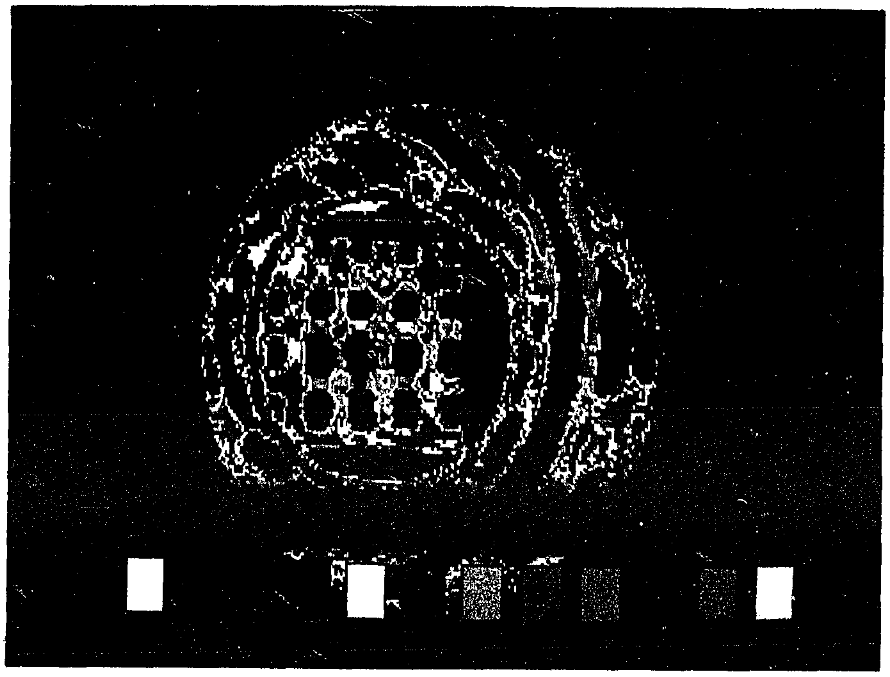

Fig. 9.4.25 Calibration palette for sampling chamber with no gas present

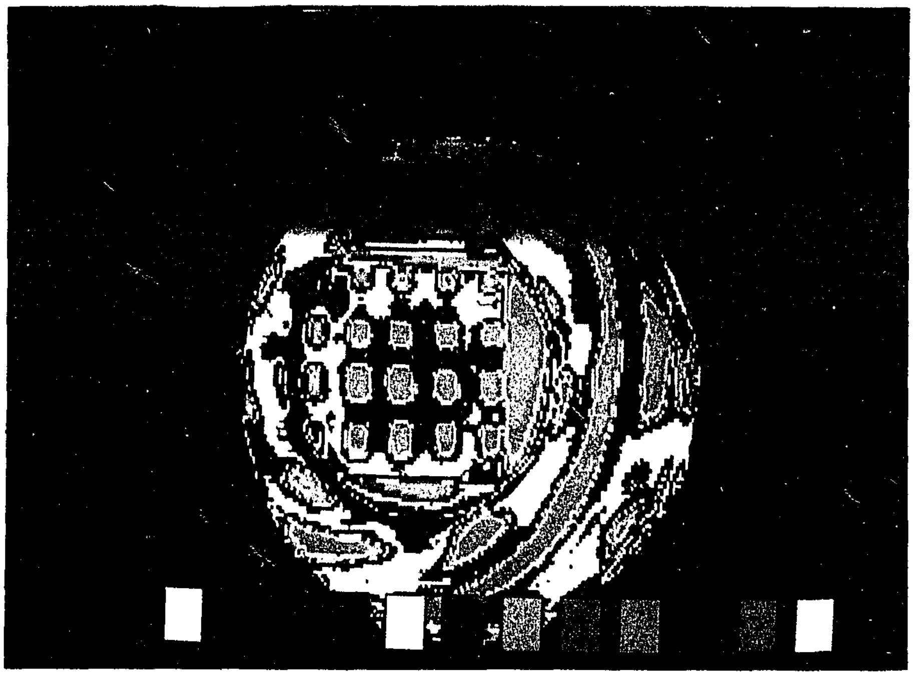

Fig. 9.4.26 Sampling chamber with high concentration of No_2

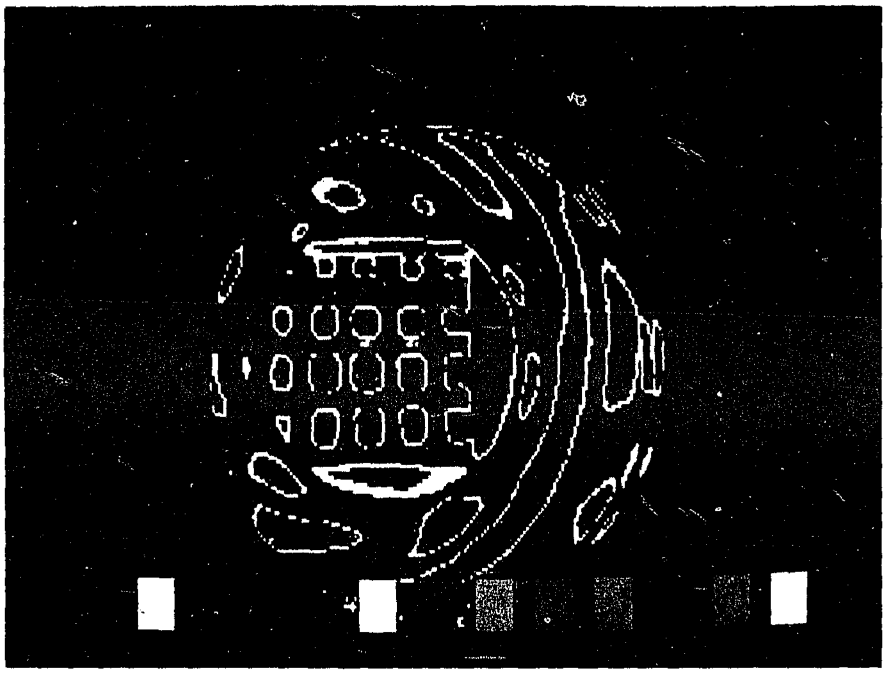

Fig. 9.4.27 Sampling chamber with low concentration of No_2

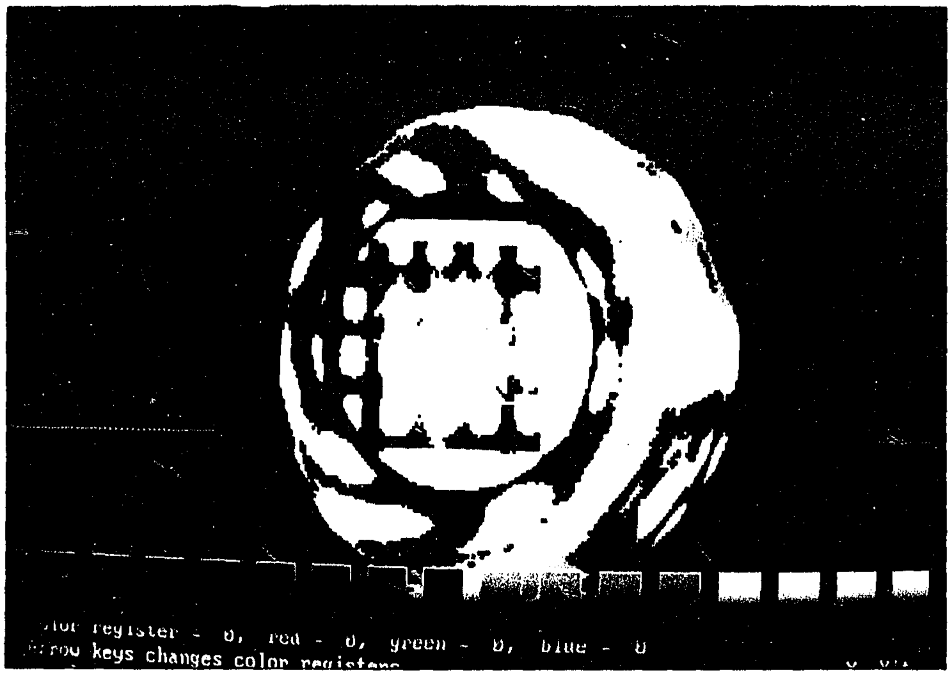

```
lor register = 0, red = 0, green = 0, blue = 0
rou keys changes color registers
```

Fig. 9.4.28 Default alignment palette for the sampling chamber using gray scale

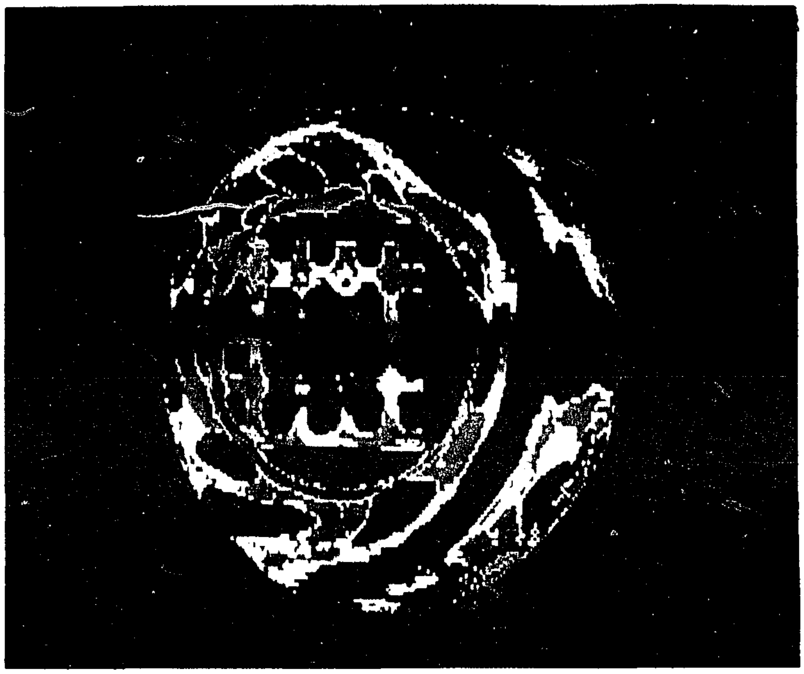

Fig. 9.4.29 Scaled ratio calibration palette

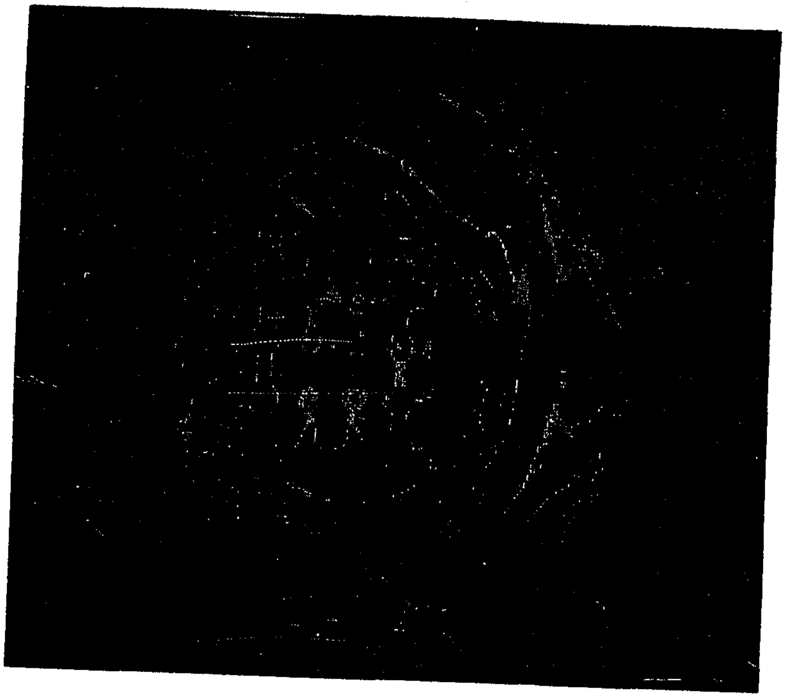

Fig. 9.4.30 Scaled ratio calibration palette using blanking technique

Fig. 9.4.31 Sampling chamber with no gas present

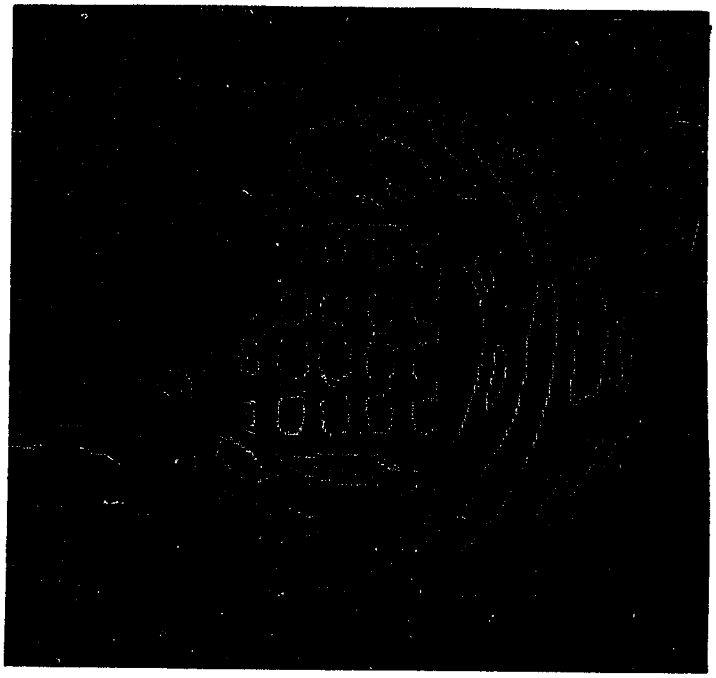

Fig. 9.4.32 Sampling chamber with scaled ratio when gas present

Fig. 9.4.33 Set #1 using on-peak absorption filter

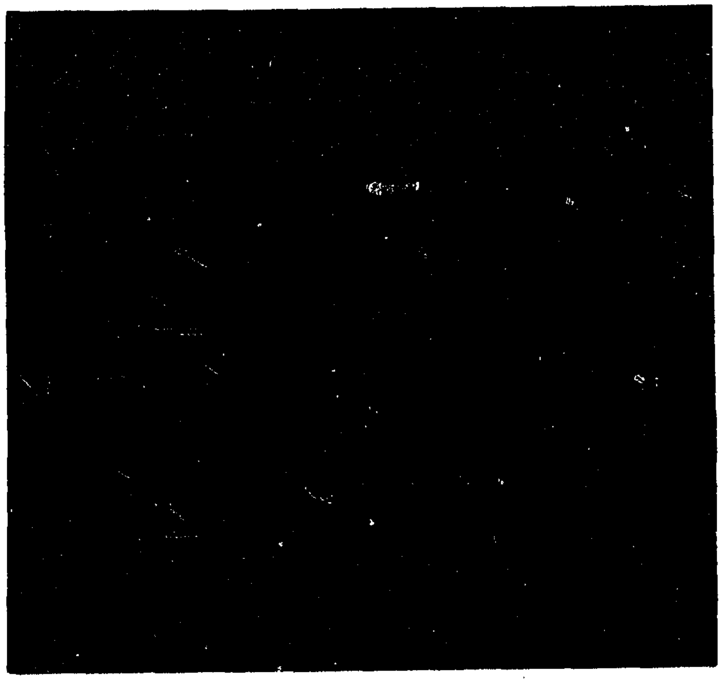

Fig. 9.4.34 Set #1 using off-peak absorption filter

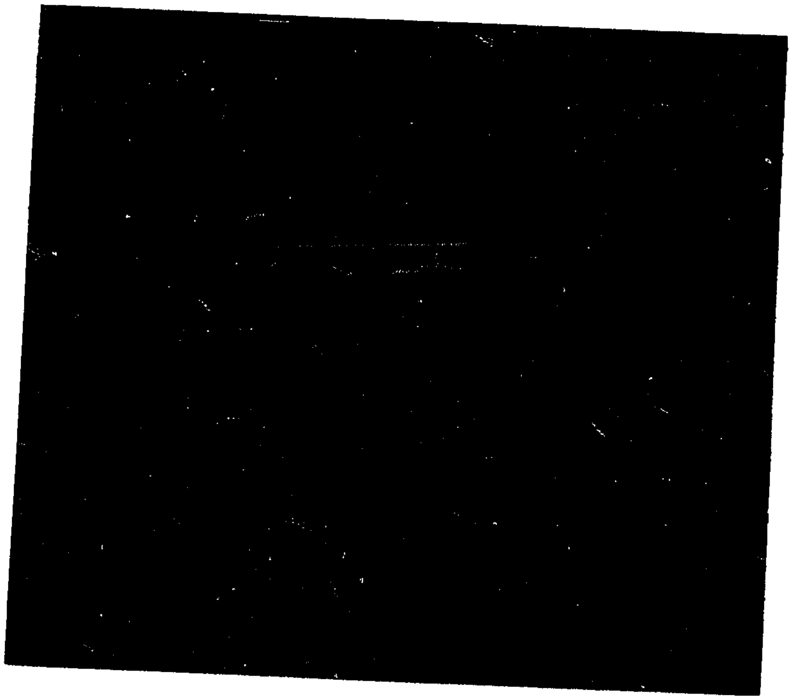

Fig. 9.4.35 Set #1 The ratio of the two intensities

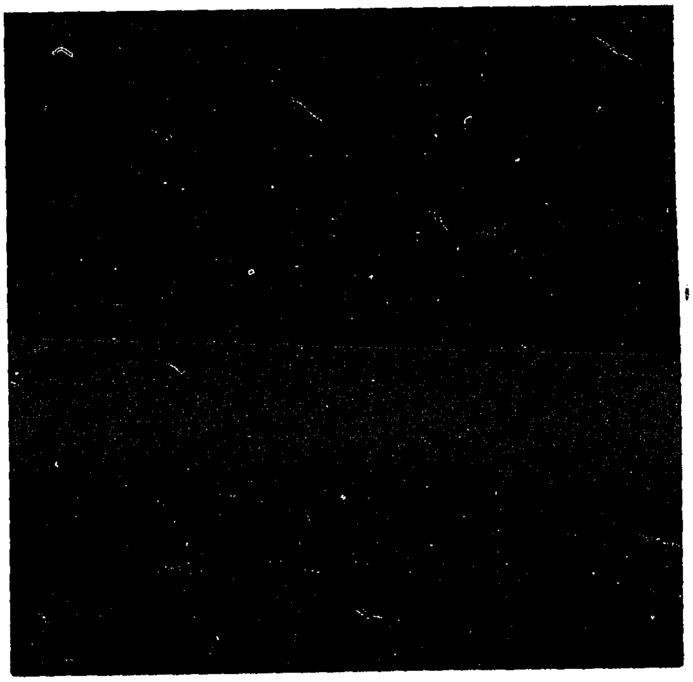

Fig. 9.4.36 Set #2 using on-peak absorption filter

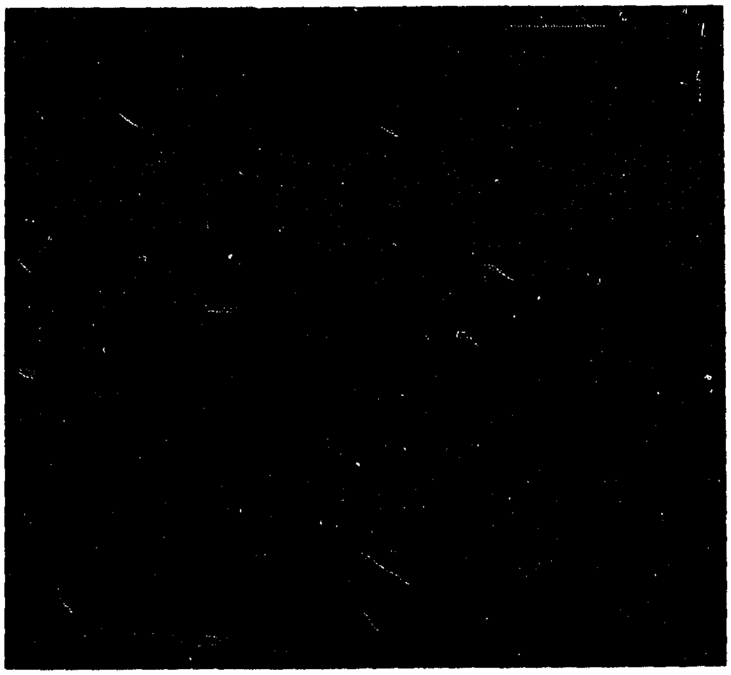

Fig. 9.4.37 Set #2 using off-peak absorption filter

Fig. 9.4.38 Set #2 The ratio of the two intensities

Fig. 9.4.39 Set #3 using on-peak absorption filter filling the FOV

Fig. 9.4.40 Set #3 using off-peak absorption filter filling the FOV

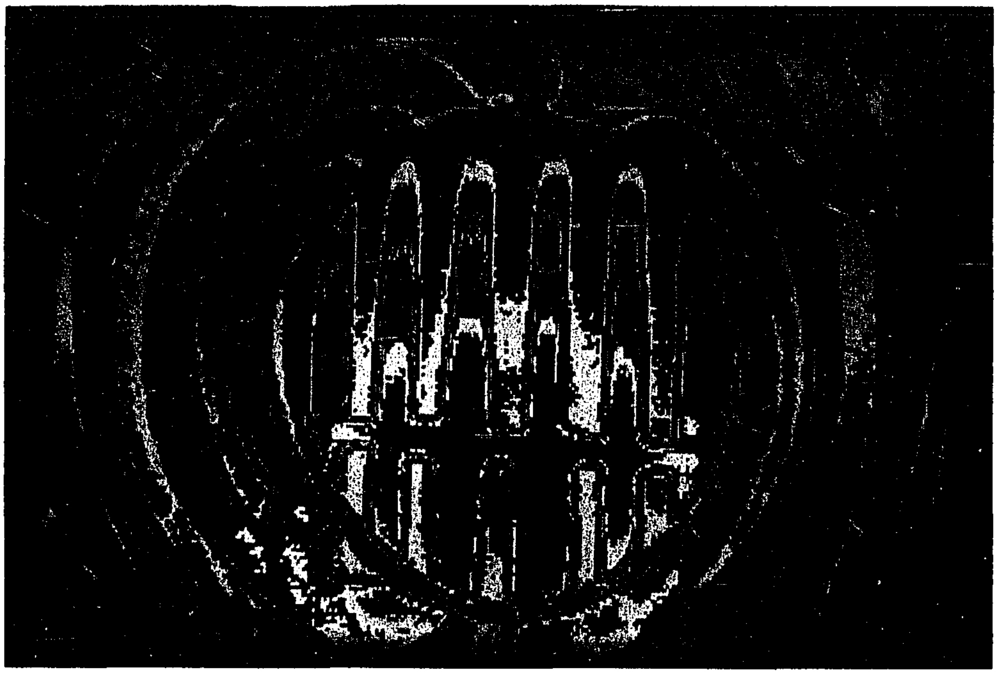

Fig. 9.4.41 Set #3 The ratio of the two intensities filling the FOV

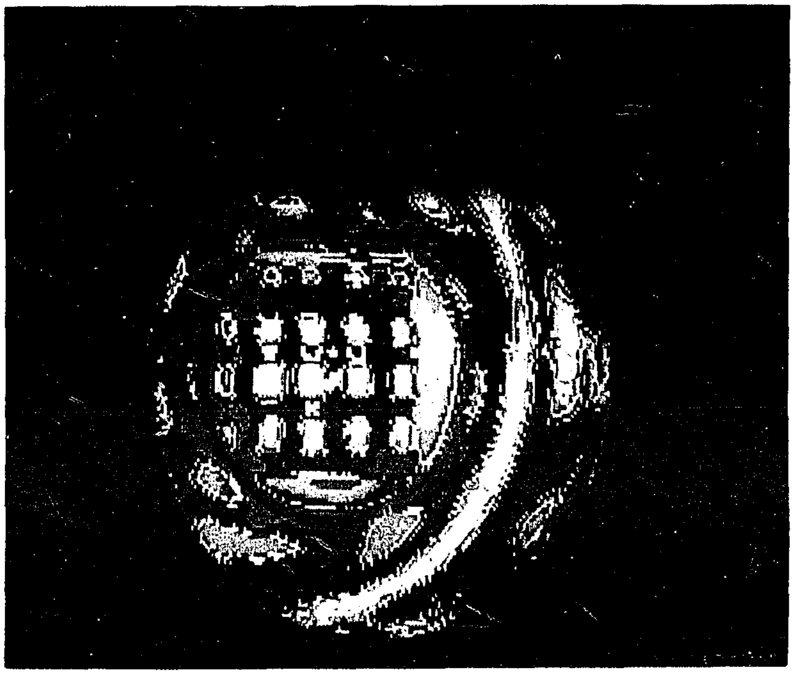

Fig. 9.4.42 Blue color assigned to a low level concentration of No_2

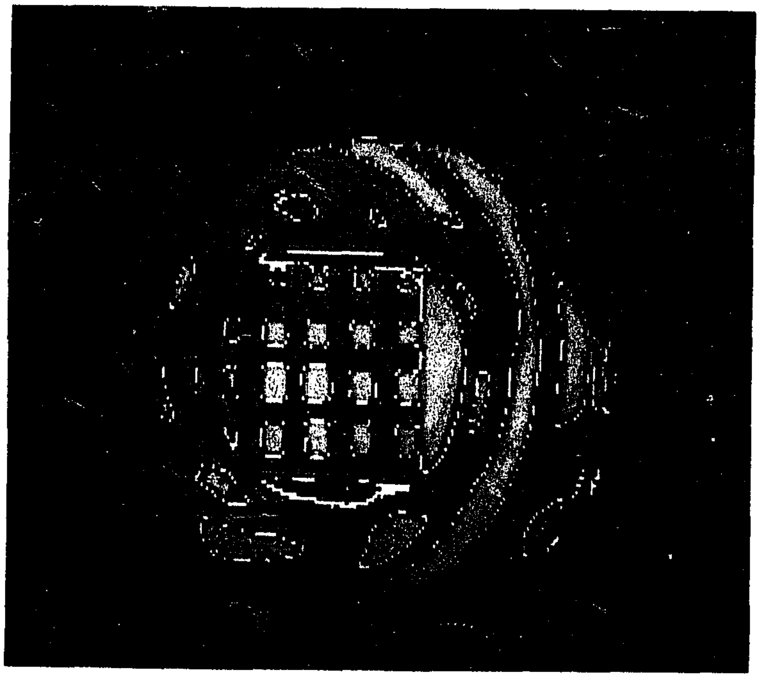

Fig. 9.4.43 Blue color assigned to a higher level concentration of No_2

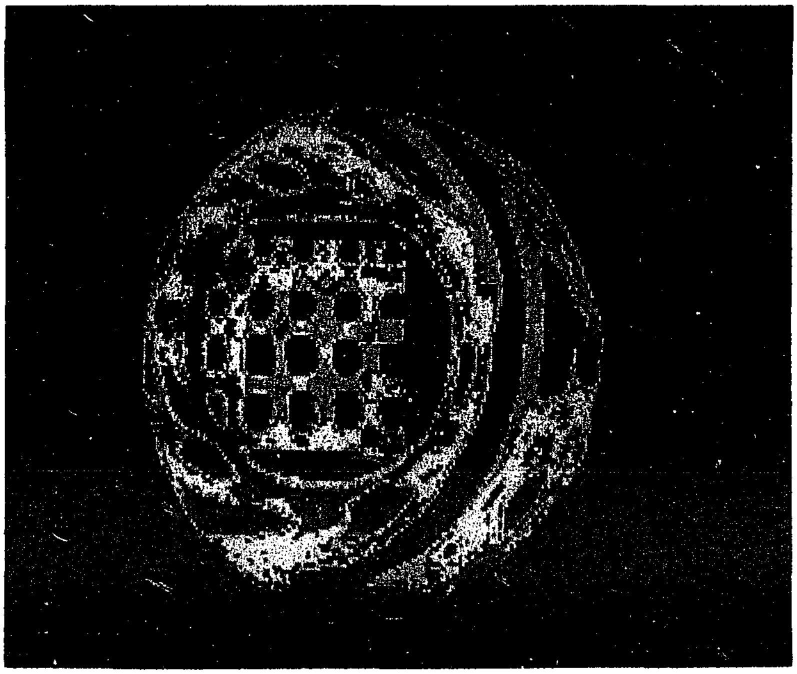

Fig. 9.4.44 Low level scaled ratio superimposed on a calibration palette

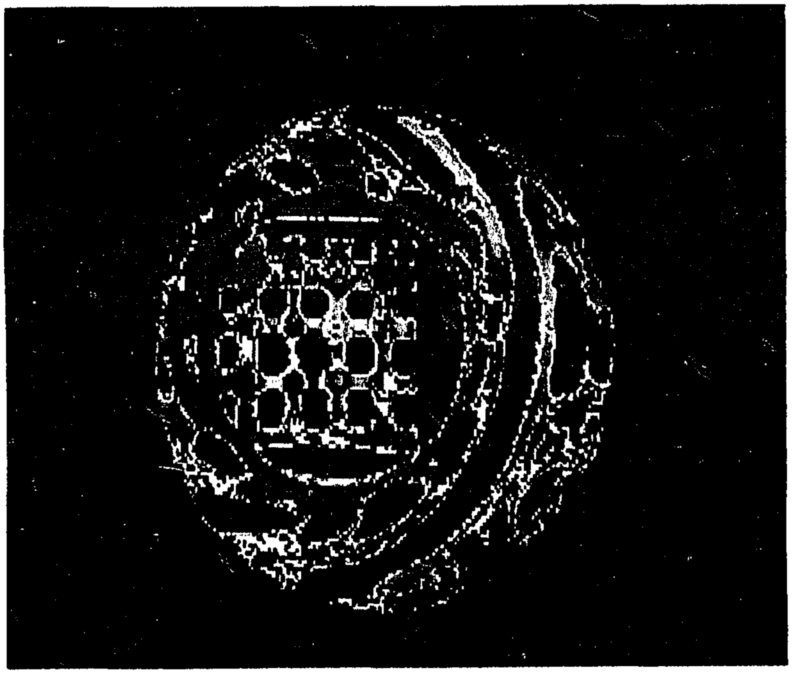

Fig. 9.4.45 High level scaled ratio superimposed on a calibration palette

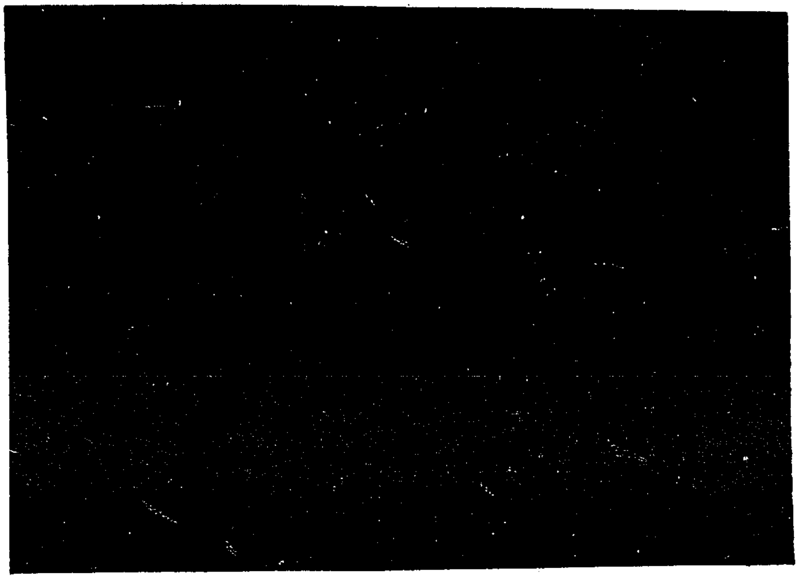

Fig. 9.4.46 Sampling chamber with no gas and no background target

Fig. 9.4.47 Accidental leak of No_2 outside of the sampling chamber

References

1. B.B. Snavely, Proc. IEEE, Aug , (1969), p. 1374.

2. A. Stern, "Air pollution", Third Edition, Vol. 3, Academic Press N.Y. (1977).

3. R.Perry, R.J Young, "Handbook of Air Polution Analysis", John Wiley & Sons, Halsted Press, (1977)

4. T. Kobayashi, and H. Inaba Appl. Phys. Letters 17 (1970), p.139.

5. T. Hirschfeld, Appl. Opt., 13 (1974), p. 1435.

6. H.J. Bernstein, Paper presented at the 1973 Spring Meeting of the optical Society of America, N.Y., April, 11-13.

7. P.L. Hanst and J.A. Morreal, J. Air Pollut. Cont. Ass., 18, (1968), p. 754.

8. H. Kildal and R.L. Byer, Proc. IEEE, 59, (1971), pp. 1644-1663.

9. T. Henningsen, M. Garbuny and R.L. Byer, Appl. Phys. Letts, 24, (1974), p. 242.

10. M.R. Bowman, A.J. Gibson and M.C.W. Sandford, Nature, 221, (1969), p. 456.

11. R.M. Schotland, E.E. Chermack and D.T. Chang, Proc. First International Symp. of Humidity and Moisture. p. 569, (Reinhart Bood Div., N.Y,. N.Y. (1964).

12. R.M. Schotland, Proc. Third Symp. on Remote Sensing of the Environment, Oct. 14-16 (1964), p. 215, Univ. of Michigan, Ann Arbor, Mich.

13. S.A. Ahmed and J.S. Gerggely, "Laser Radar Study Using Resonance Absorption for Remote Detection of Air Pollutants", Fifth Conf. on Laser Ladar Studies of Atmo., June 4-6, (1973), Williamsburg, Va.

14. S.A. Ahmed, App. Opt., 12, (1973), p. 901.

15. Chahine, M.T., et al. "Interaction mechanisms within the atmosphere, in Manual of Remote Sensing" American Society of Photogrammetry, Falls Church, Va, (1983).

16. Hansen, J.E., and L.D. Travis. "Space Scince Rev.", 16, 527, (1974).

17. W.F. Herget, W.D. Conner, Environmental Science Technology,11, No. 10, Oct., (1977).

18. R.A. Wadden and P.A. Scheff, "Indoor Air Pollution, Charactrization, Prediction and Control" p 13-28 , Johan Wiley & Sons, (1976).

19. Van de Hulst, H.C. "Light Scattering by Small Particles." Wiley, New York, (1957).

20. Chandarasekhar, S. Radiative Transfer, Oxford Univ. Press, (1950).

21. C. Elachi "Introduction to the Physics an Techniques of Remote Sensing", Wiley , (1987).

22. Herman, B. M., S. R. Bowning "The Effects of Atmospheric Aerosols on Scattered Sunlight" , J.Atmos. Sci.,28, 419-428, (1971).

23. Waters J. "Absorption and Emission by Atmospheric Gases", Chapter2.3 in Methods of Experimental Physics, Vol.12, Astrophysics, Part B. Academic Press, New York, (1976).

24. Smith, K.E. "Wave attenuation and Brightness Temperature due to Atmospheric Gases", Radio Sci., 17, 1455-1464, (1982).

25. Barnett. T. L. "Application of Nonlinear Least Square Method of Atmospheric Sounding", J. Atmos. Sci., 26, 457, (1969).

26. Chahine, M., et al. "Interaction mechanisms within the atmosphere", R. N. Colwell (Ed.), Manual of Remote Sensing. Am. Soc. of Photogrammetry, Falls Church, VA, (1983).

27. Swain, P.H., and S.M. Davis. "Remote Sensing, The Quantitative Approach", McGraw-Hill, New York, (1978).

28. Goetz, A., G. Vane, J. Solomon, and B. Rock. "Imaging spectrometry for Earth Remote Sensing", Science, 228, 1147-1153, (1985).

29. Dozier, J., and A. Strahler. "Ground Investigation in Support of Remote Sensing", Chapter 23. In R. N. Colwell (Ed.) Manual of Remote Sensing. American Soc. of Photogrammetry, Falls Church, VA, (1983).

30. Bernstein, R. (Ed.), "Digital Image Processing for Remote Sensing", New York, IEEE Press, (1987).

31. Levinthal, E., et al.,"Image Processing and Products.", Icarus 18, 75 (1973).

32. William B. Green, "Digital Image Processing, A System Approach", VNR. (1983).

33. lorre, J.J.,D. J. Lynn, and W. D. Benton, "Recent Developments at JPL in the Application of Digital Image Processing Techniques", Proc. SPIE 47, 234 (1976).

34. Sabins F.F., Jr., "Remote Sensing-Principles and Interpretation", San Francisco, Freeman, (1978).